Bio-ethanol dehydrogenation to acetaldehyde over PdZn/Mg(Al)Ox

Bram De Maesschalck

Supervisors: Prof. dr. ir. Joris Thybaut, Dr. Vladimir Galvita
Counsellor: Jolien De Waele

Master's dissertation submitted in order to obtain the academic degree of
Master of Science in Chemical Engineering

Department of Chemical Engineering and Technical Chemistry
Chair: Prof. dr. ir. Guy Marin
Faculty of Engineering and Architecture
Academic year 2015-2016

UNIVERSITEIT GENT

Bio-ethanol dehydrogenation to acetaldehyde over PdZn/Mg(Al)Ox

Bram De Maesschalck

Supervisors: Prof. dr. ir. Joris Thybaut, Dr. Vladimir Galvita
Counsellor: Jolien De Waele

Master's dissertation submitted in order to obtain the academic degree of
Master of Science in Chemical Engineering

Department of Chemical Engineering and Technical Chemistry
Chair: Prof. dr. ir. Guy Marin
Faculty of Engineering and Architecture
Academic year 2015-2016

UNIVERSITEIT GENT

ACKNOWLEDGEMENTS

Het schrijven van een dankwoord heeft iets euforisch en verlossends: eindelijk een punt zetten achter een intensieve periode waarin ik mezelf verrijkt heb, zowel op wetenschappelijk als op persoonlijk vlak. Een zeker gegeven is dat het schrijven van deze thesis gepaard ging met vallen en opstaan en het tot stand brengen ervan zou niet gelukt zijn zonder de hulp van een paar personen.

Allereerst zou ik prof. dr. ir. Guy B. Marin willen bedanken voor de kans om dit onderzoek uit te voeren aan het Laboratorium voor Chemische Technologie. Daarnaast zou ik mijn twee promotoren willen bedanken, prof. dr. ir. Joris W. Thybaut en dr. Vladimir V. Galvita, voor hun ideeën en advies die steeds een leidraad zijn geweest in de uitdieping van mijn onderzoek.

Een speciaal woord van dank gaat hierbij uit naar mijn begeleidster, Jolien De Waele, die mij steeds bijstond met raad en daad om te helpen bij elk probleem dat zich voordeed. Jolien, ik heb jouw enthousiasme en bereidheid echt enorm gewaardeerd en zonder onze boeiende gedachtewisselingen was deze thesis niet geworden wat hij nu is. Verder zou ik ook graag Alexandra Bouriakova, Anton De Vylder en de andere leden van de CaRE-groep willen bedanken voor de interessante discussies en suggesties rond mijn thesis en de leuke gesprekken tijdens de pauzes.

Leuke gesprekken en pauzes brengen mij dan ook bij het bedanken van al mijn medestudenten die ervoor gezorgd hebben dat deze jaren zullen blijven terugkomen wanneer ik nostalgisch zal terugdenken aan het studentenleven. Nick en Handan verdienen hierbij een speciale vermelding: het delen van de controlekamer was mede dankzij jullie een fijne belevenis en ik ben er zeker van dat niemand van ons nog zal vergeten zijn computer vergrendeld achter te laten. Een “dankjewel” ook aan Arne, Bert, Hans, Jens, Joeri, Lise, Michiel, Michiel, Stijn en Thomas, in het thesislokaal stond er altijd iemand klaar voor een koffie ’s ochtends vroeg of een pizza ’s avonds laat.

Als laatste zou ik graag mijn vriendin, Ellen, willen bedanken. Ook al bleef je kennis over mijn thesis meestal beperkt tot “katalysator” en “reactie”, je steun en vertrouwen zijn steeds een waardevolle hulp geweest gedurende mijn hele thesisperiode. En laat ons eerlijk zijn, mijn kennis van het Frans is ook niet echt top.

Bram De Maesschalck

1 juni 2016

UNIVERSITEIT GENT

FACULTY OF **ENGINEERING AND ARCHITECTURE**

Department of Chemical Engineering and Technical Chemistry
Laboratory for Chemical Technology
Director: Prof. Dr. Ir. Guy B. Marin

Laboratory for Chemical Technology

Declaration concerning the accessibility of the master thesis

Undersigned,

Bram De Maesschalck

Graduated from Ghent University, academic year 2015-2016 and is author of the master thesis with title:

Bio-ethanol dehydrogenation to acetaldehyde over PdZn/Mg(Al)O_x

The author gives permission to make this master dissertation available for consultation and to copy parts of this master dissertation for personal use.
In the case of any other use, the copyright terms have to be respected, in particular with regard to the obligation to state expressly the source when quoting results from this master dissertation.

1st of June 2016

Bio-Ethanol Dehydrogenation to Acetaldehyde over PdZn/Mg(Al)O_x

by

Bram DE MAESSCHALCK

Master's dissertation submitted in order to obtain the academic degree of
Master of Science in Chemical Engineering
Academic year 2015-2016

Supervisors: prof. dr. ir. Joris W. THYBAUT and dr. Vladimir V. GALVITA
Counsellor: ir. Jolien DE WAELE

Ghent University
Faculty of Engineering and Architecture
Department of Chemical Engineering and Technical Chemistry
Chairman: prof. dr. ir. Guy B. MARIN

Abstract The effect of the synthesis method and the presence of water in ethanol dehydrogenation to acetaldehyde has been investigated on a High Throughput Kinetics set-up using a PdZn supported on a mixed oxide catalyst, i.e., PdZn/Mg(Al)O_x. Due to their resemblance in electronic structure, along with a higher resistance against sintering, PdZn is the preferred substitute for conventional copper catalysts. Synthesis was performed by use of two methods, i.e., incorporation through coprecipitation and grafting through impregnation. The subsequent reduction was evaluated by variation of the number of oxidation-reduction cycles. Based on catalytic performance, the catalyst prepared via coprecipitation and larger number of reduction cycles pointed out to be superior in both conversion and selectivity to acetaldehyde. Furthermore, cokes deposition on this type of catalyst was reduced to a minimum while sintering was avoided. The effect of water was evaluated at the azeotropic composition of the feedstock, showing an increased tendency to ethanol decomposition.

Keywords ethanol dehydrogenation, acetaldehyde, PdZn, hydrotalcite based mixed oxides, intrinsic kinetics

Bio-Ethanol Dehydrogenation to Acetaldehyde over PdZn/Mg(Al)O_x

Bram De Maesschalck

Supervisors: Jolien De Waele, Vladimir V. Galvita, Joris W. Thybaut

Abstract **The effect of the synthesis method and the presence of water in ethanol dehydrogenation to acetaldehyde has been investigated on a High Throughput Kinetics set-up using a PdZn supported on a mixed oxide catalyst, i.e., PdZn/Mg(Al)O_x. Due to their resemblance in electronic structure, along with a higher resistance against sintering, PdZn is the preferred substitute for conventional copper catalysts. Synthesis was performed by use of two methods, i.e., incorporation through coprecipitation and grafting through impregnation. The subsequent reduction was evaluated by variation of the number of oxidation-reduction cycles. Based on catalytic performance, the catalyst prepared via coprecipitation and larger number of reduction cycles pointed out to be superior in both conversion and selectivity to acetaldehyde. Furthermore, cokes deposition on this type of catalyst was reduced to a minimum while sintering was avoided. The effect of water was evaluated at the azeotropic composition of the feedstock, showing an increased tendency to ethanol decomposition.**

Keywords **ethanol dehydrogenation, acetaldehyde, PdZn, hydrotalcite based mixed oxides, intrinsic kinetics**

I. Introduction

Increasing energy demands and growing climate concerns have introduced a variety of incentives in the search towards alternative fuel and chemical supplies. Bio-ethanol is already established as one of the prominent fuel alternatives with production capacities of over 1.6 million barrels per day [1]. Its use as a chemical building block, though, is rather restricted to marketing incentives such as the production of green polyethylene [2, 3].

A complete establishment is currently constrained, on the one side due to a lack in efficient conversion technology [4] and on the other side due to the water content in bio-ethanol, a common inhibitor for catalysis. Due to the intensive energy consumption of separation technologies such as azeotropic distillation, water removal cannot be considered economic [5]. Since the final goal is the production of chemicals, dehydrogenation to acetaldehyde is, therefore, proposed as alternative:

$$CH_3CH_2OH \rightarrow CH_3CHO + H_2$$

Because of its high reactivity, acetaldehyde is an important intermediate in the production of acetic acid, ethyl acetate, n-butanol, 1,3-butadiene, pyridines and other chemicals [6]. In addition, acetaldehyde will not form an azeotrope with water. That way, acetaldehyde shows the potential of being an alternative, green building block. Cu is the catalyst of choice during ethanol dehydrogenation, thanks to its ability of breaking the C-H bond while leaving the C-C bond intact [7]. Nonetheless, these catalysts show the disadvantage of rapid sintering [8]. Therefore, PdZn is introduced as a substitute for copper as it resembles the electronic structure [9] while Zn will prevent the Pd from sintering during reaction [10].

These materials are prepared via a hydrotalcite precursor which allows increasing the reproducibility of the catalyst and gives rise to a water resistant material. The latter is attributed to the memory effect of the hydrotalcite, resulting in restoring its original structure in the presence of water, without the destruction of the support [11].

II. Experimental

A. Catalyst synthesis

Mg(Al)(Pd)(Zn)O_x was synthesized via coprecipitation: for 20 g of catalyst, a 400 ml aqueous solution containing the metal nitrates with a Mg/Al/Pd/Zn ratio of 100/10-3x/x/2x, corresponding with 1 wt% of Pd and a 400 ml aqueous solution of 2.40 g of Na_2CO_3 and 22.60 g of NaOH were mixed by dropwise addition. The material was aged for 24 hours and consequently washed until neutral pH. Next, the catalyst was dried overnight and afterwards calcined ex-situ at 873 K after a temperature ramp of 4 hours. Finally, the catalyst was shaped into pellets of 250 to 500 µm.

Mg(Al)O_x was prepared via coprecipitation with a Mg/Al ratio of 10/1, via the method described above. Impregnation was performed in an ethanol solution containing 0.501 g of $Pd(NO_3)_2.2H_2O$ and 1.118 g of $Zn(NO_3)_2.6H_2O$. Afterwards, the catalyst was dried, calcined and shaped into pellets.

Before reaction, the catalyst was activated in-situ in the experimental set-up via altering oxidation-reduction cycles: $(red\text{-}ox)_x$-red. x will be either 0 (short cycle, s) or 2 (complete cycle, c). The catalysts, prepared via coprecipitation and impregnation are further addressed as incorporated and impregnated, respectively.

B. Catalyst characterization

X-ray diffraction (XRD) spectra of the catalysts were obtained with a Bruker-AXD D8 Discover using Cu Kα radiation (λ = 0.15405 nm). A combination with temperature programmed reduction (TPR) or oxidation (TPO) was carried out at a temperature ramp of 10 $K.min^{-1}$ in the presence of the corresponding gas.

Particle size distributions of the PdZn sites on the support were determined via Transmission Electron Microscopy (TEM). Metal dispersion values were obtained by D = 1.2/d, where d represents the average particle size determined by TEM.

Specific surface area measurements were carried out by means of N_2 adsorption-desorption experiments at 77 K using the method of Brunauer-Emmet-Teller (BET) (Tristar II, Micromeritics®).

E-mail: Bram.DeMaesschalck@UGent.be

C. Reaction experiments

Ethanol dehydrogenation was carried out in a High Throughput Kinetics Mechanistic Investigation (HTK-MI) set-up at the Laboratory for Chemical Technology [12]. This set-up consists of multiple stainless steel packed bed reactors. A weighted amount of 2 g of catalyst pellets was fed to the reactor and activated at 823 K via altering hydrogen and oxygen flows of 0.62 10^{-3} mol s^{-1}.

During reaction, ethanol was fed, diluted in nitrogen ($EtOH/N_2$: 5/95 mol%), at a space time of 36 kg_{cat} s mol^{-1}, a temperature of 533 K and a reactor pressure of 0.5 MPa. These conditions were verified a priori to validate the assumption of ideal plug flow behavior in the reactor and the absence of internal and external transport limitations.

The effluent analysis was carried out on a 3000 Micro GC (Agilent Technologies) containing four parallel columns and four thermal conductivity detectors. An alumina column was used for separation of the reaction products. Hexane was used as internal standard to verify the mass balance within 5 %.

Ethanol conversion (X_{EtOH}) and product selectivity (S_k) were calculated as follows:

$$X_{EtOH} = \frac{F_{EtOH,0} - F_{EtOH}}{F_{EtOH,0}} \quad (1)$$

$$S_k = \frac{C_k(F_k - F_{k,0})}{C_{EtOH}(F_{EtOH,0} - F_{EtOH})} \quad (2)$$

with C_k the number of carbon atoms for species k and F_k the corresponding molar flow rate. The subscript 0 will represent the inlet conditions.

III. Results and Discussion

A. Effect of synthesis

Four different catalysts were prepared, based on both synthesis methods and the two reduction procedures. XRD spectra of the reduced catalysts prepared via incorporation and impregnation are shown in Figure III-1. Besides the characteristic peaks of the MgO periclase, located at 37°, 43° and 62°, signals corresponding to the PdZn intermetallic compound could be identified. These are located at 31°, 42° and 44°. Other signals are assigned to ZnO not reduced upon activation.

It can be observed that the signals measured for the incorporated catalyst are more intense than the ones of the impregnated catalyst. This is assigned to the less uniform distribution of PdZn over the surface of the mixed oxide in case of the impregnated one, leading to destructive interference and thus broadening of the signal. BET surface areas for the incorporated and impregnated catalysts are, respectively, 62.6 and 53.0 m^2 g^{-1}. Hence, this shows the advantage of a more uniform surface distribution of PdZn.

TEM measurements point out this higher uniformity for the incorporated catalyst. Increasing the number of oxidation-reduction cycles gives rise to a narrower particle size distribution, see Table III-1. For the impregnated catalyst, a short cycle shows a dual distribution in the particle sizes. This is explained by the limited stability on the surface of the impregnated catalyst, leading to clustering towards higher particle sizes.

Table III-1: Structural properties of the catalysts

	Particle size (nm)	Dispersion (-)
Impregnated-s	5.5 ± 2.0 and 11.0 ± 2.0	0.204 ± 0.088
Impregnated-c	7.0 ± 2.3	0.174 ± 0.064
Incorporated-s	5.0 ± 2.5	0.283 ± 0.216
Incorporated-c	5.3 ± 1.8	0.229 ± 0.099

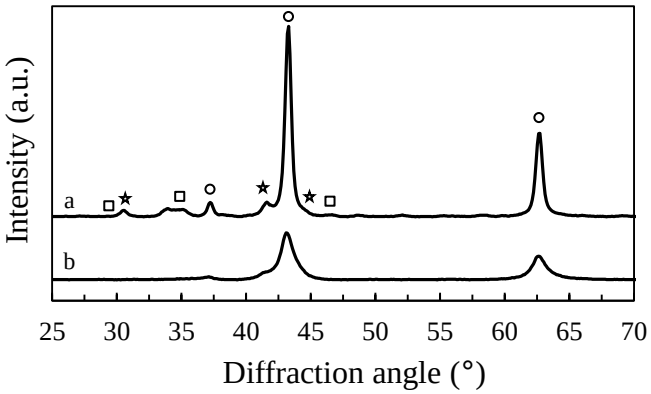

Figure III-1: XRD spectra of the incorporated (a) and the impregnated (b) catalyst (○: MgO; □: ZnO; ☆: PdZn)

Figure III-2 represents the deactivation curves for the different synthesized catalyst, showing the higher performance of the incorporated catalyst activated via a complete reduction cycle. Hence it could be indicated that a high uniformity of the surface, combined with a low particle size and thus higher dispersion will show superior results.

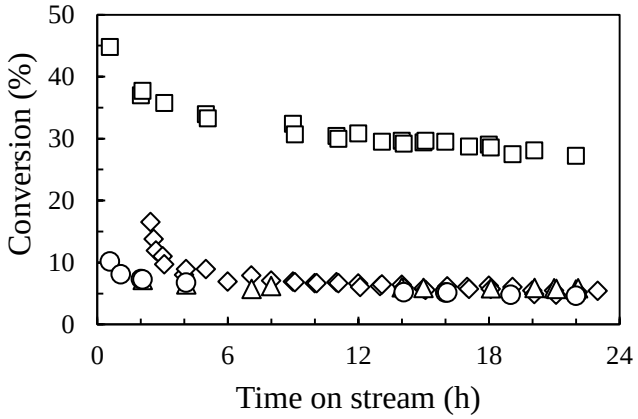

Figure III-2: Deactivation curves for impregnated-s (circles), impregnated-c (diamonds), incorporated-s (triangles) and incorporated-s (squares) (T = 533 K, p_{EtOH} = 25 kPa, space time = 36 kg_{cat} s mol^{-1})

Two different regions of deactivation could be assigned on these deactivation curves: within the first hours on stream a fast deactivation is observed while after a certain period of time, deactivation shows only restricted decreasing behavior, i.e., a stable region. TPO experiments show that cokes deposition on the surface of the catalyst is the reason for the fast initial deactivation of the catalyst. This is shown in Figure III-3. Metallic Pd sites, still present after reduction, increase the selectivity to ethanol decomposition:

$$CH_3CH_2OH \rightarrow CH_4 + CO + H_2$$

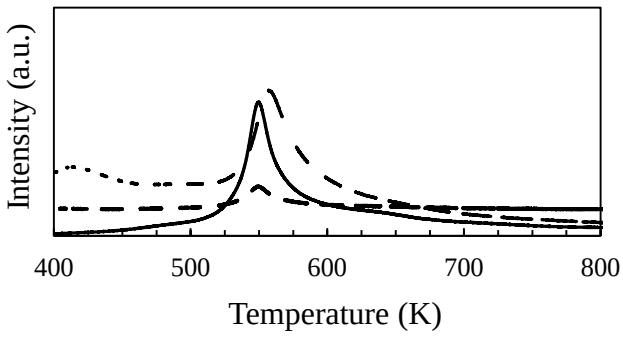

Figure III-3: Observed gas formation during TPO of incorporated-c (full: CO_2; dashed: CO; dotted: H_2O)

Table III-2: Catalytic and structural properties of the used catalysts

	Particle size (nm)	Dispersion (-)	CO_2 intensity (a.u.)	Conversion (%)	Selectivity (%) AcH	CH_4	EtOAc	EtOEt
Impregnated-s	n/a	n/a	$1.64\ 10^{-7}$	4.5	95.7	1.6	0.8	0.3
Impregnated-c	6.8 ± 2.0	0.196 ± 0.065	$1.19\ 10^{-7}$	5.4	92.8	2.5	0.7	1.5
Incorporated-s	7.6 ± 2.2	0.166 ± 0.060	$2.47\ 10^{-6}$	5.6	96.7	1.2	0.0	0.9
Incorporated-c	5.8 ± 1.5	0.228 ± 0.091	$1.55\ 10^{-7}$	27.6	97.6	0.5	0.9	0.5

These reaction products further give rise to the formation of cokes as a result of the Boudouard reaction or methane decomposition [13]. As these subsequently will cover the Pd sites, no further cokes will be formed and deposit on the surface. Cokes deposition shows the highest intensities for the catalysts with short reduction cycles. If one considers the ratio of the CO_2 intensity to the amount of ethanol converted, the incorporated-c catalyst points out to be the one the least affected by coking (Table III-2).

The restricted decrease in activity observed during the stable period could be assigned to sintering during reaction. Though, this is only observed for short reduction cycles as a complete one is sufficient to counter the sintering due to the increased stability of the PdZn intermetallic compound.

B. Stability for different regenerations

Figure III-4 shows the deactivation curves for different regenerations of incorporated-c and impregnated-c. Hence, regeneration via complete reduction cycles will not affect the performance of the catalyst. Short regeneration cycles, not shown, do not point out this ability indicating the necessity of a number of oxidation-reduction cycles. This will significantly reduce the time required for loading and unloading of the catalyst which is interesting for further experimental research or industrial operation.

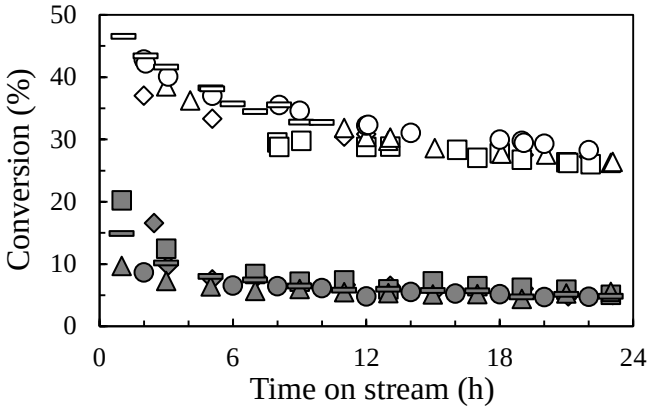

Figure III-4: Deactivation curves for incorporated-c (white) and impregnated-c (dark grey): fresh (diamonds), 1st regeneration (squares), 2nd regeneration (triangles), 3rd regeneration (circles) and 4th regeneration (stripes) (T = 533 K, p_{EtOH} = 25 kPa, space time = 36 kg_{cat} s mol^{-1})

Combined TPO and XRD after the regeneration-reaction cycles points out to have higher intensities of the PdZn signal up until temperatures of 700 K for the incorporated-c catalyst in comparison to others (Figure III-5). The spectra of the other catalysts, which are not shown, do not display these intensities, especially not up to 700 K, indicating the increased stability and a more uniform distribution of PdZn on the incorporated-c catalyst.

After oxidation, the oxides of Pd and Zn will redistribute across the surface of the catalyst but will not return to the bulk of the mixed oxide structure. As this will ease the consequent

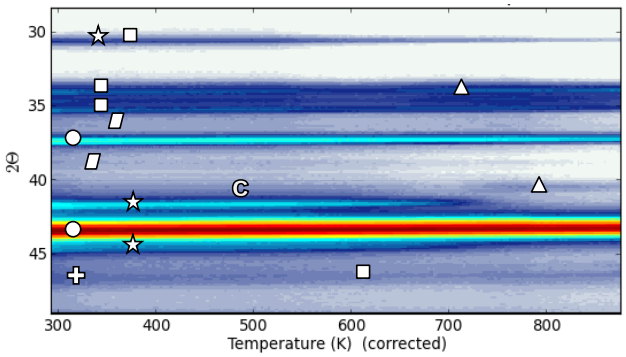

Figure III-5: TPO-XRD spectrum of used incorporated-c (△: PdO; □: ZnO; ✚ : Pd; ▱: Zn; ☆ : PdZn; ○: MgO; ©: cokes)

reduction to form the intermetallic compound, the benefit of sequencing oxidation and reduction cycles is proven.

C. Effect of water

The effect of water is evaluated for a reactor feed at the azeotropic composition, i.e., an ethanol/water weight ratio of 96/4. The conversion shows to be unaffected by the presence of water in the feed, i.e., 26.5 %. The selectivity, on the contrary, is favored to the decomposition of ethanol as shown in Table III-3.

Table III-3: Effect of the water content on the selectivity of the incorporated-c catalyst (T = 533 K, p_{EtOH} = 25 kPa, space time = 36 kg_{cat} s mol^{-1})

Water content (wt%)	Selectivity (%) AcH	CH_4	EtOAc	EtOEt
0	97.4	0.6	0.7	0.7
4	68.9	15.3	0.3	0.2

One would expect that the presence of water will induce the steam reforming of ethanol, though, the conditions to obtain the actual reforming, i.e., temperature and ethanol/water ratio, are far from reached [14]. A possible reasoning could therefore be the initialization of ethanol steam reforming through ethanol decomposition and a subsequent water gas shift [15]:

$$CH_3CH_2OH + H_2O \rightarrow CH_4 + CO_2 + 2H_2$$

Furthermore, steam could react with the cokes formed on the surface of the catalyst [16]:

$$C + H_2O \rightarrow CO + H_2$$

$$2C + 2H_2O \rightarrow CO_2 + CH_4$$

This removal of cokes will also enhance the accessibility of the metallic Pd sites, thus further increasing the selectivity to ethanol decomposition.

Regeneration of the catalyst indicates the presence of a higher fraction of metallic Pd, as reaction with pure ethanol still shows a high selectivity to methane. A possible argument for this phenomenon could be that water will affect the mixed oxide support by means of the memory effect. That way, the redistribution of the oxides will be impeded and the formation of PdZn limited upon regeneration. Nonetheless, further

characterization is required in order to understand the phenomena occurring at the surface.

IV. Conclusions and Future work

Ethanol dehydrogenation to acetaldehyde is performed on a PdZn intermetallic compound substituted on a mixed oxide support. Incorporation of Pd and Zn in the support via coprecipitation and subsequent activation via two reduction-oxidation cycles followed by a finishing reduction points out to have a superior performance over the other tested catalysts with a conversion of 27.6 % and a selectivity to acetaldehyde of 97.6 %.

Cokes deposition is minimal at the catalyst surface and limited to the initial region due to deposition on the metallic Pd sites, responsible for the actual coking. Sintering is not observed due to stabilization of the PdZn obtained via multiple reduction-oxidation cycles.

The presence of water will increase the selectivity to ethanol decomposition, possibly due to initialization of steam reforming or the removal of cokes from the surface. A more thorough analysis of the phenomena occurring at the surface is, however, required by means of characterization.

Acknowledgements

The authors would like to thank the European Research Council for funding under the European Union's Seventh Framework Programme (FP7/2007- 2013)/ERC grant agreement n° 615456

References

[1] Global ethanol production, U.S. Department of Energy, 2014.
[2] Axens, Total and IFPEN launch Atol™, an Innovative Technology for Bio-Ethylene Production Through Dehydration of Bio-Ethanol, 2014.
[3] I'm Green Polyethylene, Braskem, 2010.
[4] J.J. Bozell, G.R. Petersen, Technology development for the production of biobased products from biorefinery carbohydrates-the US Department of Energy's "Top 10" revisited, Green Chem, 12 (2010) 539-554.
[5] H.J. Huang, S. Ramaswamy, U.W. Tschirner, B.V. Ramarao, A review of separation technologies in current and future biorefineries, Sep Purif Technol, 62 (2008) 1-21.
[6] M. Eckert, G. Fleischmann, R. Jira, H.M. Bolt, K. Golka, Acetaldehyde, Ullmann's Encyclopedia of Industrial Chemistry, (2006).
[7] P. Chladek, E. Croiset, W. Epling, R.R. Hudgins, Characterization of copper foam as catalytic material in ethanol dehydrogenation, Can J Chem Eng, 85 (2007) 917-924.
[8] Y.J. Tu, Y.W. Chen, C.P. Li, Characterization of Unsupported Copper-Chromium Catalysts for Ethanol Dehydrogenation, J Mol Catal, 89 (1994) 179-190.
[9] Z.X. Chen, K.M. Neyman, A.B. Gordienko, N. Rosch, Surface structure and stability of PdZn and PtZn alloys: Density-functional slab model studies, Phys Rev B, 68 (2003).
[10] S.C. Shekar, J.K. Murthy, P.K. Rao, K.S.R. Rao, E. Kemnitz, Selective hydrogenolysis of dichlorodifluoromethane(CCl2F2) over CCA supported palladium bimetallic catalysts, Appl Catal a-Gen, 244 (2003) 39-48.
[11] V. Rives, Surface Texture and Electron Microscopy Studies of Layered Double Hydroxides, Layered Double Hydroxides: Present and Future, Nova Science Publishers, Inc. 2006.
[12] K. Van der Borght, K. Toch, V.V. Galvita, J.W. Thybaut, G.B. Marin, Information-Driven Catalyst Design Based on High-Throughput Intrinsic Kinetics, Catalysts, 5 (2015) 1948-1968.
[13] P.D. Vaidya, A.E. Rodrigues, Insight into steam reforming of ethanol to produce hydrogen for fuel cells, Chem Eng J, 117 (2006) 39-49.
[14] A. Haryanto, S. Fernando, N. Murali, S. Adhikari, Current status of hydrogen production techniques by steam reforming of ethanol: A review, Energ Fuel, 19 (2005) 2098-2106.
[15] A.N. Fatsikostas, X.E. Verykios, Reaction network of steam reforming of ethanol over Ni-based catalysts, Journal of Catalysis, 225 (2004) 439-452.
[16] J.G. Xu, G.F. Froment, Methane Steam Reforming, Methanation and Water-Gas Shift .1. Intrinsic Kinetics, Aiche Journal, 35 (1989) 88-96.

TABLE OF CONTENTS

LIST OF FIGURES

LIST OF TABLES

LIST OF ABBREVIATIONS

AcH	Acetaldehyde
BET	Brunauer-Emmet-Teller
BJH	Barrett-Joyner-Halenda
CH4	Methane
EtOAc	Ethyl acetate
EtOEt	Diethyl ether
EtOH	Ethanol
FID	Flame ionization detector
HE	Heat exchanger
HTK-MI	High throughput mechanistic investigation
HTlc	Hydrotalcite-like compound
IMC	Intermetallic compound
IS	Internal standard
LDH	Layered double hydroxide
MFC	Mass flow controller
Mg(Al)(Pd)(Zn)O_x	Pd and Zn incorporated in the mixed oxide
MSR	Methanol steam reforming
nC6	Hexane
PdO,ZnO/Mg(Al)O_x	Pd and Zn impregnated on the mixed oxide
PdZn/Mg(Al)(Pd)(Zn)O_x	Pd and Zn incorporated in the mixed oxide and reduced
PdZn/Mg(Al)O_x	Pd and Zn impregnated on the mixed oxide and reduced
PFR	Plug flow reactor
PONA	Paraffins, olefins, naphthenes and aromatics
RS	Relative sensitivity
RT	Retention time
SEM	Scanning electron microscopy
TCD	Thermal conductivity detector
TEM	Transmission electron microscopy
TPO	Temperature programmed oxidation
TPR	Temperature programmed reduction
V	Valve
WF	Weight factor
XANES	X-ray absorption near edge structure
XRD	X-ray diffraction

LIST OF SYMBOLS

GREEK SYMBOLS

α	Heat transfer coefficient over the film [W m_i^{-2} K^{-1}]
α_w	Heat transfer coefficient between bed and reactor wall [W m_r^{-2} K^{-1}]
β	Half width of signal [-]
$\Delta_{cond}H$	Condensation enthalpy [J mol^{-1}]
ΔH_X	Adsorption enthalpy of component X [J mol^{-1}]
$\Delta_r G°$	Standard Gibbs free reaction energy [J mol^{-1}]
$\Delta_r H$	Reaction enthalpy [J mol^{-1}]
$\Delta_r H°$	Standard reaction enthalpy [J mol^{-1}]
$\Delta rS°$	Standard reaction entropy [J mol^{-1} K^{-1}]
ΔS_X	Adsorption entropy of component X [J mol^{-1} K^{-1}]
ε_B	Porosity of the bed [m_f^3 m_r^{-3}]
$1-\varepsilon_B$	Fraction of reaction volume, occupied by catalyst bed [m_B^3 m_r^{-3}]
ε_p	Porosity of the catalyst pellet [m_f^3 m_p^{-3}]
Θ	Angle of incidence [-]
θ_i	Fraction of sites occupied by component i [-]
Λ	Wave length of the incident radiation [m]
λ	Heat conduction coefficient [W m^{-1} K^{-1}]
λ_{er}	Effective radial heat conductivity [W m_r^{-1} K^{-1}]
λ_p	Heat conduction coefficient of catalyst pellet [W m_p^{-1} K^{-1}]
μ	Dynamic viscosity [kg m_f^{-1} s^{-1}]
ν_i	Stoichiometric coefficient of component i [-]
ρ	Density [kg m^{-3}]
ρ_f	Density of the fluid [kg m_f^{-3}]
ρ_p	Density of the catalyst pellet [kg_{cat} m_p^{-3}]
ρ_{PdZn}	Density of the PdZn intermetallic compound [kg m^{-3}]
σ	Surface density of PdZn molecules [m^{-2}]
τ_0	Residence time of the reactor [s]
$\tau_{0,P}$	Residence time of the reactor with ideal plug flow regime [s]
τ_B	Tortuosity of the bed [m^2 m^{-2}]
τ_p	Tortuosity of the catalyst pellet [m^2 m^{-2}]
χ	Ratio of the desorption rate coefficients of the first and second layer, measure for the activation energy, bearing in mind condensation: $cst \exp[-\frac{E_d-\Delta_{cond}H}{RT}]$

ROMAN SYMBOLS

<L>	Dimension of the particle in the direction perpendicular to the reflecting plane [m]
a	Constant for the contribution in the turbulent regime [-]
A	Pre-exponential factor [mol s^{-1} m^{-3} (mol s^{-1} m^{-3})$^{-n}$]

$A_{e,i}$	True GC area of component i [-]
A_i	Measured GC area of component I [-]
a_i	Activity of component i [-]
a_m	Surface area taken by one adsorbed molecule, i.e., 0.162 nm² for N_2
a_s	Internal surface area [$m^2\ kg_{cat}$]
a_s	Specific external surface area [$m_i^2\ kg_{cat}^{-1}$]
a_v	Volumetric surface area at which reaction occurs [$m_i^2\ m^{-3}$]
b	Volume of inert material as fraction of total volume of solids [$m^3_{inert} m^{-3}_{inert+catalyst}$]
1-b	Fraction of catalyst bed, occupied by catalyst pellet [$m_p^3\ m_B^{-3}$]
C_A	Concentration of A [mol m^{-3}]
$C_{A,0}$	Inlet concentration of A [mol m^{-3}]
$C_{A,b}$	Concentration of A at bulk conditions [mol m^{-3}]
$C_{a,i}$	Number of atoms a in component i [-]
$C_{A,s}$	Concentration of A at surface conditions [mol m^{-3}]
C_t	Number of active sites at the surface [mol kg_{cat}^{-1}]
c_p	Specific heat capacity [J $kg^{-1}\ K^{-1}$]
d	Distance between two crystallographic planes [m]
D	Dispersion of the catalyst [-]
D_A	Molecular diffusion coefficient [$m_f^2\ s^{-1}$]
$D_{A,e}$	Effective diffusion coefficient [$m_f^3\ m_p^{-1}\ s^{-1}$]
D_{ea}	Effective axial diffusion coefficient [$m^2\ s^{-1}$]
D_{er}	Effective radial diffusion coefficient [$m^2\ s^{-1}$]
d_p	Pellet diameter [m]
d_{PdZn}	Particle diameter of PdZn [m]
d_t	Tube diameter [m]
E_a	Activation energy [J mol^{-1}]
E_d	Activation energy for desorption [J mol^{-1}]
F	Frequency of the corresponding particle diameter [-]
f	Friction factor [-]
$F_{A,0}$	Inlet flow rate [mol s^{-1}]
f_B	Friction factor for a packed bed [-]
F_i	Molar flow rate of component i [mol s^{-1}]
G	Gibbs free energy of the system [J mol^{-1}]
H	Enthalpy of the system [J mol^{-1}]
K	Shape factor, often taken as 1 [-]
k	Rate coefficient of the first order reaction of A [s^{-1}]
$k_{f,A}$	Mass transfer coefficient [$m_f^3\ m_i^{-2}\ s^{-1}$]
k_v	Volumetric rate coefficient [s^{-1}]
L	Length of the reactor [m]
L_p	Length of the reactor with ideal plug flow regime [m]
m	Order of reflection [-]
MM_i	Molar mass of component i [g mol^{-1}]

MM_{PdZn}	Molecular mass of the PdZn intermetallic compound [kg mol^{-1}]
n	Reaction order [-]
N_A	Avogadro number [6.022 10^{23} mol^{-1}]
$N_A\|_{r'=1}$	Flux through the external surface of the catalyst pellet [mol m_i^{-2} s^{-1}]
p	Pressure [Pa]
p_0	Vapor pressure of the adsorbed component [Pa]
$PdZn_s$	Number of PdZn atoms at the surface of the catalyst [-]
$PdZn_t$	Number of PdZn atoms in the catalyst [-]
Pe_a	Péclet number (axial) [-]
p_i	Partial pressure of component i [Pa]
P_{tot}	Reactor pressure [Pa]
R	Gas constant [8.314 J mol^{-1} K^{-1}]
$Re_{p,B}$	Reynolds number around catalyst pellet in a packed bed [-]
RS_i	Relative sensitivity of component I [-]
$R_{w,A}^{b}$	Specific production rate of A at bulk conditions [mol s^{-1} kg_{cat}^{-1}]
$R_{w,A}^{int}$	Intrinsic specific production rate of A (mol s^{-1} kg_{cat}^{-1})
$R_{w,A}^{obs}$	Observed specific production rate of A (mol s^{-1} kg_{cat}^{-1})
$r_{w,A}^{obs}$	Observed specific reaction rate [mol s^{-1} kg_{cat}^{-1}]
S	Entropy of the system [J mol^{-1} K^{-1}]
S_k	Selectivity to component k [-]
S_p	Surface of the catalyst pellet [m_p^2]
T	Temperature [K]
T_b	Temperature at the bulk [K]
T_s	Temperature at pellet surface [K]
T_{wi}	Internal wall temperature [K]
u_s	Superficial velocity [m s^{-1}]
V_0	Adsorbed volume at solely monolayer adsorption [m^3]
V_a	Adsorbed volume [m^3]
V_p	Volume of catalyst pellet [m_p^3]
W	Catalyst weight [kg_{cat}]
WF_i	Weight factor of component i [-]
x	Constant generally in the order of magnitude of the highest frequency [-]
X_A	Conversion of A [-]
X_{dil}	Conversion obtained with the diluted bed [-]
y	Constant representing the average particle diameter [m]
$y_{f,A}$	Film factor [-]
y_i	Weight percentage of component i [-]
z	Constant representing the standard deviation on the particle diameter [m]

Chapter 1: General Introduction

1 WHY ETHANOL DEHYDROGENATION?

Increasing energy demands and growing climate concerns have introduced a variety of incentives in the search towards alternative fuel and chemical supplies. An important barrier within the quest of fuel substitutes is the price of alternative raw materials such as biomass which significantly increases the eventual selling price. Bio based chemicals, on the contrary, do not show this disadvantage as the cost of the production process will have a higher impact and could thus be reduced via process optimization.

Nonetheless, bio based chemical production via so called drop-in replacements lacks in competitive processes and thus economic viability to take on their fossil based counterparts [1]. So, recent research has been focusing on alternative, new conversion routes towards valuable chemicals such as butadiene, ethyl acetate or acetaldehyde using a different building block than the conventional petroleum derived ones: ethanol. Ethanol is already established as one of the prominent fuel alternatives with production capacities of 1.6 million barrels per day (2014) [2]. Its use as chemical building block, though, is rather restricted to marketing incentives such as the production of green polyethylene by Braskem or more recently by Total with the demonstrated Atol™ technology for the production of polymer grade ethylene via dehydration of bio-ethanol [3]. A complete establishment is currently constrained, on the one side due to lack of conversion technology but on the other side due to the water content of bio-ethanol. Since water is a common inhibitor in catalysis, removal is appropriate but expensive due to the formation of an azeotrope [4]. To counter this bottleneck, an alternative conversion of ethanol to acetaldehyde will be proposed. As acetaldehyde does not show the disadvantage of a water containing azeotrope, separation of water via distillation will be straightforward and less energy intensive. In addition, acetaldehyde also shows the potential of being a platform molecule for the production of chemicals such as 1,3-butadiene or n-butanol.

Conventionally, the most opted catalyst applied in the dehydrogenation of ethanol to acetaldehyde is based on copper as the active metal site. These materials are known for their high selectivity and activity but have the disadvantage of a fast deactivation due to sintering represented by a conversion decrease of approximately 30 % over 4 hours [5]. Due to their resemblance in electronic structure, an

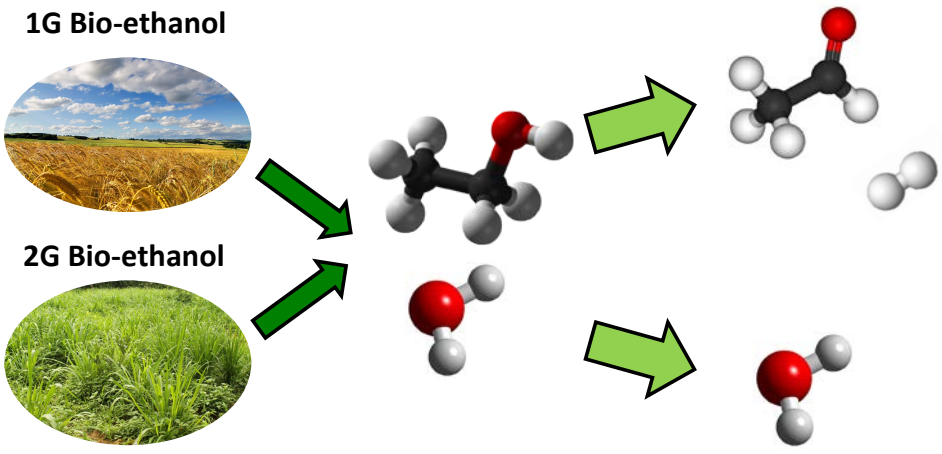

Figure 1-1: From bio-ethanol to acetaldehyde

intermetallic compound will be proposed during this work as an alternative: PdZn. Besides altering the electronic structure, Zn will also prevent Pd from sintering, countering, as such, the general disadvantage of the conventional catalyst [6]. These materials will be prepared via a hydrotalcite precursor which allows increasing the reproducibility of the catalyst and gives rise to a water resistant material. The latter is due to the memory effect of the hydrotalcite resulting in restoring the original structure in the presence of water, without destruction of the support [7]. In such manner, a catalyst could be developed, able to ameliorate the performance of conventional catalysis without dealing with the bottlenecks encountered with them.

2 THE AIM OF THIS WORK

The approach applied for the catalyst and reactor optimization in ethanol dehydrogenation fits within the expertise of the Laboratory for Chemical Technology at Ghent University and is shown in Figure 1-2. In a first step, synthesis of the catalyst is based on data obtained from literature and subsequent testing is executed on the performance. During this work, the focus lies within the first two steps of the process in order to gather more information towards a modeling approach. This approach was described by Van der Borght et al. as information driven catalyst design (Figure 1-3) in which the experimental workload will be limited to a mechanistic investigation of the catalysts, followed by modeling towards an ideal catalyst performance [8]. This mechanistic investigation will be performed on a high throughput kinetics set-up. The effect of conditions such as temperature and pressure are not necessarily tested at the most optimal conditions but rather at the conditions which allow acquiring the most detailed mechanistic investigation, bearing in mind limitations on the set-up or limitations on the pellet or reactor scale due to transport phenomena.

The mechanistic investigation will then form the basis for kinetic model development in which kinetic and catalyst descriptors are introduced. The former will hereby comprise of parameters specifying the kinetics of the reaction irrespective from the catalyst, while the latter will link the performance of the catalyst with the reaction's kinetics and allow, as such, optimization of the catalyst design [9]. This modeling approach will not belong to the scope of this work, though, an incentive will be provided towards the development of the kinetic model.

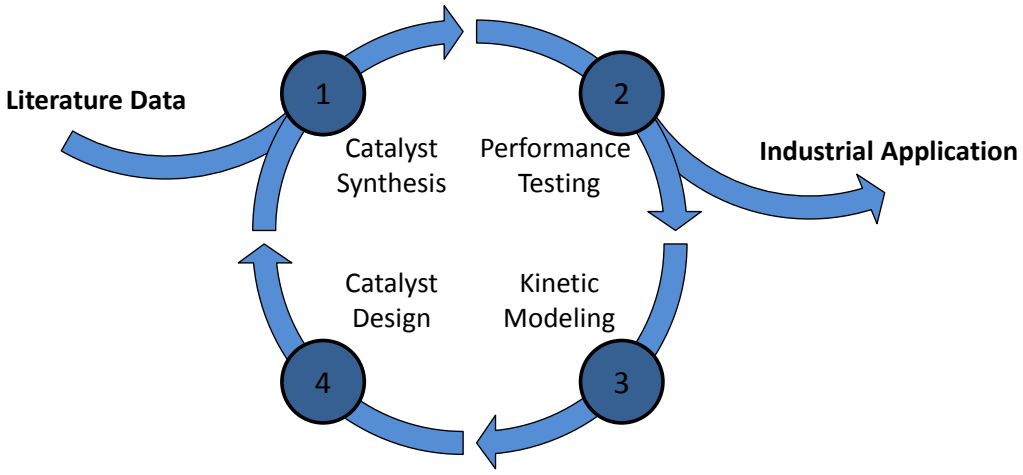

Figure 1-2: Catalytic approach towards ethanol dehydrogenation [10]

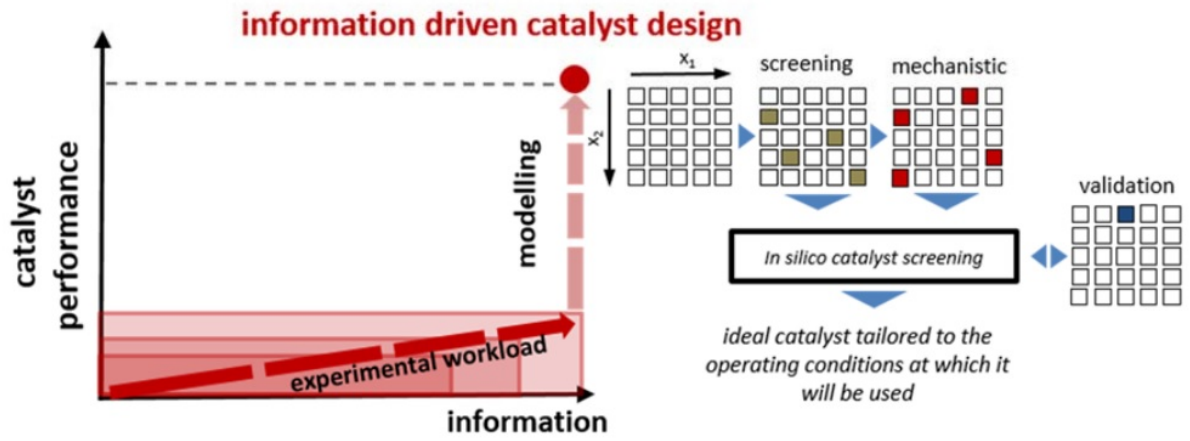

Figure 1-3: Information driven catalyst design [8]

3 REFERENCES

[1] J.J. Bozell, G.R. Petersen, Technology development for the production of biobased products from biorefinery carbohydrates-the US Department of Energy's "Top 10" revisited, Green Chem, 12 (2010) 539-554.
[2] Global ethanol production, U.S. Department of Energy, 2014.
[3] Axens, Total and IFPEN launch Atol™, an Innovative Technology for Bio-Ethylene Production Through Dehydration of Bio-Ethanol, 2014.
[4] H.J. Huang, S. Ramaswamy, U.W. Tschirner, B.V. Ramarao, A review of separation technologies in current and future biorefineries, Sep Purif Technol, 62 (2008) 1-21.
[5] Y.J. Tu, Y.W. Chen, Effects of alkali metal oxide additives on Cu/SiO2 catalyst in the dehydrogenation of ethanol, Ind Eng Chem Res, 40 (2001) 5889-5893.
[6] S.C. Shekar, J.K. Murthy, P.K. Rao, K.S.R. Rao, E. Kemnitz, Selective hydrogenolysis of dichlorodifluoromethane(CCl2F2) over CCA supported palladium bimetallic catalysts, Appl Catal a-Gen, 244 (2003) 39-48.
[7] V. Rives, Surface Texture and Electron Microscopy Studies of Layered Double Hydroxides, Layered Double Hydroxides: Present and Future, Nova Science Publishers, Inc. 2006.
[8] K. Van der Borght, K. Toch, V.V. Galvita, J.W. Thybaut, G.B. Marin, Information-Driven Catalyst Design Based on High-Throughput Intrinsic Kinetics, Catalysts, 5 (2015) 1948-1968.
[9] J.W. Thybaut, G.B. Marin, Single-Event MicroKinetics: Catalyst design for complex reaction networks, J Catal, 308 (2013) 352-362.
[10] J.W. Thybaut, Kinetic Modeling and Simulation, Ghent University, 2014.

Chapter 2: Literature Review

1 INTRODUCTION

In this chapter a literature review will be performed on the dehydrogenation of ethanol to acetaldehyde. The focus of this review will cover process, starting from biomass, towards acetaldehyde via the bio-ethanol route. Attention is paid towards the major drawback, i.e., the water content in bio-ethanol, as this effect is investigated later on in this work.

A second part will focus specifically on the different pathways towards acetaldehyde, concentrating on the catalysis applied in these processes. An overview will be given on the current state of the art, along with their bottlenecks. The PdZn/Mg(Al)O_x, an abbreviation for a PdZn intermetallic compound, substituted in a hydrotalcite derived structure, are at the center of this study and consequently elaborated on. Hereby is focused on their role in catalysis and how they will counter the bottlenecks obtained in the conventional processing of bio-ethanol.

2 THE POTENTIAL OF BIO-ETHANOL

During the last few decades, globalization has led to increasing energy demands making depleting petroleum supplies a common problem. According to Exxon Mobil's *The Outlook for Energy 2015*, the global oil demand is expected to increase from 89 MBD in 2010 to 115 MBD in 2040, an increase of almost 30 percent [1]. These shortages, along with growing concerns regarding climate change, have been a major driving force towards the exploration of alternative resources for energy and chemicals production.

One of the most promising alternatives to replace the fossil resources, both for the production of fuels and chemicals, is biomass. Since these products are, in principle, CO_2 neutral and could contribute as such to solving environmental issues, the production of bulk chemicals from bio-derived sources could be considered an interesting option. Along with the benefit of limiting the dependency on oil resources, this creates an opportunity for a new concept: biorefineries. A biorefinery can be defined as a facility that integrates biomass conversion processes and equipment to produce fuels, power and chemicals from biomass. Its concept resembles today's petrochemical refineries which produce a variety of fuels and products from crude oil [2].

Fuels are known to be high volume but low value products making the development of alternative routes more an energetic and environmental necessity than an economic opportunity. Chemicals, on the contrary, represent only a small percentage of the total processed fossil feedstock but offer much higher economic prospects. This simultaneous production of both renewable chemicals and fuels could, as such, proceed in reaching both its energetic and economic targets by reducing the dependency on fossil resources while at the same time representing a competitive bio based alternative. Furthermore, the generation of electricity and process heat will provide the refinery's utilities, reducing in this manner operating expenditure [2-7]. An overview of a biorefinery based on lignocellulosic feedstock is shown in Figure 2-1. During this review, the upper pathway via cellulose will be of particular interest.

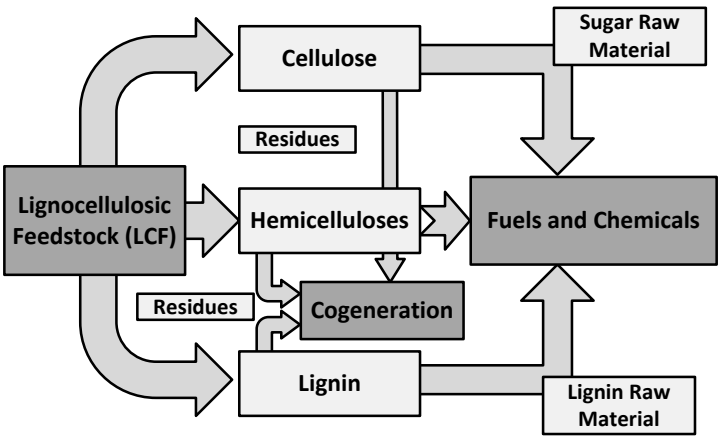

Figure 2-1: Concept of a biorefinery based on lignocellulosic feedstock [7]

From all starting molecules produced out of biomass, ethanol has proven to possess the highest potential. With a capacity of approximately 1.6 million barrels per day, biochemical transformation of biomass by fermentation to ethanol, nowadays, accounts for more than 75 % of global biofuel production (Figure 2-2). Though, this was also the reason why ethanol was, at first, not considered as a potential platform molecule but rather as so-called major commodity. Recent technology developments and strategic commercial partnerships have positioned ethanol as a feedstock for chemical production, improving its platform potential [3].

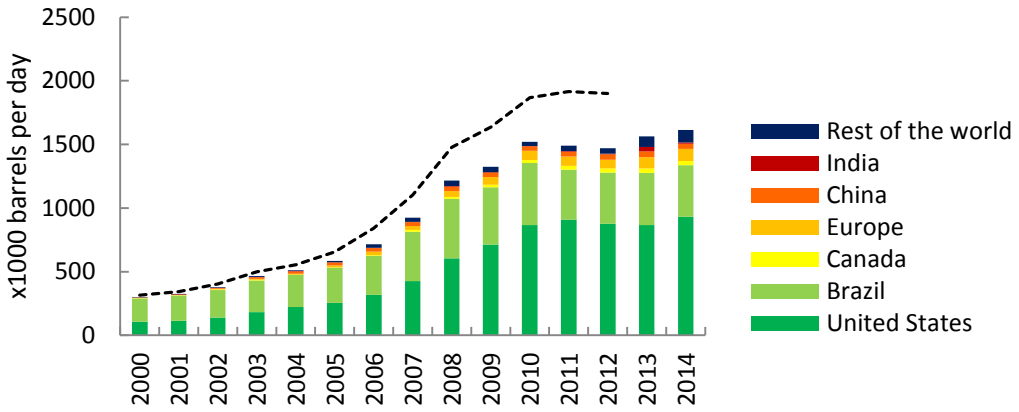

Figure 2-2: Global ethanol production 2000-2014 in comparison to the global biofuel production (statistics available up to 2012) [8, 9]

2.1 PRODUCTION OF BIO-ETHANOL

Major production facilities are located in the United States and Brazil and represent 83 % of the world's share. Though, opportunities to reduce oil imports, boost rural economies and improve air quality have proven to be large incentives for the production of bio-ethanol in other countries, e.g., Thailand, China and Argentina [10-12]. Up to the present day, the general feedstock for the production of bio-ethanol is sugar cane, wheat and corn. A drawback of the conventional fermentation process is the competition with food industry and concerns about ecological systems. For these reasons, current research has shifted almost entirely to second generation processes in which non-food biomass feedstock (e.g., lignocellulose) is used. While first generation processes are only effective for processing sugar- and starch-rich materials, such as sugar cane, second generation fermentation plants also allow converting most of the lignocellulose to chemicals. In this way, a higher yield of ethanol is possible, even though a similar amount of energy consumption and higher CO_2 reductions can be achieved [13, 14]. Recently, new, third generation processes where suggested in which the starch- and cellulose-rich residue of algae processing, for the production of biodiesel, is used as source for ethanol. The resulting combined biodiesel/bio-ethanol production offers an additional advantage as the produced CO_2 can be captured and used internally. Since algae are processed, also no competition is present with conventional agriculture. Though, these processes are, so far, not viable for industrial application [10, 15-17].

An overview of the production routes for the different generations of bio-ethanol, as integrated in a biorefinery, is shown in Figure 2-3. The processes are equivalent downstream of the fermentation step. These fermentation reactions proceed one to approximately three days at 298-314 K in the presence of yeast and nutrients. Consequently, distillation will separate the ethanol up to its azeotropic point with water. The residual flow of the separation section is known as vinasse or stillage and is further processed into biogas for the production of heat and power (as illustrated in Figure 2-3) or animal food, fertilizer and other side products [10]. Upstream of the fermentation process, the pretreatment section will mainly consist of grinding, milling and detoxification processes. In the case of first generation feedstock, a saccharification step is included for the conversion into sugars with enzymes [18].

2.2 ADDRESSING THE WATER CONTENT

Downstream of the fermenter, an aqueous solution is obtained consisting of approximately 5-12 wt% of ethanol. As is illustrated in Figure 2-3, further separation is required to obtain anhydrous ethanol which is suitable for further processing or blending with fuels. Separation of ethanol from the aqueous solution is, however, an energy-intensive process and will uptake a large fraction of the total energy requirement for the whole biorefinery. Moreover, the dehydration of ethanol encounters a second bottleneck as ethanol forms a minimum boiling azeotrope with water (95.6 wt% ethanol at a boiling point of 78.15 °C) which makes it impossible to separate ethanol and water in a single distillation column [18].

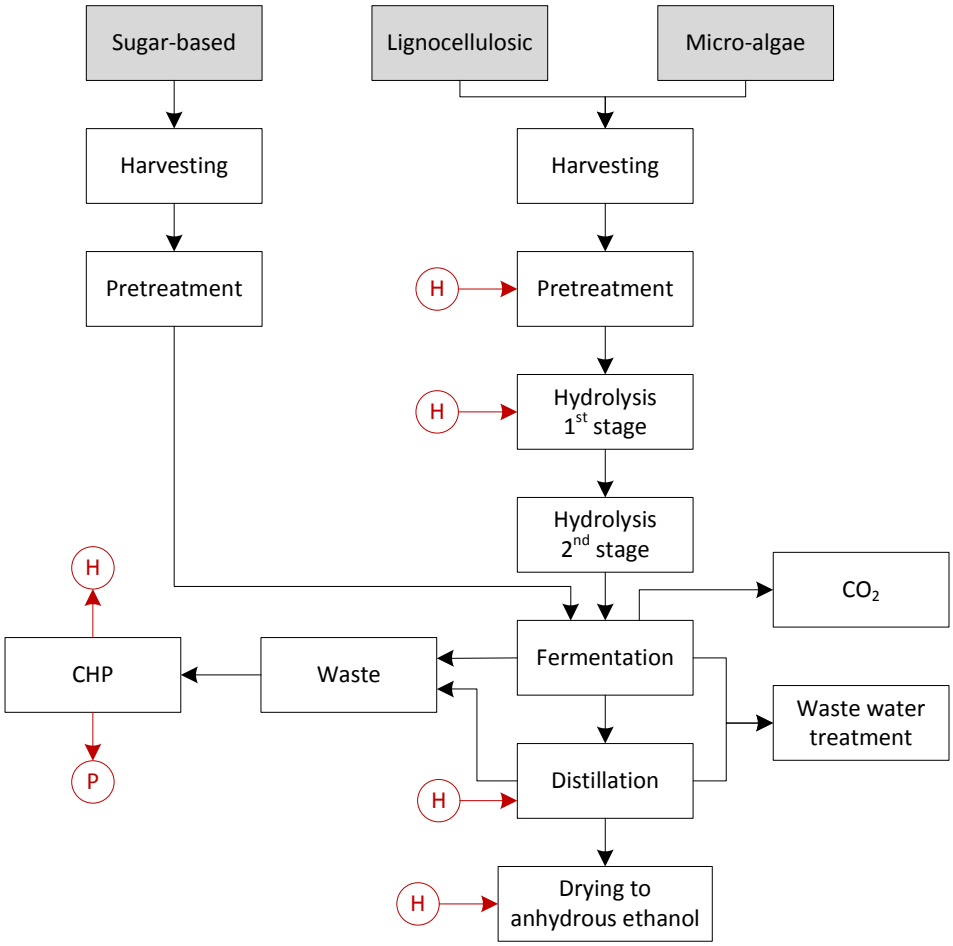

Figure 2-3: Ethanol production process for different generations of bio-ethanol (CHP: combined heat and power; H: heat; P: power) [10]

The separation of the dilute ethanol-water mixture is usually divided into two large steps: first, a more concentrated solution of ethanol is obtained via conventional distillation which is reported to be approximately 92.4 wt% as according to Huang et al. [18]. In general, this operation will comprise two columns (Figure 2-4) [18, 19]. Decreasing the pressure (to approx. 12.7 kPa) in order to break the azeotrope would result in a higher concentration, i.e., pressure swing distillation. Though, this cannot be considered as economically attractive. Therefore, further concentration is required to achieve anhydrous ethanol. Several alternatives are available and well described such as:

- Azeotropic distillation
- Extractive distillation
- Adsorption
- Pervaporation and vapor permeation
- Liquid-liquid extraction
- Hybrid processes

Azeotropic distillation will involve a third volatile component, the entrainer, added to form a ternary azeotrope and increase the efficiency of separation. As these entrainers will introduce the formation of a second phase in the mixture, the process is also known as heterogeneous azeotropic distillation. A representation of the flowsheet is shown in Figure 2-5. The formed ternary azeotrope will be separated from the dehydrated ethanol and is subsequently divided in an organic phase (ethanol and entrainer) and aqueous phase (water and entrainer). The former is refluxed while the latter is processed in entrainer recovery. Benzene is known as a traditional entrainer for the heterogeneous azeotropic distillation for ethanol dehydration. However, due to its carcinogenic effects, benzene has been substituted by other solvents such as cyclohexane. Though, cyclohexane has the disadvantage of flammability. Due to these health and safety concerns of either carcinogenic (benzene) or highly flammable (cyclohexane) solvents, azeotropic distillation is less applied in ethanol production [18, 20, 21].

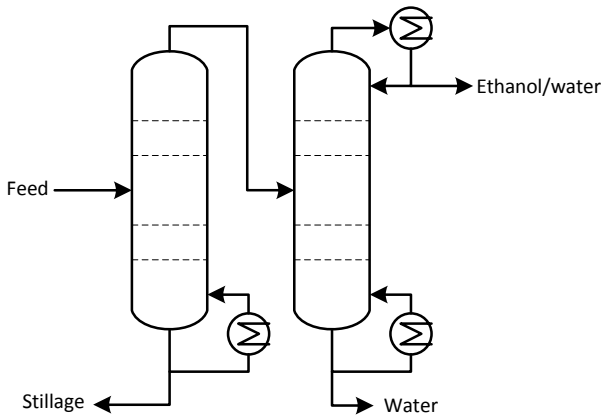

Figure 2-4: Preliminary distillation of water [19]

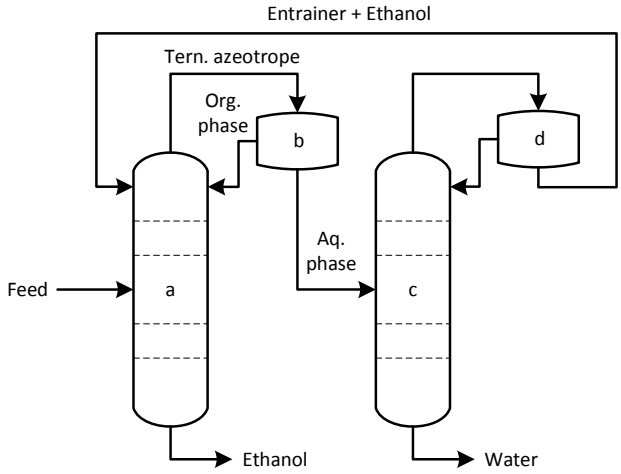

Figure 2-5: Azeotropic distillation of ethanol-water mixture (a: azeotropic column; b: decanter; c: entrainer recovery; d: condenser) [18]

Extractive distillation will, as was the case for azeotropic distillation, introduce a third component to increase the efficiency of separation between ethanol and water. This third high boiling component can either be a liquid solvent, ionic liquid, dissolved salt, a mixture of previous or a hyper-branched polymer as described by Huang et al. [18]. In order to give a brief overview, only the first type will be discussed here.

The typical extractive distillation for ethanol dehydration is illustrated in Figure 2-6. A suitable amount of high-boiling solvent is introduced in the separation column which is removed at the bottom along with the water, while dehydrated ethanol is removed at the top. The solvent-water mixture is subsequently sent to a solvent recovery column for further separation of both components. One of the commonly used solvents for this operation is ethylene glycol.

Due to the two-column system, distillation methods such as extractive and azeotropic distillation represent relatively high energy and investment costs but in spite of these major drawbacks, they are still considered as the option of choice in case of large scale production of bio-ethanol. Innovative solutions could overcome these energy intensive operations in terms of process intensification and integration. Examples are thermally coupled distillation columns, divided wall columns or thermal integration [19-21].

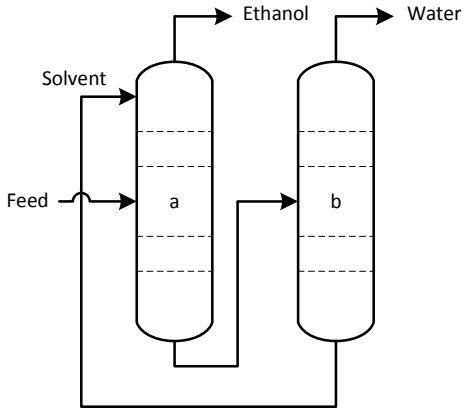

Figure 2-6: Extractive distillation of ethanol-water mixture (a: extractive distillation; b: solvent recovery) [18]

Another way of preventing the extensive energy consumption and investment cost accompanying the use of distillation systems, is by applying an adsorption dehydration system with hydrophilic zeolite molecular sieves. Since water molecules are both smaller and more polar than ethanol molecules, separation via adsorption becomes possible. Adsorption systems consume significantly less energy than distillation systems. However, the application of these systems requires high temperatures and/or low pressures for desorption, increasing thus the investment costs of the operation [18, 19, 21].

During last decades, strong developments could be considered in azeotropic separation through membrane pervaporation and vapor permeation as these techniques show themselves as competitive alternatives for molecular sieve adsorption. Unlike the cyclic nature of adsorption, pervaporation and vapor permeation can be operated continuously. Applied on ethanol dehydration,

a hydrophilic membrane will be applied, selectively transporting water. In the case of pervaporation, feed and retentate will be in the liquid phase which is in contrast to vapor permeation that requires everything in the vapor phase, limiting the temperatures at which it could be applied. Pervaporation is illustrated in Figure 2-7. Due to their superior energy efficiency in comparison to the other techniques, membrane adsorption offers an attractive alternative for ethanol dehydration. However, they do reach their limits in case of large scale separations [20-22].

At last, liquid-liquid extraction can be considered a theoretical possibility, although, neither commercial application nor experimental investigation is performed on this option. In literature, some investigation is performed on hybrid solutions, combining separation methods, e.g., membrane distillation, though, on a restricted basis [18]. It is worth considering that the final separation step of the azeotropic mixture is a real bottleneck requiring high capital and/or operating expenditure. Therefore, the focus of this work will not solely lie within processing of anhydrous ethanol.

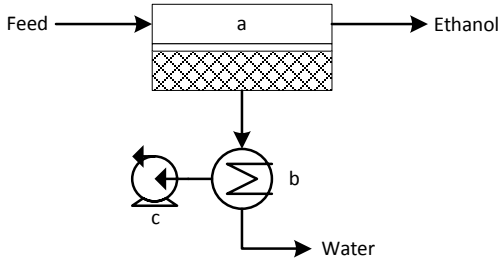

Figure 2-7: Pervaporation of ethanol-water mixture (a: membrane module; b: condenser; c: vacuum pump) [22]

2.3 PRODUCTION OF CHEMICALS FROM BIO-ETHANOL

Although most of the developments are mainly driven by the use of bio-ethanol as a biofuel, any increase in production volume or decrease in price will make the application of bio-ethanol for the production of higher-value chemicals more attractive from an economic point of view. The biggest challenges here are related to the development of novel high performance catalysts to exploit the potential of ethanol as platform molecule [4]. As shown in Figure 2-8, a number of important bulk chemicals can be produced from ethanol [6].

The direct replacement of the current building blocks originating from fossil resources with their identical green variant has the advantage that the infrastructure is already established. Such 'drop in' alternatives are therefore easier to introduce [6]. A striking example is bio based ethylene, illustrated in Brazil by the commissioning of a commercial plant by Braskem in 2010. Using ethanol derived from sugar cane as feedstock the facility produces 200,000 metric tons of green polyethylene per year. However, this is in stark contrast to the annual worldwide demand of high density polyethylene (HDPE), i.e., 5.6 million metric tons in Europe alone [23], indicating that only a small fraction of the commercially produced ethylene can be replaced by its green alternative [24, 25].

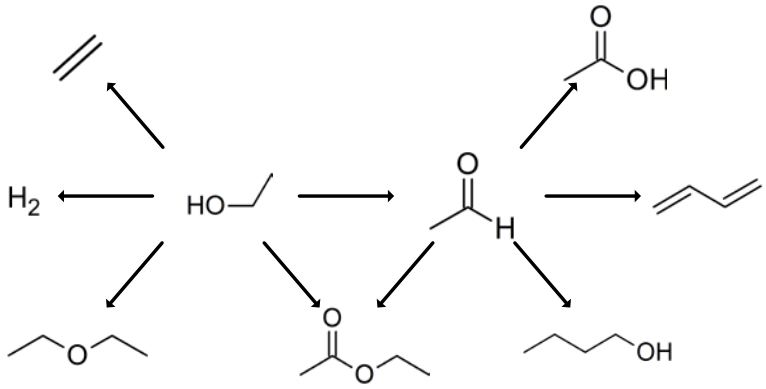

Figure 2-8: Ethanol as green platform molecule [15]

Production of ethylene seems the most interesting option for converting ethanol due to its wide application, though, from an economic and energetic point of view, it would be more viable to produce oxygenated compounds. Fossil resources typically lack oxygen containing building blocks. Since oxidation reactions involve product loss owing to overoxidation, it would be desirable to avoid these reactions as much as possible. Since biomass derived products already contain some oxygen, the production of oxygenated compounds via these chemicals seems the most obvious route. This is illustrated by Figure 2-9 which shows that, in relative terms, fossil and renewable resources are not always equally useful starting materials. It is, however, important to note that recent developments in shale gas and oil pricing will also influence this assessment [4, 13, 24]. Although, this does not affect the statement that potential is lying in the shift of the petroleum based molecule for chemicals such as acetaldehyde, butanol or ethyl acetate. The outlook on a growing production and prospects of cheap cellulosic bio-ethanol, combined with growing technological advances could, in this way, result in a strong argument for the production of chemicals from bio-ethanol. Competitive biorefineries, starting from lignocellulosic biomass, will only enhance these prospects towards the production of bio-ethanol, both as fuel as chemical building block as now economic objectives are possible to achieve [5, 15].

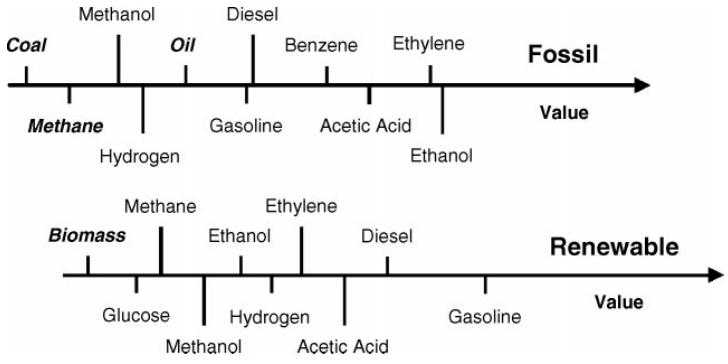

Figure 2-9: Indication of the relative production cost of chemicals produced either via fossil or via renewable resources. The raw materials are shown in italics and the fuels and chemicals are typically produced in one or more process steps, starting from fossil or renewable resources [13]

3 FROM ETHANOL TO ACETALDEHYDE

One of the potential routes for the production of chemicals is the one to acetaldehyde. Because of its high reactivity, acetaldehyde is an important intermediate for the production of acetic acid, ethyl acetate, n-butanol, 1,3-butadiene, pyridines and other chemicals. In the early years, acetaldehyde was mainly produced from ethanol or acetylene. In industrialized countries, ethanol prices were artificially increased via fiscal measures or petrochemical ethanol was simply not available, leading to acetylene as favored starting material. However, in the late 1950s Wacker-Chemie and Hoechst developed the direct oxidation process (Wacker process) using ethylene as feedstock which led to an almost complete replacement of the acetylene processes in the Western countries. Nowadays, the acetylene process is only to be found in Eastern Europe. The route via ethanol was generally applied in countries that lack a chemical industry and fossil resources [26].

During recent years, the use of acetaldehyde as an intermediate was steadily decreasing due to the commissioning of cheaper processes such as the oxo-process for n-butanol and 2-ethylhexanol and the carbonylation of methanol to acetic acid (Monsanto process). Though, the production of pyridine and pyridine bases, which are important raw materials for agricultural chemicals, is expected to increase due to a growing world population. As such, acetaldehyde markets are expected to grow slightly in China, the USA and Western Europe through 2018. Japan on the other hand shows brighter prospects with an expected growth of 4 % in the next five years. The reason for this increase is the volatile supply of butadiene to Japan and the rest of Asia due to limited availability of naphtha [27]. More efficient processes, converting bio-ethanol into green acetaldehyde, could contribute to these increases and cause a shift in feedstock. Comparing both the annual production of bio-ethanol and acetaldehyde, indicates the possibility of completely replacing the petrochemical feedstock by a more renewable alternative as acetaldehyde production is estimated at little more than one million metric tons per year [6, 26].

Table 2-1: Most important producers acetaldehyde in 2004 [26]

Company	Country	Production (10^3 t/y)
Celanese Chemicals Europe GmbH	Germany	120
Eastman Chemical Company	USA	225
ECROS, SA	Spain	90
Japan Aldehyde Company Ltd.	Japan	69
Jilin Chemical Industrial Company	China	180
Kyowa Yuka Company Ltd.	Japan	61
Showa Denko K.K.	Japan	300
Sinopec Yangzi Petrochemical Co.	China	78 (400 planned)
Wacker Chemie AG	Germany	65

3.1 OXIDATION OF ETHANOL

Acetaldehyde can be produced from ethanol via dehydrogenation with or without the presence of oxygen. The former, which is generally known as partial oxidation, is one of the oldest routes in producing acetaldehyde on a laboratory scale:

$$CH_3CH_2OH + \frac{1}{2}O_2 \rightleftarrows CH_3CHO + H_2O \qquad \Delta H = -242.0\ kJ/mol$$

This is commercialized in the Veba Chemie process (Figure 2-10). Ethanol, originating from the production plant, is mixed with air and subsequently sent over a catalyst at temperatures of 500 to 650 °C. The obtained conversions of bio-ethanol are between 50 and 70 %. To recover the generated heat during the partial oxidation of ethanol, a steam recovery system is applied after the reaction zone. The reactor effluent is then further cooled and washed with cold ethanol to remove the exhaust gas. The waste gas generally consists of nitrogen, hydrogen, methane, carbon monoxide and carbon dioxide. It is further used as fuel gas in steam generators. The effluent of the washing column is sent to a fractional distillation column to remove acetaldehyde from ethanol. Ethanol is returned to the reactor after water removal.

The catalyst applied for this process is a silver gauge [28] which reached, at a temperature of 525 °C, conversion levels of 60 % with a selectivity to acetaldehyde of 97 %. The major side product during processing is acetic acid. In the same period, also other catalysts were patented by Eastman and Shell [29, 30]. Due to the severe reaction conditions, along with a high catalyst price, the use of new catalysts has been frequently explored. Most of these new catalytic systems focus on ethanol oxidation and more rarely on ethanol dehydrogenation. This can be contributed to the higher activity that is observed in the presence of oxygen [31].

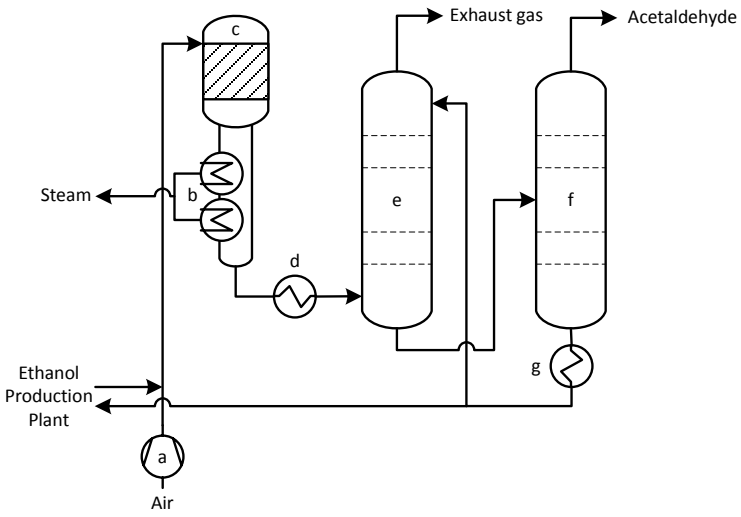

Figure 2-10: Veba Chemie process (a: air compressor; b: heat recovery; c: reactor; d: cooler; e: waste gas scrubber; f: acetaldehyde rectification g: cooler) [26]

Guan et al. investigated the effect of the particle size on the conversion of ethanol to acetaldehyde on a gold catalyst, in the presence and absence of oxygen [31]. The catalyst itself was supported on ordered mesoporous (SBA-15, SBA-16, MCM-41) and conventional silica. The different supports resulted, due to different surface structures, into a different dispersion and consequently different sizes of the gold particles. Figure 2-11 shows the dependence of the activity on this particle size. For the dehydrogenation reaction, a maximum activity is reached at 6 nm while the highest activities for the oxidation are observed at diameters above 10 nm. The reaction towards acetaldehyde occurred faster in the presence of oxygen, regardless of the particle size.

During this study, the best catalyst observed in the presence of oxygen showed a selectivity of 90 % and a conversion of around 20 %, already at 473 K. At these temperatures, no conversion via the dehydrogenation reaction was observed. The dehydrogenation catalysts, however, exhibited a selectivity close to 100 % at temperatures up to 623 K, indicating that partial oxidation will occur at higher rates, though, at a lower selectivity than dehydrogenation. Furthermore, in the oxidation, water is formed as side product while one of the advantages of the reaction at inert atmosphere is the production of hydrogen, a valuable compound in the chemical and petrochemical industry [4, 6].

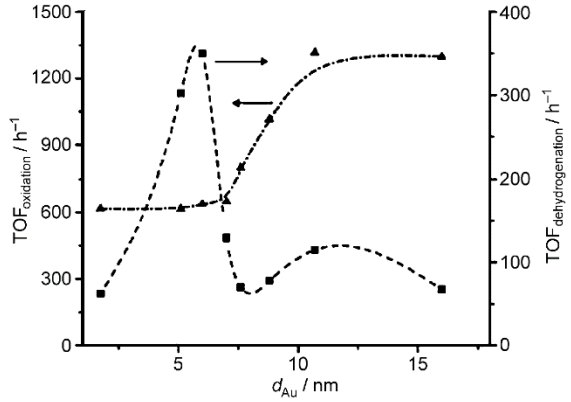

Figure 2-11: Effect of the particle size on TOF for the dehydrogenation and oxidation reaction [31]

3.2 DEHYDROGENATION OF ETHANOL

The second pathway for the production of acetaldehyde from ethanol is via dehydrogenation. In contrast with the partial oxidation, this reaction is endothermic in the absence of oxygen:

$$CH_3CH_2OH \rightleftarrows CH_3CHO + H_2 \qquad \Delta H = +82.5\ kJ/mol$$

The first generations of catalysts were generally based on oxides of copper with or without promotors such as magnesium [32] and chromium [33, 34]. Copper is an active catalyst for the dehydrogenation due to its ability of dehydrogenating the C-O bound while leaving the C-C bound intact [35]. A selectivity of almost 100 % is reached but sufficient regeneration by subsequent oxidation and reduction [36], however, is required due to sintering.

The catalyst life can be prolonged by addition of promotors but these benefits are limited. A thorough investigation in this area was done by Tu et al. who investigated the effect of different

alkali and alkaline earth metal oxides as promotors in the dehydrogenation reaction, shown in Table 2-2 [32, 37]. It was argued that the addition of metal oxides such as MgO, K_2O and Na_2O, introduces weak basic sites and has a promotional effect on the catalyst behavior. For strong basic sites, e.g., SrO, BaO and CaO, this effect has not been observed and they give rise to severe deactivation. Since sodium contains both weak and strong basic sites, a combined effect of both a high activity and fast activation is observed.

Table 2-2: The effect of promotors on the performance of Cu/SiO_2 in the dehydrogenation of ethanol (14 wt% of Cu)

Catalyst	Temperature (K)	Conversion (%)	Selectivity (%)		TOF ($s^{-1}site^{-1}$)	Reference
			Acetaldehyde	Ethyl Acetate		
Cu/SiO_2	573	30	100	-	0.218	[32]
$Cu\text{-}MgO/SiO_2$	573	50 - 55	100	-	0.291	[32]
$Cu\text{-}BaO/SiO_2$	573	10	100	-	0.291	[32]
$NaCu/SiO_2$	573	20 - 25	100	-	0.349	[37]
KCu/SiO_2	573	60	100	-	0.287	[37]

Silica is the support of choice for copper in the dehydrogenation of ethanol [38, 39]. This results from its abundance in nature as well as a superiority in both physical and chemical characteristics to meet specific requirements of applications. Though, research in this area was done to investigate the role of the support and to improve the performance. Alternatively, rice husk ash (RHA) was first adopted by Chang et al. as a support for both nickel and copper catalysts, first in CO_2 hydrogenation and later in ethanol dehydrogenation [40, 41]. Rice husk is a predominant byproduct of domestic agriculture and is composed of extremely amorphous silica. Results indicated that, despite the larger surface area of the conventional silica support, copper impregnated on rice husk ash possesses a better dispersion. Consequently, Cu/RHA showed a higher activity and a slower deactivation rate in the catalytic behavior towards the dehydrogenation of ethanol. Chang et al. attributed the latter to the smaller pores of the commonly used silica gel, suggesting that these are more feasible to be clogged or even sealed during sintering. Rice husk ash, on the contrary, exhibits larger mesopores making it a better support for copper catalysts than conventional SiO_2 [40]. For catalysts prepared via an ion exchange method, a further rise in activity and a negligible decay in performance is observed showing their superiority over the impregnated alternative [41].

Some investigations have been focusing on the effect of the support material on secondary product selectivity [42-45]. In addition to the dehydrogenation of ethanol, dehydrogenative coupling can occur between acetaldehyde and ethanol resulting in the production of ethyl acetate and hydrogen:

$$CH_3CH_2OH + CH_3CHO \rightleftarrows CH_3COOCH_2CH_3 + H_2$$

According to Inui et al., who investigated the performance of $Cu/ZnO\text{-}ZrO_2\text{-}Al_2O_3$ catalysts, this mechanism proceeds via the nucleophilic addition of ethanol to acetaldehyde, creating a hemiacetal which is subsequently dehydrogenated with formation of ethyl acetate. With this catalyst, a high selectivity towards ethyl acetate, combined with a high conversion of ethanol, was obtained [43, 46]. Also other side products are formed during conversion of ethanol on copper catalysts. The selectivity towards these species will generally be dependent of the type of support that is used. An overview of

these selectivity distributions for copper catalysts with different supports was given by Iwasa et al. [42] and is shown in Figure 2-12.

As such, it could be concluded that ZrO_2 and ZnO supports are highly selective for ethyl acetate formation while C_4 species and diethyl ether are produced in appreciable amounts over Al_2O_3. Diethyl ether will be formed from two ethanol molecules via a dehydration reaction on acid sites of the catalyst:

$$2\ CH_3CH_2OH \ \rightleftarrows\ CH_3CH_2OCH_2CH_3 + H_2O$$

According to the authors, the selectivity of the alumina support for the C_4 species, generally consisting of butyraldehyde, methyl ethyl ketone and 1-butanol, dropped after doping with KOH, indicating that these were produced via acid-catalyzed reactions. The formation of diethyl ether was, at this point, completely suppressed. On the MgO support also smaller traces of acetone were observed, though, in a negligible amount.

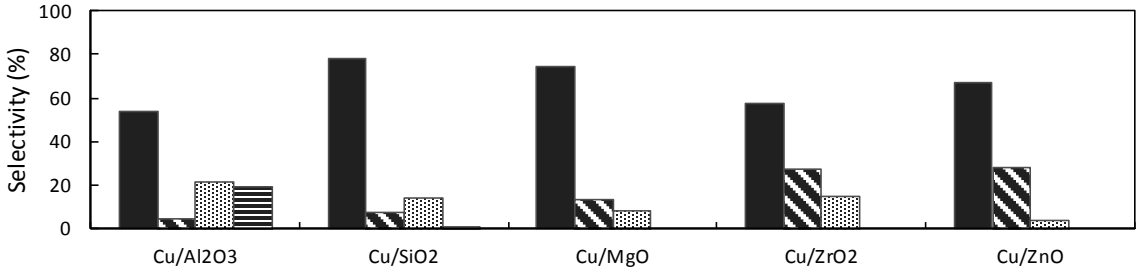

Figure 2-12: Selectivity distribution for different supports (30 wt% Cu) obtained at ethanol conversion of 50 %, a temperature of 493 K and a partial pressure of ethanol of 20.5 kPa (plain: acetaldehyde; obliquely striped: ethyl acetate; dotted: C4-species; horizontally striped: diethyl ether) [42]

Other detailed studies are performed on copper catalysts using ZrO_2 as support material due to its unique properties of having both acid and basic sites on the one hand, and reducing and oxidizing properties on the other hand. ZrO_2 has gained considerable interest in the recent years over other conventional supports such as silica or alumina. As was mentioned previously, weak basic sites could perform a promotional effect, indicating, along with the oxidizing properties, the suitability of zirconia as support in ethanol dehydrogenation. Furthermore, it was reported that ZrO_2 could play a role as a structural promoter as it is described as a preventive element for sintering of Cu crystallites [47].

Sato et al. [48-50] investigated the role of zirconia in the dehydrogenation reaction of ethanol in comparison to silica. It was stated that ethanol is activated to a radical species by Cu^+ sites or by the zirconia surface:

$$CH_3CH_2OH\ + 2^* \rightleftarrows\ CH_3CH_2O^*H + ^*\ \rightleftarrows CH_3CH_2O^* + H^*$$

When this activation takes place on the Cu^+ sites, ethanol can be dehydrogenated and transferred to the Cu^0 sites as an activated species:

$$CH_3CH_2O^* \rightleftarrows CH_3C^*O + 2\,H^* \rightleftarrows CH_3C^*O + H_2$$

On these sites, the activated species will react with an adsorbed hydrogen species resulting in the formation of acetaldehyde:

$$CH_3C^*O + H^* \rightleftarrows CH_3C^*HO + {}^* \rightleftarrows CH_3CHO + 2\,{}^*$$

A second possibility, however, is that the activated species will react with a $CH_3CH_2O^*$ species adsorbed on the Cu^+ and zirconia sites. This side reaction will give rise to formation of ethyl acetate molecules:

$$CH_3C^*O + CH_3CH_2O^* \rightleftarrows CH_3C^*OOCH_2CH_3 + {}^* \rightleftarrows CH_3COOCH_2CH_3 + 2\,{}^*$$

It was argued that when copper is supported on the zirconia surface, in contract to silica supported catalysts, the concentration of Cu^+ sites is rather low. Since these sites are mainly responsible for the dehydrogenation reaction of the adsorbed $CH_3CH_2O^*$, it is more likely that coupling reactions to ethyl acetate are enhanced between the metal and zirconia support. If the support is not active in the reaction, which is the case for silica, the reaction will only take place on the Cu^0/Cu^+ sites on the surface. As dehydrogenation is occurring much faster on these sites, the coupling reaction is less likely to be performed, causing poor ethyl acetate selectivity [4, 48]. A representation of these mechanisms on the different sites at the surface is shown in Figure 2-13.

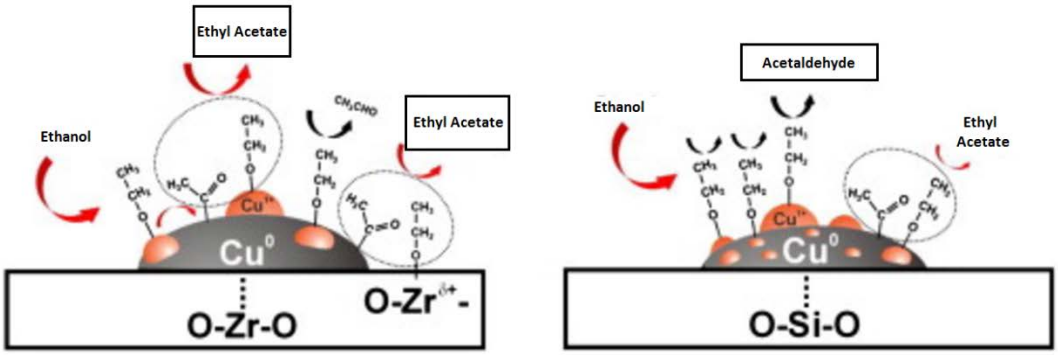

Figure 2-13: The role of zirconia and silica in the dehydrogenation of ethanol [48]

Despite the efforts to obtain higher stabilities for the copper based catalysts, sintering still remains the largest issue for these materials. For this reason, several groups have been exploring alternative catalysts for the dehydrogenation reaction of ethanol, either towards acetaldehyde or ethyl acetate [51-54].

Iwasa et al. studied the effect of the support on the reactivity over supported Pd catalysts [54]. It was concluded that, similar to the copper based catalysts, the support played an important role in the selectivity towards the desired product. Pd/ZnO, Pd/Ga_2O_3 and Pd/In_2O_3 produced acetaldehyde with high selectivity, while other supported Pd catalysts and Pd black showed a high selectivity towards methane and carbon monoxide. It was observed that Pd (110) and (111) surfaces will most probably act as catalysts in the decomposition of ethanol [55, 56]:

$$CH_3CH_2OH \rightleftarrows CH_3COH + H_2 \rightleftarrows CH_4 + CO + H_2$$

Since this reaction is less likely to occur for Pd/ZnO, Pd/Ga_2O_3 and Pd/In_2O_3, the possibility exists that these Pd planes are not present at the surface. Studies on steam reforming and dehydrogenation of methanol [57, 58] showed that the activity and selectivity are markedly enhanced by a reduction step prior to reaction. This was related with the formation of an intermetallic compound, i.e., respectively PdZn, PdGa, PdIn. On the PdZn intermetallic compound, the selectivity towards acetaldehyde was nearly complete, indicating that this could be a viable alternative for the commercially used Cu-catalyst. An overview of the results obtained for different supports of Pd catalysts is represented in Figure 2-14.

These results were re-evaluated by Sánchez et al. who also investigated the effect of SnO_2 as support in the dehydrogenation of ethanol and the role of PdZn and Pd_2Sn_3 intermetallic compounds. Blank tests with only ZnO or SnO_2 showed that the support itself only showed limited conversion and selectivity towards acetaldehyde. Activity tests of PdZn supported on silica, however, showed a conversion of 23.1 % and a selectivity of 95.6 %, confirming the potential of this intermetallic compound. Pd_2Sn_3 supported on silica only showed limited conversion [53]. Contradictory results were obtained by Iwasa et al. who claimed that silica supports cannot be considered ideal as was shown for methanol steam reforming [59]. This support did not enhance the reduction of ZnO, resulting in a limited formation of the PdZn intermetallic compound and such to a limited selectivity towards methanol steam reforming. The main difference with the article of Sánchez et al. was the amount of Pd supported on the catalyst, which was approximately 4 times higher (10 instead of 2.5 wt%). What was further observed by Iwasa et al. is the increase in selectivity that is observed by decreasing the Pd/Zn ratio, resulting in an improved formation of the PdZn intermetallic compound and a reduced presence of metallic Pd.

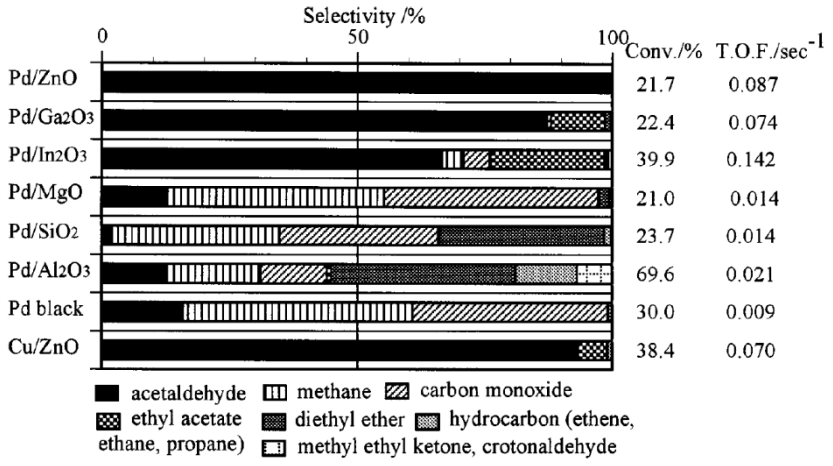

Figure 2-14: Selectivity to carbon-containing products in the dehydrogenation of ethanol at 493 K [54]

4 EXPLORING PDZN INTERMETALLIC COMPOUNDS

In the recent years, academic research institutes have been successfully replacing Cu based catalysts by PdZn intermetallic compounds in a variety of applications, such as methanol steam reforming (MSR) and selective hydrogenation and dehydrogenation reactions. PdZn exhibits similar electronic properties and catalytic reactivity as Cu. The higher stability of PdZn, however, makes it a more attractive alternative because Cu shows a decrease in activity due to sintering. This makes PdZn based catalysts interesting materials for further exploration.

4.1 FORMATION OF THE PDZN INTERMETALLIC COMPOUND

Alloys, but also intermetallic compounds (IMC) have recently gained extra attention as catalysts due to the wide range of desirable and tunable properties they offer. IMCs are, in contrast to the substitutional alloys, single-phase compounds consisting of metals with a partly covalent or ionic bond character. In this way, higher structural stabilities are often observed. Especially segregation, which is a common drawback in the usage of substitutional alloys as catalysts, can be countered as such. In terms of composition, IMCs do not necessarily have to possess a certain stoichiometric composition, but can have a broader stability region [60]. For clarity, only the term intermetallic compound will be used throughout this work to assign the PdZn species.

Pd and Zn are able to form alloys and intermetallic compounds within a wide range of compositions. A representation of the phase diagram of the binary system is shown in Figure 2-15. The thermodynamically stable tetragonal PdZn phase is catalytically the most interesting structure. (Figure 2-16). It is situated in a broad composition range between 37 and 56 % of Zn and has a stoichiometric composition of 1:1. This structure is easily formed by the reduction of Pd particles on a ZnO support at temperatures around 300 °C. In this way, a catalyst is obtained which is already successfully applied in catalytic applications (e.g., MSR) [57, 58, 61].

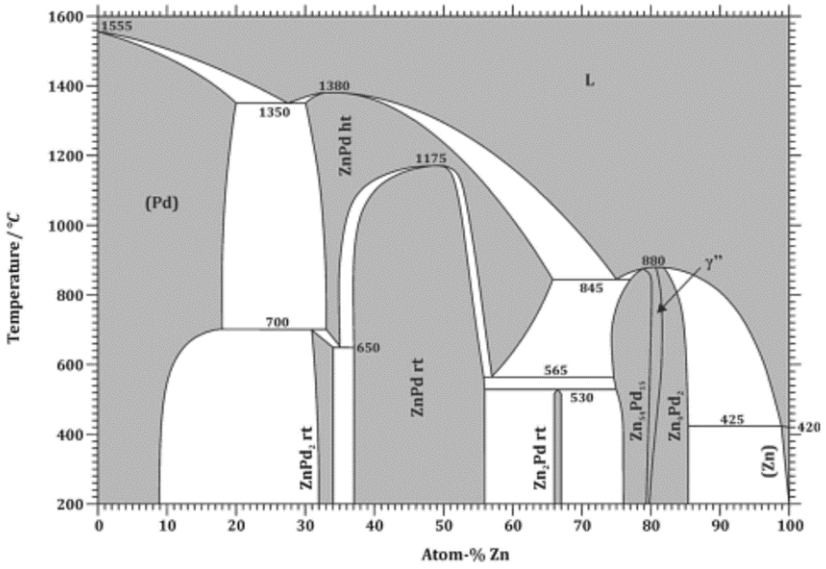

Figure 2-15: Phase diagram of the binary system Pd-Zn [60]

However, preparation of intermetallic PdZn in a controlled manner with a desired composition and particle size is far from straightforward. As a matter of fact, it could be assigned as the major disadvantage of in situ formation of PdZn by reduction starting from Pd/ZnO. In general, the challenge in the synthesis of these intermetallic compounds will be the simultaneous achievement of control of the above mentioned properties and a high surface area. Especially the latter is a very important requirement for application in catalysis.

Electropositive elements or metals with precursors that are not easy to reduce, such as Zn, bring in extra difficulties for controlled incorporation into the IMC. This could not only significantly affect the catalytic properties, but also the IMCs formed. For these reasons, the formation of the PdZn intermetallic compound must be handled with care. In general, PdZn forms under reducing conditions starting from Pd/ZnO at 300 °C. This phenomenon could be explained by hydrogen, activated on the Pd, which migrates towards the ZnO leading to the formation of reduced Zn species. Subsequently, these species diffuse into the Pd forming the intermetallic compound [60].

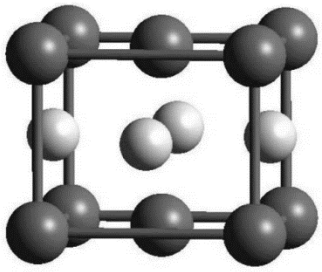

Figure 2-16: Tetragonal structure of the PdZn intermetallic compound (light spheres: Zn, dark spheres: Pd) [62]

These findings were confirmed by Iwasa et al. using ex situ XRD measurements [57]. However, Tew et al. already noticed formation of the intermetallic compound at reduction temperatures of 100 °C using X-ray absorption near edge structure (XANES) [63]. Though, these compounds formed at lower temperatures showed fewer selectivity towards the desired products in catalytic applications, such as MSR, suggesting the simultaneous presence of metallic Pd and PdZn [64]. Summarizing, the exact temperature of the ZnO reduction in presence of metallic Pd could depend on a variety of parameters, e.g., synthesis and reaction conditions.

Overall, Föttinger et al. argued that the formation of the PdZn intermetallic compound starts at the surface and subsequently grows further inwards due to diffusion of reduced Zn particles in the metallic core [65]. The initial formation of the compound already starts at a temperature below 80 °C while diffusion into the actual bulk of the Pd requires temperatures above 350 °C [66, 67]. This has to do with the thermal stability of the surface monolayers of PdZn, creating as such a complete shell around the Pd particles before diffusing into the particle bulk [68].

The support will also play an important role in the synthesis of the intermetallic compound as it could improve the dispersion of the metal particles. This will not only increase the catalytic activity of the IMC but also the stability against sintering as the diffusion distances between active sites increase. Investigations were conducted on the formation of PdZn on oxides such as silica [53, 69] and alumina [70-72]. The latter support resulted in a high dispersion and stability against sintering. However,

residues of ZnO and fcc Pd were still present leading to significant decreases in selectivity [70]. The same effect was, as mentioned previously in 3.2, encountered by Iwasa et al. for silica. This effect was more pronounced at higher loadings of the metals on the support [59].

Though, comparison between different prepared IMCs is reported to be rather difficult due to the sensitivity to the preparation history. As a result, differences in composition, dispersion, homogeneity or metal-support contacts may complicate the comparison. Hydrotalcite-like compounds (HTlc), on the other hand are well-defined platform precursor materials. The advantage of these precursors is the uniform distribution of divalent and trivalent cations in the edge-sharing octahedral, allowing close interaction between all metal cations. This was demonstrated by Ota et al. who applied a Pd(Zn)(Al)O_x precursor which formed the IMC PdZn at temperatures of 250 °C [73]. According to the authors, this occurred via a Pd_2Zn intermediate stage. The usage of hydrotalcite-like compounds as precursors for IMC formation has gained a lot of interest in catalysis applications and has become a widely used support material [74-76].

4.2 THE ROLE OF PDZN IN CATALYSIS

It was mentioned previously that intermetallic compounds offer the advantage of desirable and tunable properties, often different from the ones of individual metals. Substitution of the corresponding metal by an intermetallic compound could as such lead to enhancements in activity, selectivity and especially in stability. Hereby, it is not necessarily the case that the properties of the IMC consists of a superposition of the properties of the metals it is constituting [60].

It was proposed by several authors [62, 77] that an alteration of the electronic structure of Pd by formation of an IMC was responsible for changes in the catalytic performance. As such, the local electronic structure of Pd in PdZn is different from metallic Pd and, in fact, resembles the one of Cu. Due to this similar valence electron density, a catalytic equivalent of Cu based catalysts could be obtained, which did not have the drawbacks encountered for copper such as sintering, already at moderate temperatures, or pyrophoricity [60]. The role of Zn is therefore not solely to alter the electronic structure but also to prevent the Pd from sintering [78]. As a matter of illustration the catalytic performance of PdZn and PtZn was evaluated by Chen et al. [62]. Despite the fact that both catalysts possessed the same crystal structure, catalytic performance of PdZn was significantly better due to the differences in valence band structures.

These findings of similar catalytic performances, combined with an enhanced stability, has led to an increased interest in research areas which generally apply copper based catalysts and encounter a loss in activity due to sintering. The main catalytic applications considered are methanol steam reforming and selective hydrogenation/dehydrogenation reactions.

4.2.1 METHANOL STEAM REFORMING

Methanol has emerged in recent years as a promising carrier for the chemical storage of hydrogen. Since it does not require the cleavage of C – C bonds, it is less prone to coking, in comparison to e.g.,

ethanol as feedstock, and the reaction temperatures are low (200-300 °C). Methanol steam reforming proceeds according to following reaction:

$$CH_3OH + H_2O \rightleftarrows CO_2 + 3\,H_2$$

Mostly, Cu based catalysts have been applied due to their superior performance. Analogies with methanol synthesis can be found in the CO_2 hydrogenation since MSR is the reverse reaction and similar catalysts are active and selective for methanol synthesis [60]. Research on alternative Pd based catalysts was performed by Iwasa et al. who reported that Pd/ZnO showed exceptional selectivity and activity [57, 79, 80]. Several supports and metal catalysts were reviewed. However, Pd/ZnO appeared as one of the most promising candidates for replacing Cu [61, 73]. Also in the case of ethanol steam reforming for hydrogen production, PdZn showed itself as an interesting alternative. Though, the reaction was rather restricted to the dehydrogenation reaction and Pd remains the catalyst of choice for the reforming of ethanol [81].

4.2.2 Selective Hydrogenation Reactions

Pd catalysts are among the most extensively investigated catalysts in hydrogenation reactions for the conversion of organic molecules or CO and CO_2 in methanol synthesis. By using ZnO as support, resulting in the formation of the PdZn intermetallic compound, the reactivity of the Pd in the hydrogenation reactions could be seriously increased. In general, this could be assigned to two different effects: the ligand and ensemble effect.

The first effect results in the modification of the electronic properties of Pd due to the formation of the intermetallic compound, as already mentioned. This is affected by the neighboring Zn atoms which influence as such the strength of adsorption of reactants, products and intermediates. The second effect can be assigned to dilution of the Pd atoms at the surface resulting in a lower concentration of hydrogen at the surface. This latter effect could therefore be of importance in selective hydrogenation reactions [60].

One of the most important applications with a long history of Pd based catalysts is the selective hydrogenation of alkynes to alkenes, with acetylene as most prominent one. Since acetylene acts as a poison for the polymerization catalyst in the production of polyethylene, its removal is required in the ethylene effluent of a steam cracker:

$$C_2H_2 + H_2 \rightleftarrows C_2H_4$$

Pd catalysts show high activity but low selectivity towards this reaction. Besides, deactivation occurs due to coking. By adding a second metal, the performance and selectivity of the catalysts can be enhanced to a large extent. PdZn catalysts were already applied in a similar reaction where 1-pentyne was selectively hydrogenated to 1-pentene with only low formation of alkanes [63]. The lower supply of hydrogen due to the absence of neighboring sites is beneficial for the selectivity by suppressing full hydrogenation. Furthermore, the heat of adsorption of alkenes showed to be lower for PdZn than metallic Pd, leading as such to faster desorption and a higher selectivity [60, 82].

4.2.3 SELECTIVE DEHYDROGENATION REACTIONS

In a much lesser extent than selective hydrogenation reactions of alkynes or dienes, also selective dehydrogenation reactions are performed using PdZn intermetallic compounds. General work in this area was mainly done by Iwasa et al. who claimed the dehydrogenation of methanol to formaldehyde as a side reaction of methanol steam reforming [83]:

$$CH_3OH \rightleftarrows CH_2O + H_2$$

Further extension of this work was done for the dehydrogenation of ethanol for different intermetallic compounds with Pd [54]:

$$CH_3CH_2OH \rightleftarrows CH_3COH + H_2$$

As such, it could be argued that PdZn showed a nearly complete selectivity to acetaldehyde and one of the higher turnover frequencies of the different catalysts as was shown in Figure 2-14. It is for these potential prospects that PdZn intermetallic compounds will be investigated more thorough in this work.

5 HYDROTALCITE PRECURSORS IN CATALYSIS

Comparative studies of different metallic phases often suffer from limited comparability due to differences encountered during preparation history. Application of various solvents, ligands, supports or thermal post-treatments result in different structures, dispersion, etc. making catalytic comparison in terms of intrinsic effects rather difficult. For these reasons, a synthetic approach must be applied that allows conserving the complexity of the supported catalysts and that assures a straightforward comparison between different intermetallic compounds. This synthetic approach can be addressed by application of hydrotalcite-like compounds prepared by a precipitation method. As these materials are known to be well-defined platform precursors for intermetallic compounds, reproducibility is high, assuring adequate comparability.

5.1 LAMELLAR STRUCTURE OF HYDROTALCITE

Hydrotalcite-like compounds are anionic clay materials which are, unlike their counterparts, the cationic clays, only rarely found in nature. The group of anionic clays have attracted much attention worldwide because of their potential in a wide range of applications such as catalysis in pharmaceutical industries and organic synthesis, anion scavengers in waste water treatment, medicines, etc. [84]. Another name for the hydrotalcite-like compounds is layered double hydroxides (LDHs) which gives a better indication of the structure of the material.

Expression (2-1) shows the structure of the representative of the LDHs, i.e., hydrotalcite. This structure is closely related to the one of brucite or $Mg(OH)_2$. The divalent and trivalent cations (Mg and Al, respectively) are uniformly distributed in edge-sharing octahedrons. Each of the octahedrons will consist of one Mg^{II} ion in the centre and six OH^- groups at vertexes similar to brucite. In the case

of hydrotalcite, though, some of the magnesium ions are replaced by Al^{III} resulting in a positive charge that requires compensation by carbonate anions, located in the interlayer region between two brucite-like layers. Next to the anions, the gallery will also contain water molecules which are hydrogen bounded to the layered hydroxides and/or interlayered anions. The electrostatic interactions and hydrogen bonds between the layers and the contents of the gallery will hold the layers together and form the crystal structure of the hydrotalcite [73, 84, 85]. A representation of the layered structure of the hydrotalcite is shown in Figure 2-17.

$$[Mg_3Al(OH)_8][(CO_3)\tfrac{1}{2}2H_2O] \quad (2\text{-}1)$$

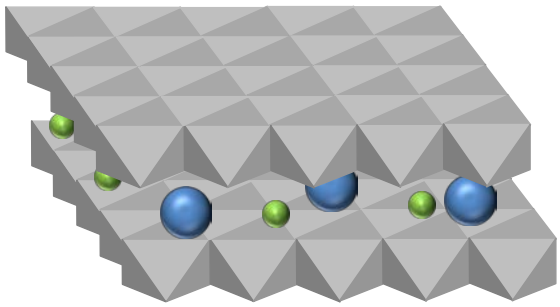

Figure 2-17: Layered structure of hydrotalcite

All LDH materials have a structure similar to hydrotalcite as shown in Figure 2-17, even though the structure can sometimes be distorted due to various combinations of cations or intercalated anions with different sizes or charge. Nonetheless, the majority of the LDH materials adhere to following general formula:

$$[M^{II}_{1-x}M^{III}_x(OH)_2]^{x+}(A^{n-})_{x/n}mH_2O \quad (2\text{-}2)$$

In which M^{II} and M^{III} represent the divalent and trivalent metal, respectively. A^{n-} represents the anion while the value of x is reported to be 0.2 to 0.33 in forming a pure LDH phase. A too high concentration of trivalent cations could cause destabilization of the structure due to repulsion forces resulting from the higher charge of the brucite-like layers. Lower concentrations of trivalent cations at their turn cause a lower concentration of anions in between the layers for compensation of the charge. Due to this lower concentration, the structure will tend to distort. Though, it is possible to synthesize HTlc with x values outside its desired range. Due to formation of hydroxides and other impurities it will, however, be more difficult to obtain a consistent concentration within the layers.

During formation of the LDH, the divalent and trivalent metal will substitute, fully or partially, Mg and Al, respectively. The only requirement for these ions to substitute is an ionic radius which is not that different from those of Mg^{II} and Al^{III} in order to maintain the octahedron configuration. An overview of some examples of metals for substitution is shown in Table 2-3, indicating that a large variety in compositions is possible to be obtained. Ion exchange is hereby not solely limited to one metal, but different combinations are possible, as well as higher valences, e.g., Sn^{IV} or Zr^{IV}. It will, however, not be possible to substitute magnesium by cations with radii smaller than 0.06 nm, e.g., Bi^{II}, as they will destabilize the structure of the LDH [85, 86].

The restraints on the choice of interlayer anions are much less pronounced as a large variety can be applied in synthesis. The only conditions are that the anion should not abstract metal ions from the brucite-like layers and that it has a sufficiently high charge density. Large anion molecules with low charges will undeniably result in a lack of compensation of the positive charge of the head layers, causing distortion of the material. Both inorganic and organic anions are yet applied in the synthesis of hydrotalcite-like compounds, some of the most prominent examples are CO_3^{2-}, NO_3^-, Cl^-, carboxylates, terephthalates, etc.

Table 2-3: Ionic radii of some cations with a coordinate number of 6, suitable for substitution in the LDH structure [84]

M^{II}	Radius (nm)	M^{III}	Radius (nm)
Fe	0.061	Al	0.054
Co	0.065	Co	0.055
Ni	0.069	Fe	0.055
Mg	0.072	Mn	0.058
Cu	0.073	Ga	0.062
Zn	0.074	Cr	0.069
Pd	0.086	V	0.074

5.2 CALCINATION AND MEMORY EFFECT

The LDH material can be directly transformed into the corresponding mixed oxide by calcination at higher temperatures (> 400 °C). In this way, materials are formed with interesting catalytic properties such as high thermal stability, large surface areas and high basicity. During the transformation towards the corresponding mixed oxides, one can distinguish between four different stages [84]. In a first stage, dehydration takes place in order to remove the intercalated water molecules out of the galleries between the brucite-like layers:

$$[M^{II}_{1-x}M^{III}_x(OH)_2]^{x+}(A^{n-})_{x/n}mH_2O \rightarrow [M^{II}_{1-x}M^{III}_x(OH)_2]^{x+}(A^{n-})_{x/n} + m\,H_2O \quad (2\text{-}3)$$

Specifically for hydrotalcite, dehydration will perform at temperatures between 100 and 250 °C. This is followed at higher temperatures (350-450 °C) by dehydroxylation to transform the hydroxide layer into oxides. This step is mainly responsible for the collapse of the structure and the disappearance of the lamellar arrangement:

$$[M^{II}_{1-x}M^{III}_x(OH)_2]^{x+}(A^{n-})_{x/n} \rightarrow [M^{II}_{1-x}M^{III}_xO]^{x+}(A^{n-})_{x/n} + H_2O \quad (2\text{-}4)$$

In a sequencing step, decomposition of the anion in the structure will occur, giving rise to the actual mixed oxide structure with the decomposed anions:

$$[M^{II}_{1-x}M^{III}_xO]^{x+}(A^{n-})_{x/n} \rightarrow M^{II}_{1-x}M^{III}_xO_{1+x/2}(BO_y) \quad (2\text{-}5)$$

In which BO_y corresponds with the decomposed anions. In configuration with NO_3^- or CO_3^{2-} as intercalated anions, which is the case for hydrotalcite, the decomposed anion is not present as these will be removed as NO_2 and CO_2, respectively. Elimination of the carbonate ions as CO_2 could partially destroy the layers, giving rise to holes or so-called craters. This cratering can be assigned to be

responsible for the detected increase in pore volume and corresponding surface area, observed by calcination of the hydrotalcite. This decarbonation of the structure generally takes place between 420 and 470 °C [87].

Further heating of the mixed oxide structure, will introduce additional decomposition of the structure by oxide reformation:

$$M^{II}_{1-x}M^{III}_{x}O_{1+x/2}(BO_y) \rightarrow (1-3/2\,x)\,M^{II}O + x/2\,M^{II}M^{III}_{2}O_4 + BO_y \quad (2\text{-}6)$$

For hydrotalcite, this phase segregation generally occurs at temperatures higher than 700 °C, giving rise to the corresponding MgO and $MgAl_2O_4$ spinel structures. From this stage on, the structure of the material can be considered irreversible which is not the case for previous stages. For the former structures an interesting effect will occur as the original layered material will be restored upon exposure to an aqueous solution. This is known as the so-called memory effect and is illustrated in Figure 2-18.

In the aqueous solution, the hydroxide structure is again restored from the oxides and anions can intercalate into the lamellar structure of the LDH. The dehydroxylation of the brucite-like layer, i.e., the collapse of the layered structure occurs topotactically at temperatures less than 500 °C [88]. Diffusion of metal ions, resulting in occupation of other metal sites, at this stage of calcination could therefore be ignored. This indicates that cations in the LDH structure remain evenly distributed at the oxide structure and thus the same structure could be restored after reconstruction [84]. This property of mixed oxides could therefore be considered a benefit since the presence of water in processing will not result in a destruction of the catalyst as the structure can be restored by regeneration at higher temperatures.

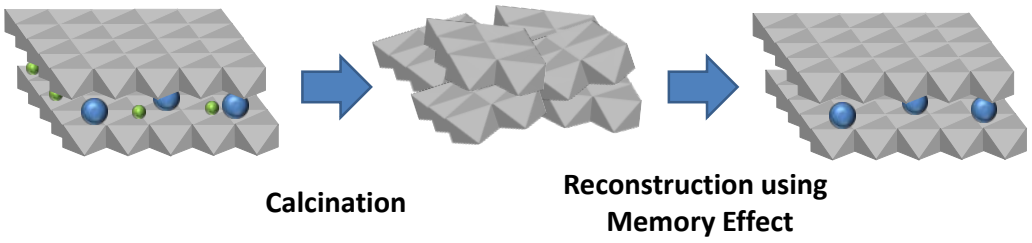

Figure 2-18: Calcination and reconstruction of the hydrotalcite structure

5.3 CATALYSIS

Upon calcination of LDHs, mixed oxides are obtained with attractive properties from a catalytic point of view, such as high surface areas, thermal stability and a considerable basicity. The ability of cation exchange, in order to introduce other metals into the structure, further expands the areas of catalysis in which application can be found. During the last decades, intensive research was performed using calcined hydrotalcite-like compounds covering the regions of base and redox catalysis [89]. In order to give a brief overview, only the application of dehydrogenation will be

discussed. Due to the high metal dispersion that is possible to be obtained, hydrotalcite precursors are gaining interest as support for metals active in dehydrogenation reactions.

In patent literature, examples can be found on the dehydrogenation of aliphatic hydrocarbons (C_6 - C_{20}) into aromatics using Pd/Mg(Al)O_x at temperatures of 620-770 K and pressures of 0-1 MPa. Both selectivity and conversion were reported to be higher in comparison to conventional Pd based catalysts [90].

$$C_6H_{12} \xrightarrow{Pd/Mg(Al)O_x} C_6H_6 + 3\,H_2$$

Also smaller hydrocarbons are considered for dehydrogenation with hydrotalcite-based catalysts as alternative pathways for conventional steam cracking are searched for. Research in this area was performed by the group of Alexis Bell which applied a PtGa intermetallic compound in the dehydrogenation of small alkanes such as ethane [91, 92]:

$$C_2H_6 \xrightarrow{PtGa/Mg(Ga)(Al)O_x} C_2H_4 + H_2$$

It was reported that both metals would migrate towards each other upon reduction, resulting as such in the corresponding intermetallic compound. Furthermore, the effect of other intermetallic compounds, such as PtSn and PtIn, was investigated [93, 94]. The extension towards propane dehydrogenation was more thoroughly explored by Redekop et al. [76] at Ghent University.

HTlc are also applied as supports for vanadium in the oxidative dehydrogenation of butane:

$$C_4H_{10} + O_2 \xrightarrow{V/Mg(Al)O_x} C_4H_8 + H_2O + \frac{1}{2}O_2 \xrightarrow{V/Mg(Al)O_x} C_4H_6 + 2\,H_2O$$

It was argued that the basic properties of the support favoured the consecutive dehydrogenation reactions towards butadiene resulting in a high selectivity towards dehydrogenation. Due to the absence of strong acid sites on the support, decomposition into carbon dioxides is inhibited. Conversion, however, was low as V only reduced at very high temperatures [95].

In terms of alcohol dehydrogenation, benzyl alcohol was successfully dehydrogenated in batch by Fang et al. [96] to benzaldehyde at nearly complete selectivity:

$$C_6H_6CH_2OH \xrightarrow{Au/Mg(Al)O_x} C_6H_6COH + H_2$$

Hydrotalcite derived precursors were not yet deployed on the dehydrogenation of ethanol to acetaldehyde. Ota et al, however, applied PdZn catalysts on an oxide support for the steam reforming of methanol which shows, as according to Iwasa et al, similarities with the dehydrogenation reaction (see 3.2). As the formation of the PdZn intermetallic compound was successfully obtained on hydrotalcite precursors, it should be possible to extrapolate its use towards the dehydrogenation of ethanol.

6 CONCLUSIONS

Increasing energy demands and growing concerns regarding climate change have been a major driving force towards the exploration of alternative, green, resources for the production of both energy and chemicals. The introduction of biorefineries, in which simultaneous production of fuels, chemicals and energy will be performed, is therefore considered an interesting option to compete with today's petrochemical refineries.

From all molecules produced from biomass, ethanol has proven to possess the highest potential as it is not solely valuable as fuel, but also as platform molecule to a variety of chemicals. Especially, the production of oxygenated compounds can be considered more viable since fossil resources typically lack oxygen contain building blocks. One of the potential routes is the production of acetaldehyde which is, due to its high reactivity, an important intermediate for the production of ethyl acetate, n-butanol or pyridines. Production from bio-ethanol can be performed via two different pathways: partial oxidation and dehydrogenation. This study focusses on the latter as simultaneous production of hydrogen takes place.

Conventional catalysts used for the dehydrogenation of ethanol are Cu based. However, these show the drawback of rapid sintering, resulting in the need for sufficient regeneration. In the search for an alternative, PdZn intermetallic compounds are introduced. Pd based catalysts lack in selectivity and give rise to severe decomposition of the ethanol molecules towards carbon monoxide and methane. The addition of Zn, though, will alter the electronic structure towards the one of copper, increasing as such the selectivity. Furthermore, it will prevent the Pd from sintering and ameliorate the stability of the catalyst.

Hydrotalcite precursors offer a suitable support for these intermetallic compounds as it is possible to evenly distribute the metals throughout the structure. Such, reproducibility is high and the formation of the intermetallic compound upon reduction is favored. The support itself offers the benefits of a high surface area, increasing as such the dispersion, and thermal stability. Due to its ability of exchanging cations, a wide variety of compositions can be attained.

To date, no reviews are available on the performance of PdZn intermetallic compounds via hydrotalcite precursors in the dehydrogenation of ethanol. However, the application of such catalysts was already successful in the steam reforming of methanol, a reaction with an analogous catalysis. Further focus of this work is therefore lying within this area of catalysis.

7 REFERENCES

[1] The Outlook for Energy: a View to 2040, Exxon Mobil, 2014.
[2] National Renewable Energy Laboratory (NREL).
[3] J.J. Bozell, G.R. Petersen, Technology development for the production of biobased products from biorefinery carbohydrates-the US Department of Energy's "Top 10" revisited, Green Chem, 12 (2010) 539-554.
[4] J.M.R. Gallo, J.M.C. Bueno, U. Schuchardt, Catalytic Transformations of Ethanol for Biorefineries, J Brazil Chem Soc, 25 (2014) 2229-2243.
[5] J.A. Posada, A.D. Patel, A. Roes, K. Blok, A.P.C. Faaij, M.K. Patel, Potential of bioethanol as a chemical building block for biorefineries: Preliminary sustainability assessment of 12 bioethanol-based products, Bioresource Technol, 135 (2013) 490-499.
[6] C. Angelici, B.M. Weckhuysen, P.C.A. Bruijnincx, Chemocatalytic Conversion of Ethanol into Butadiene and Other Bulk Chemicals, ChemSusChem, 6 (2013) 1595-1614.
[7] B. Kamm, P.R. Gruber, M. Kamm, Biorefineries - Industrial Processes and Products, Ullmann's Encyclopedia for Industrial Chemistry, Wiley-VCH Verlag GmbH & Co. KGaA, 2012.
[8] International Energy Statistics, U.S. Energy Information Administration (EIA).
[9] Global ethanol production.
[10] J. Baeyens, Q. Kang, L. Appels, R. Dewil, Y.Q. Lv, T.W. Tan, Challenges and opportunities in improving the production of bio-ethanol, Prog Energ Combust, 47 (2015) 60-88.
[11] M.J. Bradshaw, Global energy dilemmas: a geographical perspective, Geogr J, 176 (2010) 275-290.
[12] O.J. Sanchez, C.A. Cardona, Trends in biotechnological production of fuel ethanol from different feedstocks, Bioresource Technol, 99 (2008) 5270-5295.
[13] J. Rass-Hansen, H. Falsig, B. Jørgensen, C.H. Christensen, Bioethanol: fuel or feedstock?, J Chem Technol Biot, 82 (2007) 329-333.
[14] R. Hammerschlag, Ethanol's energy return on investment: A survey of the literature 1990 - Present, Environ Sci Technol, 40 (2006) 1744-1750.
[15] J. Sun, Y. Wang, Recent Advances in Catalytic Conversion of Ethanol to Chemicals, Acs Catal, 4 (2014) 1078-1090.
[16] M.J. Groom, E.M. Gray, P.A. Townsend, Biofuels and biodiversity: Principles for creating better policies for biofuel production, Conserv Biol, 22 (2008) 602-609.
[17] S. Kumar, R. Gupta, G. Kumar, D. Sahoo, R.C. Kuhad, Bioethanol production from Gracilaria verrucosa, a red alga, in a biorefinery approach, Bioresource Technol, 135 (2013) 150-156.
[18] H.J. Huang, S. Ramaswamy, U.W. Tschirner, B.V. Ramarao, A review of separation technologies in current and future biorefineries, Sep Purif Technol, 62 (2008) 1-21.
[19] L.M. Vane, Separation technologies for the recovery and dehydration of alcohols from fermentation broths, Biofuel Bioprod Bior, 2 (2008) 553-588.
[20] A.K. Frolkova, V.M. Raeva, Bioethanol dehydration: State of the art, Theor Found Chem En+, 44 (2010) 545-556.
[21] A.A. Kiss, D.J.P.C. Suszwalak, Enhanced bioethanol dehydration by extractive and azeotropic distillation in dividing-wall columns, Sep Purif Technol, 86 (2012) 70-78.
[22] L.M. Vane, A review of pervaporation for product recovery from biomass fermentation processes, J Chem Technol Biot, 80 (2005) 603-629.
[23] European Plastics Demand.
[24] P.N.R. Vennestrom, C.M. Osmundsen, C.H. Christensen, E. Taarning, Beyond Petrochemicals: The Renewable Chemicals Industry, Angew Chem Int Edit, 50 (2011) 10502-10509.
[25] I'm Green Polyethylene.
[26] M. Eckert, G. Fleischmann, R. Jira, H.M. Bolt, K. Golka, Acetaldehyde, Ullmann's Encyclopedia of Industrial Chemistry, (2006).
[27] Acetaldehyde, Chemical Economics Handbook, Stanford Research Institute2013.

[28] W. Heitmann, W. Ester, Verfahren zur Herstellung von Carbonylverbindungen, Veba Chemie West GmbH, Germany, 1970.
[29] E.H. Carter, L.E. Sartain, Conversion of organic hydroxy compounds to carbonyl derivatives, Eastman Kodak Co, United States, 1954.
[30] W. Brackman, Process for the preparation of aldehydes and ketones, Shell Dev, 1959.
[31] Y.J. Guan, E.J.M. Hensen, Ethanol dehydrogenation by gold catalysts: The effect of the gold particle size and the presence of oxygen, Appl Catal a-Gen, 361 (2009) 49-56.
[32] Y.J. Tu, Y.W. Chen, Effects of alkaline-Earth oxide additives on silica-supported copper catalysts in ethanol dehydrogenation, Ind Eng Chem Res, 37 (1998) 2618-2622.
[33] W. Opitz, W. Urbanski, Verfahrung zur Herstellung von Aldehyden durch Dehydrierung von primären aliphatischen Alkoholen, Knapsack AG, Germany, 1961.
[34] Y.J. Tu, C.P. Li, Y.W. Chen, Effect of Chromium Promoter on Copper-Catalysts in Ethanol Dehydrogenation, J Chem Technol Biot, 59 (1994) 141-147.
[35] P. Chladek, E. Croiset, W. Epling, R.R. Hudgins, Characterization of copper foam as catalytic material in ethanol dehydrogenation, Can J Chem Eng, 85 (2007) 917-924.
[36] A.J. Marchi, J.L.G. Fierro, J. Santamaria, A. Monzon, Dehydrogenation of isopropylic alcohol on a Cu/SiO2 catalyst: A study of the activity evolution and reactivation of the catalyst, Appl Catal a-Gen, 142 (1996) 375-386.
[37] Y.J. Tu, Y.W. Chen, Effects of alkali metal oxide additives on Cu/SiO2 catalyst in the dehydrogenation of ethanol, Ind Eng Chem Res, 40 (2001) 5889-5893.
[38] F.W. Chang, W.Y. Kuo, H.C. Yang, Preparation of Cr2O3-promoted copper catalysts on rice husk ash by incipient wetness impregnation, Appl Catal a-Gen, 288 (2005) 53-61.
[39] I. Chorkendorff, J.W. Niemantsverdriet, Concepts of modern catalysis and kinetics, John Wiley & Sons2006.
[40] F.W. Chang, W.Y. Kuo, K.C. Lee, Dehydrogenation of ethanol over copper catalysts on rice husk ash prepared by incipient wetness impregnation, Appl Catal a-Gen, 246 (2003) 253-264.
[41] F.W. Chang, H.C. Yang, L.S. Roselin, W.Y. Kuo, Ethanol dehydrogenation over copper catalysts on rice husk ash prepared by ion exchange, Appl Catal a-Gen, 304 (2006) 30-39.
[42] N. Iwasa, N. Takezawa, Reforming of Ethanol - Dehydrogenation to Ethyl-Acetate and Steam Reforming to Acetic-Acid over Copper-Based Catalysts, B Chem Soc Jpn, 64 (1991) 2619-2623.
[43] K. Inui, T. Kurabayashi, S. Sato, Direct synthesis of ethyl acetate from ethanol over Cu-Zn-Zr-Al-O catalyst, Appl Catal a-Gen, 237 (2002) 53-61.
[44] K. Inui, T. Kurabayashi, S. Sato, N. Ichikawa, Effective formation of ethyl acetate from ethanol over Cu-Zn-Zr-Al-O catalyst, J Mol Catal a-Chem, 216 (2004) 147-156.
[45] L.X. Wang, W.C. Zhu, D.F. Zheng, X. Yu, J. Cui, M.J. Jia, W.X. Zhang, Z.L. Wang, Direct transformation of ethanol to ethyl acetate on Cu/ZrO2 catalyst, React Kinet Mech Cat, 101 (2010) 365-375.
[46] K. Inui, T. Kurabayashi, S. Sato, Direct synthesis of ethyl acetate from ethanol carried out under pressure, Journal of Catalysis, 212 (2002) 207-215.
[47] J. Agrell, H. Birgersson, M. Boutonnet, I. Melian-Cabrera, R.M. Navarro, J.L.G. Fierro, Production of hydrogen from methanol over Cu/ZnO catalysts promoted by ZrO2 and Al2O3, Journal of Catalysis, 219 (2003) 389-403.
[48] A.G. Sato, D.P. Volanti, I.C. de Freitas, E. Longo, J.M.C. Bueno, Site-selective ethanol conversion over supported copper catalysts, Catal Commun, 26 (2012) 122-126.
[49] A.G. Sato, D.P. Volanti, D.M. Meira, S. Damyanova, E. Longo, J.M.C. Bueno, Effect of the ZrO2 phase on the structure and behavior of supported Cu catalysts for ethanol conversion, Journal of Catalysis, 307 (2013) 1-17.
[50] I.C. Freitas, S. Damyanova, D.C. Oliveira, C.M.P. Marques, J.M.C. Bueno, Effect of Cu content on the surface and catalytic properties of Cu/ZrO2 catalyst for ethanol dehydrogenation, J Mol Catal a-Chem, 381 (2014) 26-37.

[51] A.B. Gaspar, F.G. Barbosa, S. Letichevsky, L.G. Appel, The one-pot ethyl acetate syntheses: The role of the support in the oxidative and the dehydrogenative routes, Appl Catal a-Gen, 380 (2010) 113-117.
[52] A.B. Gaspar, A.M.L. Esteves, F.M.T. Mendes, F.G. Barbosa, L.G. Appel, Chemicals from ethanol-The ethyl acetate one-pot synthesis, Appl Catal a-Gen, 363 (2009) 109-114.
[53] A.B. Sanchez, N. Homs, J.L.G. Fierro, P.R. de la Piscina, New supported Pd catalysts for the direct transformation of ethanol to ethyl acetate under medium pressure conditions, Catalysis Today, 107-08 (2005) 431-435.
[54] N. Iwasa, O. Yamamoto, R. Tamura, M. Nishikubo, N. Takezawa, Difference in the reactivity of acetaldehyde intermediates in the dehydrogenation of ethanol over supported Pd catalysts, Catal Lett, 62 (1999) 179-184.
[55] J.L. Davis, M.A. Barteau, Decarbonylation and Decomposition Pathways of Alcohols on Pd(111), Surf Sci, 187 (1987) 387-406.
[56] R. Shekhar, M.A. Barteau, Structure Sensitivity of Alcohol Reactions on (110) and (111) Palladium Surfaces, Catal Lett, 31 (1995) 221-237.
[57] N. Iwasa, S. Masuda, N. Ogawa, N. Takezawa, Steam Reforming of Methanol over Pd/Zno - Effect of the Formation of Pdzn Alloys Upon the Reaction, Appl Catal a-Gen, 125 (1995) 145-157.
[58] N. Takezawa, N. Iwasa, Steam reforming and dehydrogenation of methanol: Difference in the catalytic functions of copper and group VIII metals, Catalysis Today, 36 (1997) 45-56.
[59] N. Iwasa, T. Mayanagi, W. Nomura, M. Arai, N. Takezawa, Effect of Zn addition to supported Pd catalysts in the steam reforming of methanol, Appl Catal a-Gen, 248 (2003) 153-160.
[60] K. Föttinger, PdZn based catalysts: connecting electronic and geometric structure with catalytic performance, in: J.J. Spivey, Y.-F. Han, K.M. Dooley (Eds.) Catalysis, The Royal Society of Chemistry2013.
[61] N. Iwasa, T. Mayanagi, N. Ogawa, K. Sakata, N. Takezawa, New catalytic functions of Pd-Zn, Pd-Ga, Pd-In, Pt-Zn, Pt-Ga and Pt-In alloys in the conversions of methanol, Catal Lett, 54 (1998) 119-123.
[62] Z.X. Chen, K.M. Neyman, A.B. Gordienko, N. Rosch, Surface structure and stability of PdZn and PtZn alloys: Density-functional slab model studies, Phys Rev B, 68 (2003).
[63] M.W. Tew, H. Emerich, J.A. van Bokhoven, Formation and Characterization of PdZn Alloy: A Very Selective Catalyst for Alkyne Semihydrogenation, J Phys Chem C, 115 (2011) 8457-8465.
[64] Y.H. Chin, R. Dagle, J.L. Hu, A.C. Dohnalkova, Y. Wang, Steam reforming of methanol over highly active Pd/ZnO catalyst, Catalysis Today, 77 (2002) 79-88.
[65] K. Fottinger, J.A. van Bokhoven, M. Nachtegaal, G. Rupprechter, Dynamic Structure of a Working Methanol Steam Reforming Catalyst: In Situ Quick-EXAFS on Pd/ZnO Nanoparticles, J Phys Chem Lett, 2 (2011) 428-433.
[66] A. Bayer, K. Flechtner, R. Denecke, H.P. Steinruck, K.M. Neyman, N. Rosch, Electronic properties of thin Zn layers on Pd(111) during growth and alloying, Surf Sci, 600 (2006) 78-94.
[67] W. Stadlmayr, S. Penner, B. Klotzer, N. Memmel, Growth, thermal stability and structure of ultrathin Zn-layers on Pd(111), Surf Sci, 603 (2009) 251-255.
[68] C. Rameshan, W. Stadlmayr, C. Weilach, S. Penner, H. Lorenz, M. Havecker, R. Blume, T. Rocha, D. Teschner, A. Knop-Gericke, R. Schlogl, N. Memmel, D. Zemlyanov, G. Rupprechter, B. Klotzer, Subsurface-Controlled CO2 Selectivity of PdZn Near-Surface Alloys in H-2 Generation by Methanol Steam Reforming, Angew Chem Int Edit, 49 (2010) 3224-3227.
[69] B.E. Green, C.S. Sass, L.T. Germinario, P.S. Wehner, B.L. Gustafson, Ester Hydrogenation over Pd-Zn Sio2, Journal of Catalysis, 140 (1993) 406-417.
[70] T. Conant, A.M. Karim, V. Lebarbier, Y. Wang, F. Girgsdies, R. Schlogl, A. Datye, Stability of bimetallic Pd-Zn catalysts for the steam reforming of methanol, Journal of Catalysis, 257 (2008) 64-70.
[71] L. Bollmann, J.L. Ratts, A.M. Joshi, W.D. Williams, J. Pazmino, Y.V. Joshi, J.T. Miller, A.J. Kropf, W.N. Delgass, F.H. Ribeiro, Effect of Zn addition on the water-gas shift reaction over supported palladium catalysts, Journal of Catalysis, 257 (2008) 43-54.

[72] A. Karim, T. Conant, A. Datye, The role of PdZn alloy formation and particle size on the selectivity for steam reforming of methanol, Journal of Catalysis, 243 (2006) 420-427.
[73] A. Ota, E.L. Kunkes, I. Kasatkin, E. Groppo, D. Ferri, B. Poceiro, R.M.N. Yerga, M. Behrens, Comparative study of hydrotalcite-derived supported Pd2Ga and PdZn intermetallic nanoparticles as methanol synthesis and methanol steam reforming catalysts, Journal of Catalysis, 293 (2012) 27-38.
[74] A. Ota, J. Krohnert, G. Weinberg, I. Kasatkin, E.L. Kunkes, D. Ferri, F. Girgsdies, N. Hamilton, M. Armbruster, R. Schlogl, M. Behrens, Dynamic Surface Processes of Nanostructured Pd2Ga Catalysts Derived from Hydrotalcite-Like Precursors, Acs Catal, 4 (2014) 2048-2059.
[75] M. Filez, E.A. Redekop, H. Poelman, V.V. Galvita, R.K. Ramachandran, J. Dendooven, C. Detavernier, G.B. Marin, Unravelling the Formation of Pt-Ga Alloyed Nanoparticles on Calcined Ga-Modified Hydrotalcites by in Situ XAS, Chem Mater, 26 (2014) 5936-5949.
[76] E.A. Redekop, V.V. Galvita, H. Poelman, V. Bliznuk, C. Detavernier, G.B. Marin, Delivering a Modifying Element to Metal Nanoparticles via Support: Pt-Ga Alloying during the Reduction of Pt/Mg(Al,Ga)O-x Catalysts and Its Effects on Propane Dehydrogenation, Acs Catal, 4 (2014) 1812-1824.
[77] A.P. Tsai, S. Kameoka, Y. Ishii, PdZn=Cu: Can an intermetallic compound replace an element?, J Phys Soc Jpn, 73 (2004) 3270-3273.
[78] S.C. Shekar, J.K. Murthy, P.K. Rao, K.S.R. Rao, E. Kemnitz, Selective hydrogenolysis of dichlorodifluoromethane(CCl2F2) over CCA supported palladium bimetallic catalysts, Appl Catal a-Gen, 244 (2003) 39-48.
[79] N. Iwasa, T. Mayanagi, S. Masuda, N. Takezawa, Steam reforming of methanol over Pd-Zn catalysts, React Kinet Catal L, 69 (2000) 355-360.
[80] N. Iwasa, M. Yoshikawa, W. Nomura, M. Arai, Transformation of methanol in the presence of steam and oxygen over ZnO-supported transition metal catalysts under stream reforming conditions, Appl Catal a-Gen, 292 (2005) 215-222.
[81] A. Casanovas, J. Llorca, N. Homs, J.L.G. Fierro, P.R. de la Piscina, Ethanol reforming processes over ZnO-supported palladium catalysts: Effect of alloy formation, J Mol Catal a-Chem, 250 (2006) 44-49.
[82] M. Crespo-Quesada, F. Cardenas-Lizana, A.L. Dessimoz, L. Kiwi-Minsker, Modern Trends in Catalyst and Process Design for Alkyne Hydrogenations, Acs Catal, 2 (2012) 1773-1786.
[83] N. Iwasa, S. Kudo, H. Takahashi, S. Masuda, N. Takezawa, Highly Selective Supported Pd Catalysts for Steam Reforming of Methanol, Catal Lett, 19 (1993) 211-216.
[84] Z.P. Xu, J. Zhang, M.O. Adebajo, H. Zhang, C.H. Zhou, Catalytic applications of layered double hydroxides and derivatives, Appl Clay Sci, 53 (2011) 139-150.
[85] F. Cavani, F. Trifiro, A. Vaccari, Hydrotalcite-Type Anionic Clays: Preparation, Properties and Applications, Catalysis Today, 11 (1991) 173-301.
[86] X. Duan, D.G. Evans, Layered double hydroxides, Springer Science & Business Media2006.
[87] F. Rey, V. Fornes, J.M. Rojo, Thermal-Decomposition of Hydrotalcites - an Infrared and Nuclear-Magnetic-Resonance Spectroscopic Study, J Chem Soc Faraday T, 88 (1992) 2233-2238.
[88] V. Rives, Surface Texture and Electron Microscopy Studies of Layered Double Hydroxides, Layered Double Hydroxides: Present and Future, Nova Science Publishers, Inc. 2006.
[89] B.F. Sels, D.E. De Vos, P.A. Jacobs, Hydrotalcite-like anionic clays in catalytic organic reactions, Catal Rev, 43 (2001) 443-488.
[90] N.J. Blom, E.G. Derouane, Process and catalyst for preparing aromatic compounds, Topsoe Haldor AS, 1992.
[91] P.P. Sun, G. Siddiqi, M.F. Chi, A.T. Bell, Synthesis and characterization of a new catalyst Pt/Mg(Ga)(Al)O for alkane dehydrogenation, Journal of Catalysis, 274 (2010) 192-199.
[92] G. Siddiqi, P.P. Sun, V. Galvita, A.T. Bell, Catalyst performance of novel Pt/Mg(Ga)(Al)O catalysts for alkane dehydrogenation, Journal of Catalysis, 274 (2010) 200-206.
[93] P.P. Sun, G. Siddiqi, W.C. Vining, M.F. Chi, A.T. Bell, Novel Pt/Mg(In)(Al)O catalysts for ethane and propane dehydrogenation, Journal of Catalysis, 282 (2011) 165-174.

[94] V. Galvita, G. Siddiqi, P.P. Sun, A.T. Bell, Ethane dehydrogenation on Pt/Mg(Al)O and PtSn/Mg(Al)O catalysts, Journal of Catalysis, 271 (2010) 209-219.
[95] T. Blasco, J.M.L. Nieto, A. Dejoz, M.I. Vazquez, Influence of the acid-base character of supported vanadium catalysts on their catalytic properties for the oxidative dehydrogenation of n-butane, Journal of Catalysis, 157 (1995) 271-282.
[96] W.H. Fang, J.S. Chen, Q.H. Zhang, W.P. Deng, Y. Wang, Hydrotalcite-Supported Gold Catalyst for the Oxidant-Free Dehydrogenation of Benzyl Alcohol: Studies on Support and Gold Size Effects, Chem-Eur J, 17 (2011) 1247-1256.

Chapter 3: Procedures

1 INTRODUCTION

In this chapter an overview will be provided of the different procedures that were applied during this work on the synthesis and characterization of the catalysts. Furthermore, the reader is guided through the reaction set-up used for the catalytic reaction experiments. Attention is hereby devoted to the different sections in the flow sheet and the measurement of kinetic data.

2 CATALYST SYNTHESIS AND OPERATION

2.1 NOMENCLATURE

Since PdZn intermetallic compounds are prepared via two different synthesis routes, it is important to stress their difference in nomenclature. In general a mixed oxide with a brucite-like structure and different metals (besides magnesium) incorporated in the structure is defined as Mg(Me)O_x. As an intermetallic compound is formed, this is introduced in the front of the designation. In case of impregnation of the metals, these are also introduced before the designation, though, in their oxide notation. Such, the different catalysts are referred to as:

- Pd and Zn incorporated in the structure: Mg(Al)(Pd)(Zn)O_x
- Pd and Zn impregnated in the structure: PdO,ZnO/Mg(Al)O_x
- Pd and Zn incorporated in the structure and reduced: PdZn/Mg(Al)(Pd)(Zn)O_x
- Pd and Zn impregnated in the structure and reduced: PdZn/Mg(Al)O_x

2.2 SYNTHESIS

Two different synthesis pathways are applied to prepare PdZn intermetallic compounds on hydrotalcite precursors. In a first approach the Pd and Zn metals will be grafted on the catalyst structure by means of impregnation. The second approach will already include these metals inside the structure via a one-pot synthesis, so called coprecipitation.

2.2.1 COPRECIPITATION

One of the most conventional methods, especially for the preparation of hydrotalcite precursors, is coprecipitation due to its reliability and reproducibility of the synthesis. For these reasons, the method is seen as recommendable for scaling up in order to produce larger quantities of material [1]. Therefore, coprecipitation is the method of choice during this work for the preparation of hydrotalcite precursors. The synthesis methods of these precursors will be as according to the ones applied by Ota et al. [2] and the group of Alexis Bell [3-6].

To start the synthesis of this material, two different solutions are prepared: a metal nitrate solution, containing the corresponding metals, and a basic solution of hydroxyl and carbonate ions. The latter is used to create conditions of supersaturation by control of the pH of the solution. In general, it is required to reach a pH higher or equal to the one at which the most soluble hydroxide is

precipitated. This happens in practice by dropwise addition of both solutions in an aqueous environment at a fixed temperature of 323 K under constant stirring. The pH is maintained at a value around 10. The compositions of both solutions for the preparation of 20 g of Mg(Al)(Pd)(Zn)O_x are listed in Table 3-1. These quantities correspond with atomic ratios for Mg/Al/Pd/Zn of 100/10-3x/x/2x, in which x corresponds with a quantity of 1 wt% of Pd in the catalyst. The corresponding masses in the basic solution for the synthesis were as reported by Sun et al. [3]. This synthesis method will be referred to as the one-pot synthesis.

Table 3-1: Composition of both solutions in the one-pot synthesis of 20 g of Mg(Al)(Pd)(Zn)O_x

Solution 1		**Solution 2**	
Compound	**Mass (g)**	**Compound**	**Mass (g)**
$Mg(NO_3)_2.6H_2O$	116.41	Na_2CO_3	2.40
$Al(NO_3)_3.9H_2O$	14.77	NaOH	22.60
$Pd(NO_3)_2.2H_2O$	0.501		
$Zn(NO_3)_2.6H_2O$	1.118		

After addition of both solutions, the corresponding precipitate is aged for 24 hours at room temperature. Subsequently, the precipitate is filtered and washed until a neutral pH. During washing, an important consideration is to completely remove the nitrate ions still present in the material as these are able to substitute the carbonate ions in the interlayer structure. Since these ions are more thermally stable, it will be more difficult to remove them upon calcination [7].

After filtration, the hydrotalcite-like compound is dried overnight and consequently calcined ex-situ to obtain the corresponding mixed oxide. This calcination will take place at 873 K for 2 hours after a temperature ramp of 4 hours. Afterwards, the catalyst is shaped into pellets of 250 to 500 µm by subsequent compressing, crushing and sieving.

Since the metals Pd and Zn are incorporated into the mixed oxide structure, these synthesized catalysts will be further denoted throughout this work as incorporated ones.

2.2.2 IMPREGNATION

An alternative way of grafting PdZn intermetallic compounds on a mixed oxide basis is via impregnation. The mixed oxide containing solely Mg and Al is first prepared in a simultaneous way as the incorporated catalyst. The composition of both solutions used in the one-pot synthesis to obtain 20 grams of catalyst is listed in Table 3-2. Subsequently, two solutions of respectively Pd and Zn nitrates, dissolved in ethanol, are added to the support under constant stirring. After addition, the material is dried and pulverized before it is calcined at identical conditions as in previous section. Pelletizing will also be performed via a similar procedure. Since the main difference of this synthesis is the addition of Pd and Zn via impregnation, the corresponding catalysts are further indicated as impregnated ones.

Table 3-2: Composition of both solutions in the one-pot synthesis of 20 g of Mg(Al)O_x

Solution 1		Solution 2		Solutions 3 and 4 (ethanol)	
Compound	**Mass (g)**	**Compound**	**Mass (g)**	**Compound**	**Mass (g)**
$Mg(NO_3)_2.6H_2O$	116.410	Na_2CO_3	2.40	$Pd(NO_3)_2.2H_2O$	0.501
$Al(NO_3)_3.9H_2O$	16.881	NaOH	22.60	$Zn(NO_3)_2.6H_2O$	1.118

2.2.3 Pretreatment and Regeneration

In order to create the PdZn intermetallic compound, subsequent reduction is required. This will be performed on-line after loading the catalyst in the reaction set-up (section 3) by sequencing redox cycles: $(H_2\text{-}O_2)_n\text{-}H_2$. Each of these cycles takes 30 minutes and will consist of a flow of the corresponding gas at 0.620 or 0.612 mmol s^{-1} for hydrogen and oxygen, respectively. In between every cycle, nitrogen is fed at the same flow rate of hydrogen as buffer for 15 minutes. The number of cycles n will have a certain influence on the particle size of the catalyst and hence on the activity. This will be discussed in later chapters. An overview of the formation of PdZn intermetallic compounds via different synthesis methods, followed by reduction, is shown in Figure 3-1.

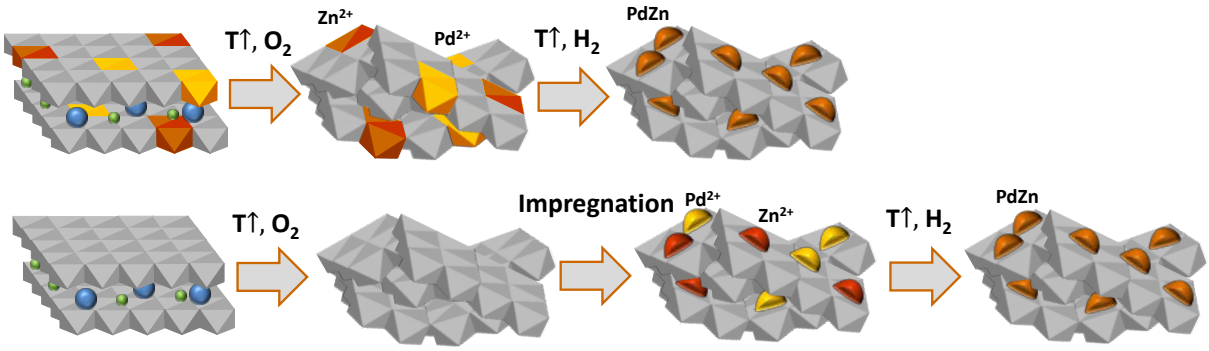

Figure 3-1: Different procedures of active site generation via incorporation (upper) and impregnation (lower), followed by reduction [3-6]

2.3 Characterization Techniques

2.3.1 BET Analysis

The underlying principle of surface area measurements via a BET analysis is to physisorb an inert gas, such as nitrogen in order to determine how many molecules one requires to form a complete monolayer. Although this sounds straightforward, molecules, in practice, adsorb beyond the monolayer, forming multilayers. In addition, the size of the nitrogen molecules allows them to condense in the small pores of the catalyst material. As the ease of condensation is largely depending on the pores, this phenomenon, called capillary pore condensation, can be utilized to determine the type of pores and their size distribution [8]. To observe this condensation, the operating temperature is set at 77 K or the boiling point of liquid nitrogen.

In order to account for multilayer adsorption, an isotherm was developed by Brunauer, Emmet and Teller, represented by equation (3-1) [9]. As this method has its limitations, one must note that the equation is solely valid under following assumptions [8]:

- Dynamic equilibrium between adsorbate and adsorptive: the rates of adsorption and desorption in any layer are equal
- Molecules adsorb on equivalent adsorption sites (first layer)
- The molecules of the first layer constitute the adsorption sites for molecules in the second layer, and so on for higher layers
- Interactions between adsorbates are ignored
- Adsorption-desorption conditions are the same for all layers but the first
- The adsorption energy for molecules in the second and higher layers equals the condensation energy
- The multilayer grows to infinite thickness at the saturation pressure ($p = p_0$)

$$\frac{V_a}{V_0} = \frac{\chi \frac{p}{p_0}}{\left(1 - \frac{p}{p_0}\right)\left(1 - \frac{p}{p_0} + \chi \frac{p}{p_0}\right)} \tag{3-1}$$

With V_a Adsorbed volume [m³]
V_0 Adsorbed volume at solely monolayer adsorption [m³]
p Pressure [Pa]
p_0 Vapor pressure of the adsorbed component [Pa]
χ Ratio of the desorption rate coefficients of the first and second layer, measure for the activation energy bearing in mind condensation: $cst \exp[-\frac{E_d - \Delta_{cond}H}{RT}]$
E_d Activation energy for desorption [J mol^{-1}]
$\Delta_{cond}H$ Condensation enthalpy [J mol^{-1}]
T Temperature [K]
R Gas constant [8.314 J mol^{-1} K^{-1}]

The determination of the internal surface area will take place in the relative pressure range between 0.05 and 0.35 as regression is only accurate in this area. The calculation is performed via the linearized equation of expression (3-1):

$$\frac{p}{p_0 - p}\frac{1}{V_a} = \frac{1}{\chi V_0} + \frac{(\chi - 1)}{\chi V_0}\frac{p}{p_0} = \alpha + \eta \frac{p}{p_0} \tag{3-2}$$

Regression will subsequently result in values for the constants α and η, which will be applied for the determination of the volume in case of monolayer adsorption. Following expression will then be used to determine the internal surface area from this adsorbed monolayer:

$$a_s = \frac{V_0 N_A}{22400 \frac{mol}{m^3}} \frac{a_m}{W} \tag{3-3}$$

With a_s Internal surface area [m² kg_{cat}]
N_A Avogadro number [6.022 10^{23} mol^{-1}]

a_m Surface area taken by one adsorbed molecule, i.e., 0.162 nm² for N_2
W Catalyst weight [kg_{cat}]

The isotherm of mesoporous materials will contain a hysteresis that will correspond with capillary condensation occurring inside the catalyst pores. As the form of the hysteresis will largely depend on the ease of condensation and consequently the pore size, the average pore size could be determined via the Barrett-Joyner-Halenda (BJH) method [10]. All measurements were performed on a Tristar II from Micromeritics®.

2.3.2 TPR/TPO

Temperature programmed reaction methods, such as reduction (TPR) or oxidation (TPO), are analysis techniques in which the corresponding reaction is monitored while the temperature increases linearly in time. This is monitored by measuring the outlet composition via a mass spectrometer as this will represent the corresponding gas consumption. Thus, for TPR and TPO this will respectively be hydrogen and oxygen. By applying the TPR analysis method to the catalyst, information can be acquired about the temperature necessary to reach a complete reduction of both palladium and zinc and thus if the formation of the intermetallic compound could occur in some way. TPO on the other hand, can be applied to investigate whether cokes are formed on the catalyst surface or not by detection of CO or CO_2 signals during the measurement. Furthermore, a combination of both methods can be used to simulate a number of oxidation-reduction cycles. Subsequent characterization by means of TEM could than indicate the desired amount of cycles necessary to regenerate the catalyst. The amount of reduction cycles could indeed affect the particle size and hence the number of active sites of the catalyst, signifying the need for characterization to assign an adequate number of cycles. The TPO and TPR procedures were applied to an apparatus of the Autochem II series from Micromeritics®.

2.3.3 XRD

The crystallographic structure of the catalyst materials will be characterized by X-ray diffraction (XRD) analysis. XRD occurs in the elastic scattering of X-ray photons by atoms in a periodic lattice. The scattered monochromatic X-rays that are in phase will then give constructive interference, satisfying the Bragg relation [8]:

$$m\Lambda = 2d\ sin\Theta \tag{3-4}$$

With m Order of reflection [-]
Λ Wave length of the incident radiation [m]
d Distance between two crystallographic planes [m]
Θ Angle of incidence [-]

By changing the angle of incidence at a constant wave length, XRD could hence provide information on the different crystallographic planes present and the corresponding lattice spacing. In addition, one can consider that the shape of the diffraction peaks will carry information on the dimensions of the reflective planes. Diffraction lines of perfect crystals are very narrow while smaller crystallite

sizes (below 100 nm) will give rise to line broadening due to destructive interference. This relation of the crystal size with the width of the diffraction peak can be characterized by the Sherrer equation:

$$< L > = \frac{K\lambda}{\beta cos\theta} \tag{3-5}$$

With <L> Dimension of the particle in the direction perpendicular to the reflecting plane [m]
β Half width of signal [-]
K Shape factor, often taken as 1 [-]

A disadvantage of XRD, however, is that it cannot detect particles that are either too small or amorphous [8]. Therefore, TEM will be considered to achieve a more accurate determination of the particle size. The XRD spectra will be measured using a Bruker-AXD D8 Discover which emits a Cu Kα radiation with a wavelength of 0.154 nm.

2.3.4 TEM

In transmission electron microscopy (TEM), a primary electron beam of high energy and intensity is passed through a condenser to form parallel rays that impinge on the sample. The attenuation of the beam will hereby depend on both the density and thickness of the material, resulting in a two-dimensional projection of the sample mass by the transmitted electrons. This is subsequently magnified by electron optics to produce a bright field image. The corresponding dark field image is obtained from the diffracted electron beams [8]. A representation of the TEM set-up is shown in Figure 3-2. In contrast to scanning electron microscopy (SEM), TEM will only provide information in a two-dimensional form, however, on a subnanometer scale. It can therefore be considered as a very accurate method for determination of the catalyst particle sizes, providing that there is sufficient contrast between catalyst and support.

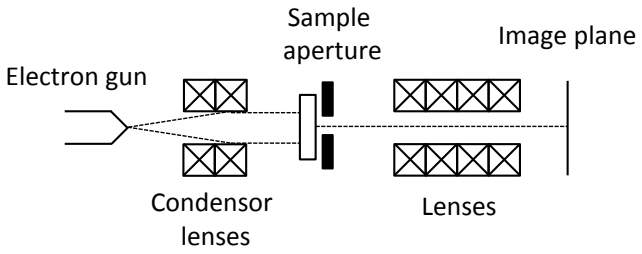

Figure 3-2: Set-up of an electron microscope in the transmission mode [8]

By means of the bright and dark field images of the TEM experiments, particle size distributions will be analyzed. The number of particles analyzed will hereby set at a value of 500 which is subsequently characterized by a normal distribution represented in following expression:

$$F(d_{PdZn}) = x \exp\left[-\frac{(d_{PdZn} - y)^2}{2z^2}\right] \tag{3-6}$$

With F Frequency of the corresponding particle diameter [-]

d_{PdZn} Particle diameter of PdZn [m]
x Constant generally in the order of magnitude of the highest frequency [-]
y Constant representing the average particle diameter [m]
z Constant representing the standard deviation on the particle diameter [m]

The particle size distribution obtained via TEM experiments could, in this manner, give an indication of the dispersion of the catalyst, i.e., an indication for the number of metal atoms accessible for reaction over the total number of metal atoms, represented by following equation [8]:

$$D = \frac{PdZn_s}{PdZn_t} \tag{3-7}$$

With D Dispersion of the catalyst [-]
$PdZn_s$ Number of PdZn atoms at the surface of the catalyst [-]
$PdZn_t$ Number of PdZn atoms in the catalyst [-]

The dispersion of the catalyst can subsequently be determined via following expression [11]:

$$D = \frac{2\ MM_{PdZn}\ \sigma}{\rho_{PdZn}\ N_A\ d_{PdZn}} \tag{3-8}$$

With MM_{PdZn} Molecular weight of the PdZn intermetallic compound [kg mol^{-1}]
σ Surface density of PdZn molecules [m^{-2}]
ρ_{PdZn} Density of the PdZn intermetallic compound [kg m^{-3}]

The factor 2 represents the fact that a Pd atom provides two active sites for dissociative hydrogen adsorption. The surface density of PdZn molecules are calculated based on diameter values provided by Chen et al. [12] and stating that only Pd atoms are available for chemisorption. The density of the PdZn intermetallic compound is based on the density of equimolar amounts of both metals. That way, expression (3-8) could be rewritten as:

$$D = \frac{1.2}{d_{PdZn}} \tag{3-9}$$

In literature, a value of 1.1 was reported for similar calculations of PdZn dispersion [2]. The number of active sites of PdZn on the surface is consequently calculated via expression (3-7) taking into account the number of PdZn atoms in the catalyst. For the synthesized catalysts, containing 1 wt% of Pd, this will be 0.0940 mol per kg of catalyst.

3 REACTION SET-UP AND OPERATION

The experimental study on reaction kinetics in this work is performed on a High Throughput Kinetics Mechanistic Investigation set-up (further indicated as HTK-MI) which is commercially distributed by Zeton B.V. In general, the set-up consists of four reactor blocks, each containing two tubular reactors. A representation of the set-up is shown in Figure 3-3, indicating the presence of a section for both gaseous and liquid feedstock, a reactor section and an analysis section. The analysis section consists of two gas chromatographs (GC), not shown on the figure, consisting of 1 column and an FID detector and one microGC with 4 columns and 4 TCD detectors, i.e., commercially sold as a 3000 µGC. A

complete overview of the four sections is illustrated by the P&ID of HTK-MI, represented by Figure 3-4. In what follows, more elaboration will be provided on the different sections. A summary of the different features and possible operating conditions of the HTK-MI set-up was provided by Van der Borght et al. [13] and is shown in Table 3-4.

Table 3-3: Features and operating conditions of the High-Throughput Kinetics Mechanistic Investigation [13]

Feature or operating condition	**HTK-MI**
Number of reactors	8
Number of heating blocks	4
Reactor type	Tubular
Reactor internal diameter d_{id} (10^{-3} m)	11.0
Reactor length L (m)	0.9
Feed flow rate control	Per reactor
Operating temperature range T_{min}, T_{max} (K)	323 - 923
Operating pressure range p_{min}, p_{max} (10^5 Pa)	1 - 200
Catalyst mass W (10^{-3} kg)	0.5 - 10

Figure 3-3: High Throughput Kinetics Mechanistic Investigation with liquid feed section (a), gaseous feed section (b), reactor section (c) and analysis section (d)

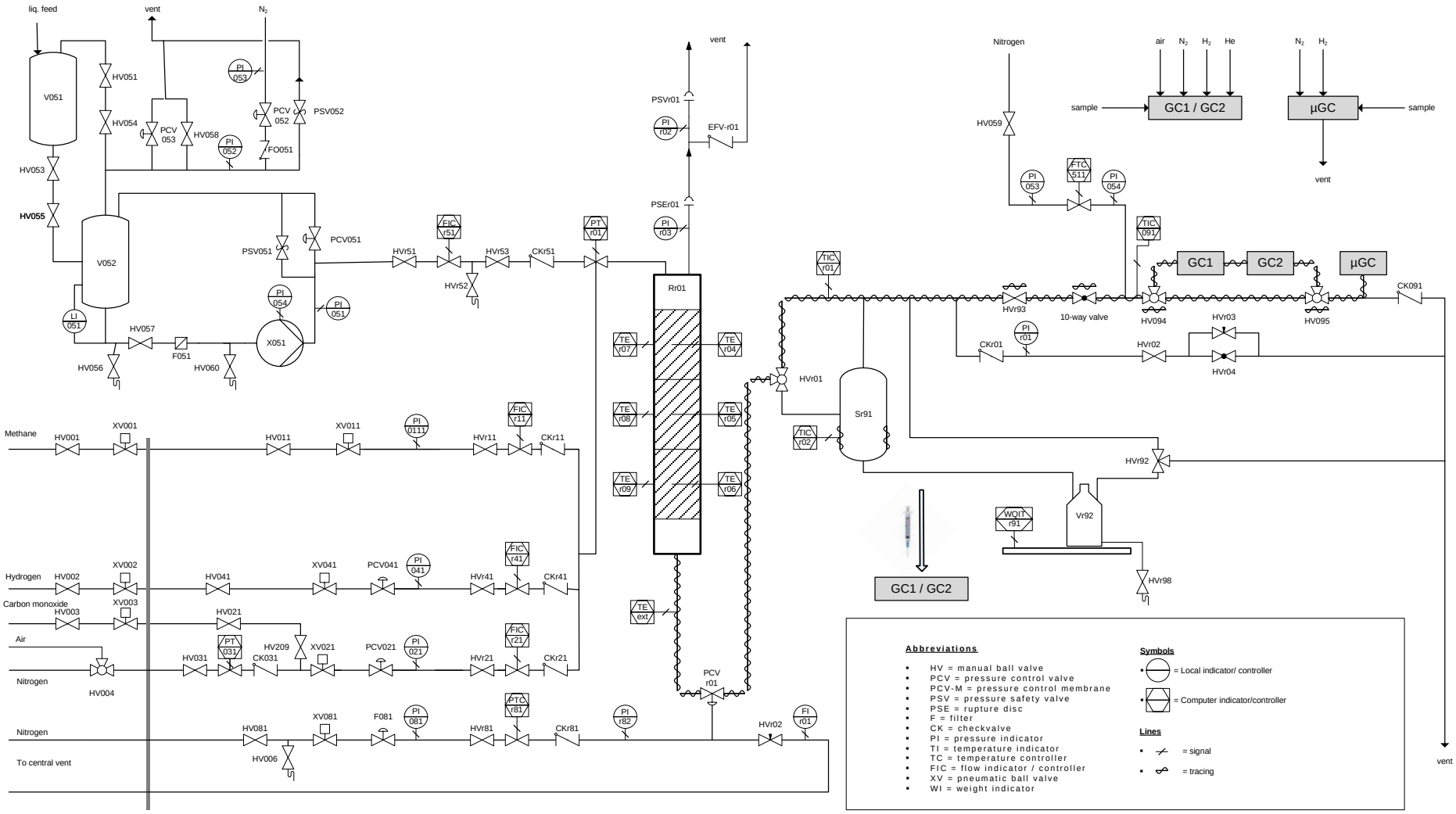

Figure 3-4: P&ID diagram of the HTK-MI set-up

3.1 GASEOUS FEED SECTION

The feed section of the reaction set-up can be divided into a gaseous and liquid section. The former section consists of mass flow controllers (MFCs) of the type EL-FLOW® from Bronkhorst High-Tech B.V. Three different flow controllers are present:

- MFC 1: methane, calibrated at 10 Nl/h
- MFC 2: nitrogen/oxygen, calibrated for nitrogen at 100 Nl/h
- MFC 4: hydrogen, calibrated for hydrogen at 1000 Nl/h

The second type of flow controller is connected on two gas supplies, between which is interchanged during the regeneration procedure. It is necessary to bear in mind the fact that these controllers are only calibrated for the specified type of gas and therefore a correction factor needs to be taken into account in case of other gases. This correction factor will be determined based on the thermal conductivity of the actual component and the one used for calibration of the controllers. Oxygen flow will hereby be controlled by the same controller as nitrogen (MFC 2), indicating the need for a correction factor. For the thermal mass flow controllers applied during the experiments, the correction factor will hence be calculated based on the difference in heat capacity and density of both fluids:

$$CF_{O_2} = \frac{c_{p,O_2}\rho_{O_2}}{c_{p,N_2}\rho_{N_2}} \tag{3-10}$$

With c_p Heat capacity at a constant pressure [J kg^{-1} K^{-1}]
ρ Normal density at 273.15 K and 101.325 kPa [kg m^{-3}]

The correction factor calculated for oxygen will have a value of 1.013 which needs to be multiplied with the desired set point to obtain the necessary set point of the flow controller.

The first controller, which is generally used for methane flow, is not used during operation. Methane is a commonly applied internal standard during analysis on the HTK-MI set-up. Though, during ethanol dehydrogenation methane can be formed as byproduct through decomposition of ethanol and is thus not suited as internal standard. For this reason, n-hexane is used which is added via the liquid feed section.

3.2 LIQUID FEED SECTION

As experimental feedstock, ethanol or mixtures of water and ethanol are used in the HTK-MI. Since these components are in the liquid state at room temperature, a liquid feed section is required for an efficient supply of the feedstock. Therefore, a reciprocating pump (Eldex Optos series) is used to transport the liquid feed through a riser pipe towards the reactor. In the upstream section of the reactor, the liquid is subsequently mixed with nitrogen coming from the gaseous feed section which should lead to evaporation of the liquid feed. This was confirmed by simulations performed with Aspen Plus®, shown in Figure 3-6. The gas mixture is then fed to the reactor section. Together with ethanol and water, a third component in the liquid feed is n-hexane. This is used as internal standard

throughout the reaction as neither formation, nor consumption will occur. Experimental data will hereby be limited to measurements with maximal deviations of 5 % based on a carbon balance.

3.3 REACTOR SECTION

The reactor section consists of two parallel tubes positioned in a heated reactor block. Temperature control can be performed both externally, i.e., wall temperature, as internally, i.e., center of tube, via thermocouples. As the temperature is measured at three points along the axial coordinate, a corresponding temperature profile can be measured and hence be controlled more thorough, an important consideration for isothermal operation of the reactor (Chapter 5: Intrinsic Kinetics).

As will be discussed in the chapter on intrinsic kinetics, a second important consideration for isothermicity is the presence of an inert compound to reduce the generated heat per unit of volume during operation. The materials that are used for this dilution are α-alumina pellets. An artist impression of the reactor content is shown in Figure 3-5. Three different layers will be present, distinguished by their diameter.

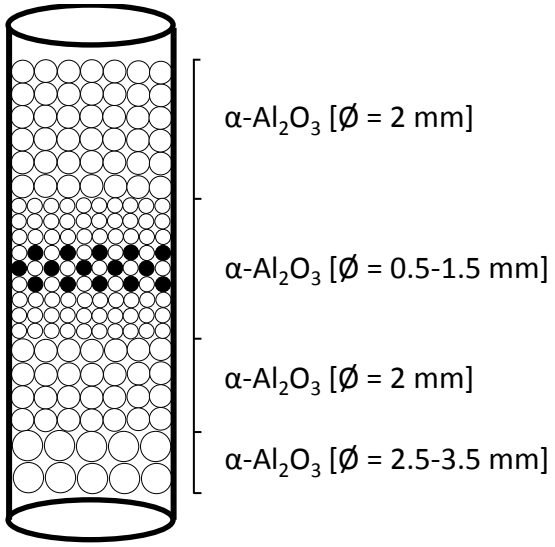

Figure 3-5: Reactor loading with catalyst (black) and inert (white) material

Downstream of the reactor section, the products are sent to a flash vessel for the removal of liquid products formed due to condensation by the decrease in temperature and pressure. This indicates that it is necessary to consider if condensation occurs with reactants or products. If a liquid phase would be present, this needs to be analyzed separately, making use of an online sampler. To assure a full operation in gas phase, simulations are performed with the Aspen Plus® software [14]. A representation of the set-up is illustrated in Figure 3-6, showing the reactor and the subsequent cooling and pressure relief. The feed will comprise of 95.26 mol% of nitrogen and 4.76 mol% of ethanol. After reaction, the effluent is cooled down to 60 °C and relieved to 1 atm. Taking into account a sensitivity analysis on the conversion in the reactor, it was observed that condensation was avoided in all situations and all effluent was flowing to the analysis section downstream of the vessel.

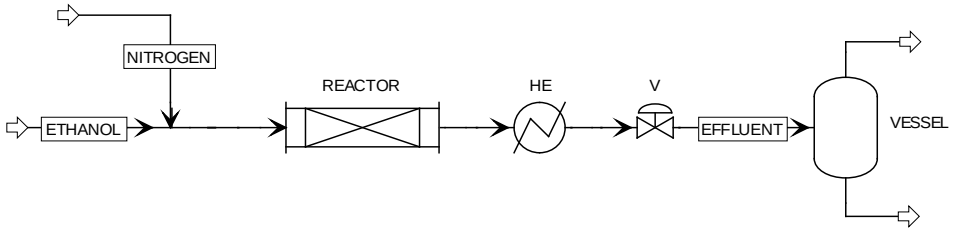

Figure 3-6: HTK-MI set-up in Aspen software (HE: heat exchanger; V: valve)

3.4 ANALYSIS SECTION

Before flowing to the gas analysis section, a multiport selection valve needs to be passed by, which connects the different reaction sections for analysis. 10 gates will be present, one for each reactor, one for calibration purposes and one outlet towards the analysis section. In a first part of this section of the reaction set-up two gas chromatographs (Agilent Technologies 6850 series) equipped with a flame ionization detector (FID) are present for analysis. The operating principle of such a detector is to ionize the components by sending them through a H_2 flame. The ions which are subsequently formed are then transported between two electrodes resulting in a current proportional to the concentration of the component. Due to the ionization, this analysis method is not suitable for every component. Nitrogen and carbon monoxide are for instance not possible to be measured. The GCs are suited for both general and PONA (Paraffins, Olefins, Naphthenes and Aromatics) analysis as their columns are of the type PONA and DB-1 (Agilent J&W) for GC-1 and GC-2, respectively. Analysis of the liquid effluent is also possible via manual injection.

These GCs will be used for the determination of the concentration of internal standard in the feedstock. Relative sensitivity values (RS) are used to define the true area (A_e) of each component. Normalizing the results will subsequently give the weight percent of every component:

$$A_{i,e} = \frac{A_i}{RS_i} \tag{3-11}$$

The relative sensitivity values of different components present during ethanol dehydrogenation, along with their retention times (RT), are listed in Table 3-4. For a number of samples a calibration line is constructed for which the slope will represent the ratio of the relative sensitivity values. The value of hexane is set at a constant value as according to Dietz [15] in order to determine the values of the different components. The value of methane is also derived from Dietz.

The values for the relative sensitivity were determined via calibration, based on the known concentration of the internal standard, i.e., hexane:

$$\frac{A_i}{A_{IS}} = \frac{RS_i}{RS_{IS}} \frac{C_i}{C_{IS}} \tag{3-12}$$

Table 3-4: Relative sensitivity (FID) and retention time of possible products and reactants [15]

Component	RS_i	RT_i (min)
Methane	0.97	5.745
Acetaldehyde	0.265	6.376
Ethanol	0.492	7.008
Diethyl ether	0.580	7.777
Ethyl acetate	0.420	9.555
Hexane	1.03	9.815

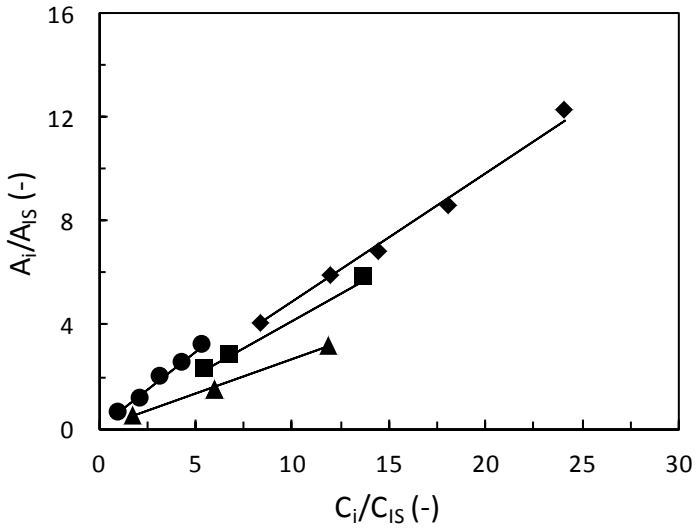

Figure 3-7: Calibration lines for ethanol (diamonds), acetaldehyde (triangles), ethyl acetate (cubes) and diethyl ether (circles)

The analysis of the reactor effluent during this work is performed in the second part of the gas analysis section via a µGC from Agilent Technologies of the type 3000 Micro GC. That way, a fast and reliable measurement of the gaseous effluent is allowed which is desirable for online sampling. The µGC contains four columns in parallel:

- Molesieve column: separation of permanent gases and methane
- PLOTU column: separation of C_2 and C_3 hydrocarbons
- Alumina column: separation of C_3 and C_4 hydrocarbons
- OV-1 column: isomer separation of C_4 to C_6 hydrocarbons

Analysis occurs via a thermal conductivity detector (TCD) which measures the conductivity of the sample and compares it to a reference component via a Wheatstone bridge. Since no ionization is occurring, it will be possible to measure gases such as nitrogen and carbon monoxide. The latter, however, will be calculated based on the formation of methane as it is produced in equimolar amounts.

The determination of the weight percentage of every component in the reaction mixture is determined via weight factors (WF) provided by Dietz [15]. These were evaluated with the calibrated

factors by comparison between chromatograms of the microGC and the GCs with FID detector. The same principle as for equation (3-11) holds, though, one has to bear in mind that the weight factors are the inverse of the relative sensitivities. The weight factors along with retention times for the different components are listed in Table 3-5. The weight percentages of the different components in the feed are then defined as follows:

$$y_k = \frac{WF_k A_k}{\sum_i^n WF_i A_i} \tag{3-13}$$

Table 3-5: Weight factor and retention time of components of the reaction mixture [15]

Component	WF_i	RT_i (min)	Abbreviation
Methane	0.45	0.239	CH4
Acetaldehyde	0.68	0.273	AcH
Ethanol	0.64	0.325	EtOH
Diethyl ether	0.67	0.407	EtOEt
Ethyl acetate	0.79	0.570	EtOAc
Hexane	0.7	0.655	nC6

3.5 KINETICS MEASUREMENTS

The conversion and selectivity during kinetics testing are determined according to the equations provided by the course of Chemical Reactors: Fundamentals and Applications by Guy B. Marin at Ghent University [13]. The corresponding flow rates are calculated from the weight percentages of the component and the internal standard, derived by equation (3-13):

$$F_k = \frac{y_k}{y_{IS}} \frac{MM_{IS}}{MM_k} F_{IS} \tag{3-14}$$

With MM_i Molar mass of component i [g mol^{-1}]
F_i Molar flow rate of component i [mol s^{-1}]

The internal standard is hereby indicated by the subscript IS. The conversion of ethanol is consequently calculated as follows:

$$X_{EtOH} = \frac{F_{EtOH,0} - F_{EtOH}}{F_{EtOH,0}} \tag{3-15}$$

The selectivity is determined via equation (3-16):

$$S_k = \frac{C_{a,k}(F_k - F_{k,0})}{C_{a,EtOH}(F_{EtOH,0} - F_{EtOH})} \tag{3-16}$$

With $C_{a,k}$ Number of atoms a in component K

For the calculation of the selectivity, the carbon balance will be used.

4 REFERENCES

[1] X. Duan, D.G. Evans, Layered double hydroxides, Springer Science & Business Media2006.
[2] A. Ota, E.L. Kunkes, I. Kasatkin, E. Groppo, D. Ferri, B. Poceiro, R.M.N. Yerga, M. Behrens, Comparative study of hydrotalcite-derived supported Pd2Ga and PdZn intermetallic nanoparticles as methanol synthesis and methanol steam reforming catalysts, J Catal, 293 (2012) 27-38.
[3] P.P. Sun, G. Siddiqi, M.F. Chi, A.T. Bell, Synthesis and characterization of a new catalyst Pt/Mg(Ga)(Al)O for alkane dehydrogenation, Journal of Catalysis, 274 (2010) 192-199.
[4] V. Galvita, G. Siddiqi, P.P. Sun, A.T. Bell, Ethane dehydrogenation on Pt/Mg(Al)O and PtSn/Mg(Al)O catalysts, Journal of Catalysis, 271 (2010) 209-219.
[5] G. Siddiqi, P.P. Sun, V. Galvita, A.T. Bell, Catalyst performance of novel Pt/Mg(Ga)(Al)O catalysts for alkane dehydrogenation, Journal of Catalysis, 274 (2010) 200-206.
[6] P.P. Sun, G. Siddiqi, W.C. Vining, M.F. Chi, A.T. Bell, Novel Pt/Mg(In)(Al)O catalysts for ethane and propane dehydrogenation, Journal of Catalysis, 282 (2011) 165-174.
[7] M.J. Climent, A. Corma, S. Iborra, K. Epping, A. Velty, Increasing the basicity and catalytic activity of hydrotalcites by different synthesis procedures, J Catal, 225 (2004) 316-326.
[8] I. Chorkendorff, J.W. Niemantsverdriet, Concepts of modern catalysis and kinetics, John Wiley & Sons2006.
[9] S. Brunauer, P.H. Emmett, E. Teller, Adsorption of gases in multimolecular layers, Journal of the American chemical society, 60 (1938) 309-319.
[10] E.P. Barrett, L.G. Joyner, P.P. Halenda, The determination of pore volume and area distributions in porous substances. I. Computations from nitrogen isotherms, Journal of the American Chemical society, 73 (1951) 373-380.
[11] M. Saeys, Surface Phenomena and Catalysis, Ghent University, 2015.
[12] Z.X. Chen, K.M. Neyman, A.B. Gordienko, N. Rosch, Surface structure and stability of PdZn and PtZn alloys: Density-functional slab model studies, Phys Rev B, 68 (2003).
[13] K. Van der Borght, K. Toch, V.V. Galvita, J.W. Thybaut, G.B. Marin, Information-Driven Catalyst Design Based on High-Throughput Intrinsic Kinetics, Catalysts, 5 (2015) 1948-1968.
[14] Aspen Plus®, http://www.aspentech.com/products/engineering/aspen-plus/
[15] W.A. Dietz, Response Factors for Gas Chromatographic Analyses, J Gas Chromatogr, 5 (1967) 68-&.

Chapter 4: Characterization of Catalysts

1 INTRODUCTION

In order to obtain fundamental insight in the link between catalyst synthesis and activity, the properties of the catalysts have to be determined. Via several techniques such as XRD, TPR, TEM, etc., information can be obtained about the catalyst morphology, topology and composition. Via the combination of characterization techniques and kinetic tests, not only fundamental understanding of the phenomena, but also guidelines can be put forward, aiding the future catalyst design. During this chapter, the results obtained with the analysis techniques discussed in Chapter 3 are represented and used for a more in-depth analysis of the synthesis methods.

2 THE DIFFERENCE BETWEEN INCORPORATION AND IMPREGNATION

In Chapter 3, the synthesis methods applied in this work for the production of a PdZn intermetallic catalyst on a mixed oxide support were reported, i.e., wet incipient impregnation of Pd and Zn on the support and coprecipitation of the active metals Pd and Zn with the support. To elucidate the effect of synthesis on the catalyst properties, such as surface area, particle size, crystallographic structure, etc., characterization is key for further catalyst optimization. Since both catalysts are operated in the reduced state, both will be analyzed before and after reduction.

2.1 FORMATION OF THE PDZN INTERMETALLIC BOND

To ensure that the reduction operation is sufficient for the conversion of PdO and ZnO to PdZn, a temperature programmed reduction is applied on the mixed oxide. By means of these TPR measurements, the behavior of the catalyst could be examined in a hydrogen environment and simultaneously, the consumption of hydrogen gas could be detected over a wide range of temperatures. This measurement of the hydrogen consumption was performed at a constant temperature ramp of 5 K per minute and is represented in Figure 4-1 for both synthesis methods.

For the incorporated catalyst, only one clear peak can be distinguished at approximately 420 K which can be assigned to the reduction of PdO in the mixed oxide structure. At first, the reduction will result in the formation of metallic Pd, though, due to the excess of hydrogen, it is subsequently converted to a saturated hydride compound, PdH_x [1, 2]. Upon further increase in temperature, the hydrogen will again desorb and, that way, result in a spill-over on the ZnO present in the mixed oxide structure. Hence, the reduction to form metallic Zn will be facilitated [3]. Due to the fact that the hydrogen consumption already took place during formation of the hydride compound, no additional hydrogen consumption is observed. What should be further noted on the first signal is the fact that the reduction of pure PdO generally occurs at temperatures much lower than 400 K, indicating an extra stabilization of the PdO in the hydrotalcite derived structure [3].

$Mg(Al)(Pd)(Zn)O_x$ is synthesized with a molar Pd:Zn ratio of 1:2 in order to ensure a complete reduction of PdO to PdZn instead of metallic Pd. Palladium will increase the selectivity to methane via the decomposition of ethanol [4, 5]. This non-equimolar ratio will therefore result in the remaining presence of ZnO in the structure of the catalyst, further indicated as bulk ZnO. As the amount of Pd in the structure is not sufficient to act as a hydrogen carrier for all ZnO, a small, broad

peak can be observed at 700 K. Nonetheless, zinc will not completely reduce at these moderate temperatures. It was yet reported in literature that ZnO will not reduce for temperatures below 900 K in the absence of Pd [6], thus indicating that ZnO is remaining in the mixed oxide structure.

The impregnated catalyst is a different story as not one mutual peak is observed for the reduction of PdO and ZnO but two broader signals. The broadness can be contributed to the less uniform distribution of the PdO particles on the catalyst surface. That way, particles of smaller sizes are easier reduced with hydrogen than larger ones. Furthermore, the reduction peak of PdO appears at lower reduction temperatures than for the incorporated catalyst. This indicates that the impregnation of Pd ions will not obtain the same stabilization benefits as for the incorporated catalysts, indicated by the peak occurring at lower temperatures. The spill-over effect, measured for the incorporated catalyst could also be suggested here, resulting in the formation of metallic Zn. Next to this spill-over hydrogen, additional amounts will be consumed resulting in the corresponding signals above 600 K. The ZnO particles are less well distributed over the surface than for the incorporated catalyst. Larger differences in particle size are hence present, leading to broadening of the hydrogen consumption signal. Reduction of bulk ZnO will not occur for the impregnated catalyst as no ZnO is present inside the structure of the mixed oxide. Non-reduced ZnO will, as such, remain present at the surface of the catalyst.

The reduction procedure of the catalyst will comprise of a constant flow of hydrogen at a temperature of 823 K. According to previously obtained results both the reduction of PdO and ZnO should be achieved. The question, however, now rises if indeed the intermetallic compound PdZn is formed instead of a side by side formation of metallic Pd and Zn.

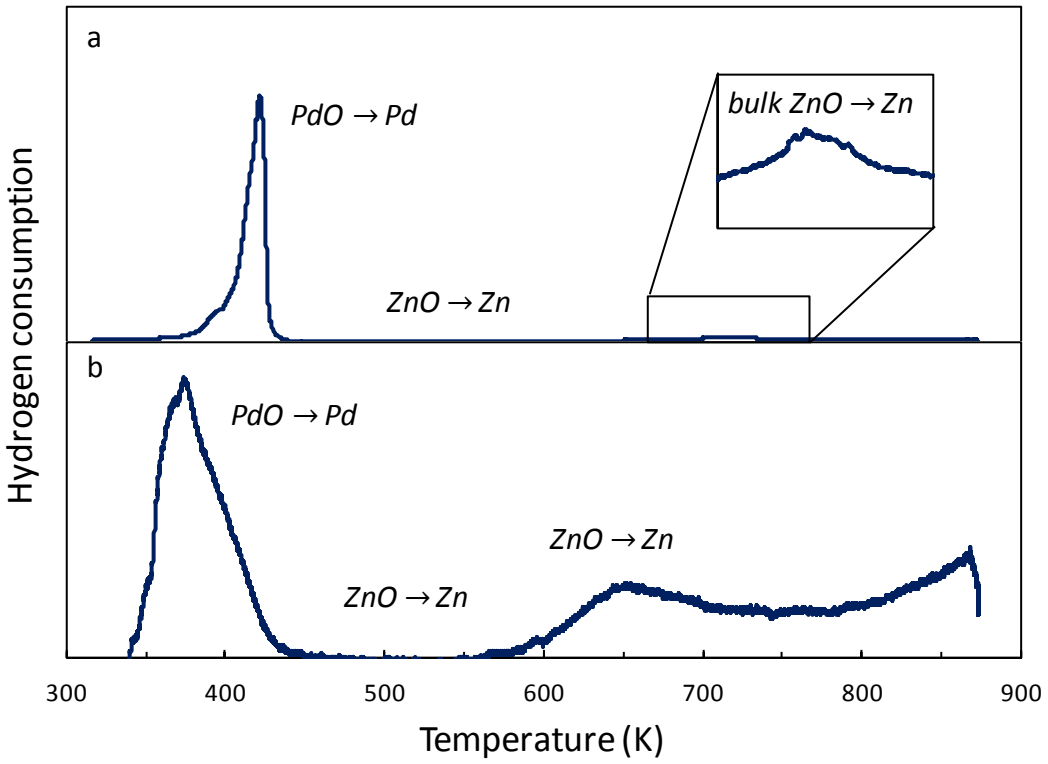

Figure 4-1: TPR profile of Mg(Al)(Pd)(Zn)O_x (a) and PdO,ZnO/Mg(Al)O_x (b)

An indication for the formation of the PdZn intermetallic compound can be found by measuring XRD spectra in order to identify the different crystallographic planes of the material. A representation of these spectra, for both the fresh and reduced samples of the synthesized catalysts, is shown in Figure 4-2. The peaks of the MgO periclase, distinctive for hydrotalcite based mixed oxides, will dominate the spectra with signals at 37°, 43° and 62°. Besides these signals of high intensity, which are present in all measured samples, strong differences are observed between the incorporated and impregnated catalysts. Relatively intense signals were detected for the former that remained unobserved for the latter indicating the presence of a phase unrelated to the mixed oxide structure. This missing component is sodium nitrate which remained present in the catalyst after the washing treatment and was not decomposed by calcination [7]. In literature, it was reported that sodium nitrate decomposes at temperatures above 623 K [8], so despite the fact that the applied calcination temperature of 873 K was adequate, no complete decomposition took place. A possible reasoning for this observation is the insufficient pulverization and washing of the catalyst before calcination resulting in a limited removal of $NaNO_3$ from the interlayered structure. The subsequent reduction which will take place at 823 K in a hydrogen environment will then eventually result in the disappearance of the signals. The impregnated catalyst shows no signals of sodium nitrate confirming that the washing treatment of this catalyst suffices.

The synthesis method of coprecipitation will lead to a mixed oxide structure in which both palladium and zinc oxides are incorporated in the structure. Due to the uniform distribution of Pd and Zn in the mixed oxide structure and thus small crystallographic phases of PdO and ZnO, no signals are observed for these compounds on the XRD spectra (sample d, Figure 4-2). For the impregnated catalyst, though, PdO and ZnO are grafted onto the surface of the catalyst forming, as such, larger particles with larger crystallographic planes, thereby giving rise to a clear observation of the peak corresponding to PdO and ZnO. This is represented by sample b in Figure 4-2.

Reduction of the catalysts (samples a and c, Figure 4-2) will show the disappearance of the palladium and zinc oxide signals while a new peak will appear at 42°. This signal can be assigned to the PdZn intermetallic compound and indicates as such the formation of the active sites for ethanol dehydrogenation. The sharper signal is observed for the incorporated catalyst. That way, one could argue that a more uniform distribution of PdO and ZnO gives rise to more intense signals in the XRD spectra. This reasoning states that due to the uniform distribution, diffusion of the zinc atoms in the palladium is enhanced, creating a more uniform surface of PdZn. In the impregnated catalyst, larger crystals of palladium will be present for which a complete diffusion of zinc atoms into the core is limited. The mechanism of diffusion of zinc into the palladium cores is yet described as the corresponding mechanism for the formation of PdZn [9], though XRD provides limited information for this phenomenon.

If the reduced samples are consequently subjected to a temperature programmed oxidation (temperature ramp of 5 K per minute), the disappearance of the PdZn signal could be observed as is shown in Figure 4-3. Despite the fact that the spectra are still dominated by the peaks corresponding to the MgO periclase, the presence of signals originating from PdO and ZnO can be observed at 34° and 55°, respectively. Originally, these peaks were not measured for the incorporated catalyst as the Pd and Zn ions were incorporated in the structure, giving rise to only very weak signals. That way, it

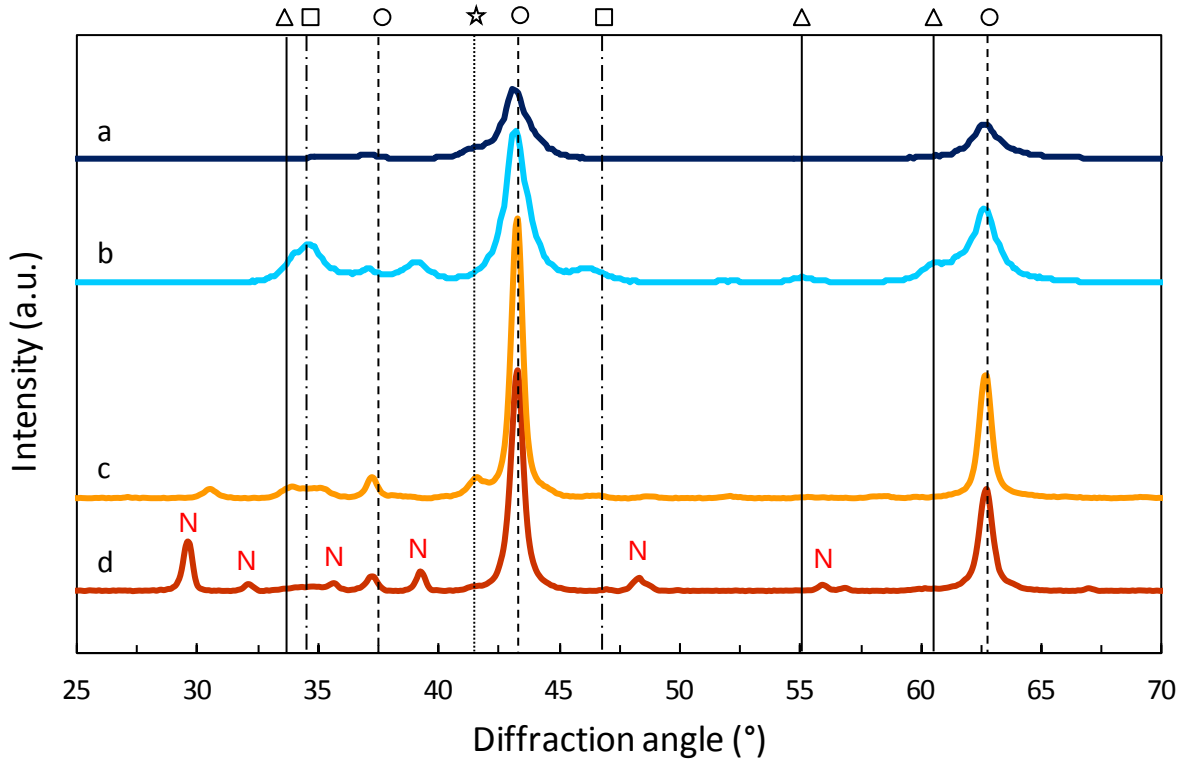

Figure 4-2: XRD spectra for PdZn/Mg(Al)O_x (a, dark blue), PdO,ZnO/Mg(Al)O_x (b, cyan), PdZn/Mg(Al)(Pd)(Zn)O_x (c, yellow) and Mg(Al)(Pd)(Zn)O_x (d, red)
(○: MgO; □: ZnO; △: PdO; ☆: PdZn; N: $NaNO_3$)

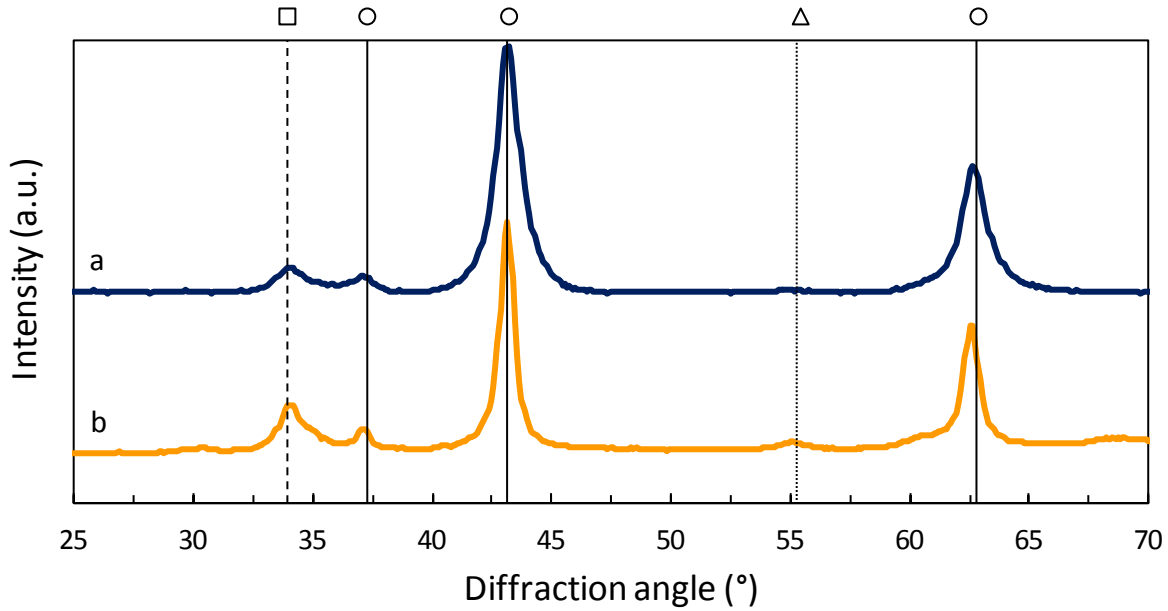

Figure 4-3: XRD spectra of PdZn/Mg(Al)O_x (a, dark blue) and PdZn/Mg(Al)(Pd)(Zn)O_x (b, yellow) after TPO (○: MgO; □: ZnO; △: PdO)

could be observed that both the Pd and Zn ions will diffuse out of the structure upon reduction and redistribute on the surface of the catalyst upon oxidation. This is investigated more thorough in Section 3.

A more in-depth understanding of the reduction mechanism to PdZn could be obtained by combining a technique that reduces the sample with a technique that tracks the presence of the intermetallic compound. Such a characterization method is found in TPR-XRD which will combine previously discussed techniques for a more thorough analysis. The TPR-XRD spectrum of the incorporated catalyst is shown in Figure 4-4. The temperature ramp applied during the reduction is set at 10 K per minute.

The peaks of $NaNO_3$, identified as the result of insufficient washing of the catalyst, show high intensity in the region between 300 and 400 K but will disappear due to decomposition at higher temperatures. Though the first calcination was not sufficient for removal, a second high-temperature treatment will. The smaller signals of PdO and ZnO observed in this temperature range will also disappear somewhat above 400 K and give rise to signals resembling the metallic forms of Pd and Zn. Hereby, Figure 4-4 illustrates that the peaks corresponding with the metallic zinc will lose intensity at lower temperatures than metallic palladium suggesting that the Zn will diffuse into the Pd particles. This diffusion of zinc in palladium was yet described in literature as the mechanism of formation of the PdZn intermetallic compound [9]. During the diffusion, the possibility exists of formation of an intermediate compound as the concentration of Zn will not directly be uniform over the entire Pd particle. One of the possible intermetallic compounds that could be formed during this diffusion is $PdZn_2$:

$$Pd + 2\,Zn \rightleftarrows\ PdZn_2$$

As the metallic zinc is not yet fully diffused to the core of the palladium, an egg-shell structure is possibly formed of a Pd core and a $PdZn_2$ mantle. That way, signals of both crystallographic structures should be observed. Corresponding signals of $PdZn_2$, however, are located at similar diffraction angles as Pd. A decisive answer on this formation, therefore, remains absent.

Furthermore Ota et al. reported the formation of another intermediate compound, Pd_2Zn [10]:

$$2\,Pd + Zn \rightleftarrows\ Pd_2Zn$$

Here, it was observed that next to the PdZn intermetallic compound, also egg-shell structures were present consisting of a Pd_2Zn core and a ZnO mantle. These structures were observed at temperatures of 573 K but disappeared at temperatures of 773 K. The only compound remaining at that point was PdZn. The measurements performed via TPR-XRD are, however, lacking in confirmation of the presence of this intermediate compound as the corresponding signal is located around 42°. At these diffraction angles, Pd and, possibly, $PdZn_2$ signals are formed in the same temperature range. The actual appearance of the PdZn intermetallic bond could be observed starting from temperatures around 550 K. The signals corresponding with the species are located at 31°, 42° and 44°. As such, TPR-XRD will provide the confirmation of the actual formation of the PdZn intermetallic compound during the reduction cycles at 873 K under a constant hydrogen flow.

Figure 4-5 shows the TPR-XRD spectrum of the impregnated catalyst. As was observed in the XRD spectra of Figure 4-2, no signals are detected representing $NaNO_3$. More intense signals, though, are witnessed for the oxides of Pd and Zn for which the former is observed to disappear faster as it is not stabilized by the mixed oxide support. The signal of the latter, on the contrary, will last much longer as it is less easy reduced on the impregnated catalyst. A possible reasoning for this phenomenon is that for impregnation, the oxides are forming larger clusters upon grafting. That way, reduction of these particles with hydrogen takes longer or requires higher temperatures.

During reduction, metallic Zn will diffuse into the Pd cores and consequently gives rise to the PdZn intermetallic compound. Whether or not, possible intermediates are formed before deriving the final compound remains an open question as signals corresponding to either Pd_2Zn or $PdZn_2$ are not possible to be distinguished from others. The occurrence of the PdZn intermetallic bond could be observed by the signals at 42° and 44°.

2.2 SURFACE STRUCTURE

During synthesis, calcination of the hydrotalcite precursors will give rise to a mixed oxide support. These mesoporous materials are known for their high surface area suggesting their suitability as a carrier for the PdZn active sites. This surface area is determined by nitrogen adsorption. The corresponding adsorption and desorption isotherms of the mixed oxides, prepared either via coprecipitation or via impregnation are shown in Figure 4-6, along with their isotherms after reduction.

Taking into account the classification constructed by Brunauer, Deming, Deming and Teller [11], the adsorption isotherms of both the incorporated and impregnated catalysts could be assigned as type IV isotherms. In the earlier pressure stages, monolayer adsorption will occur on the catalyst and this part of the isotherm will be used for the determination of the surface area, using the BET isotherm. The surface areas observed for the different catalysts are shown in Table 4-1. After fully occupying the monolayer, multilayer adsorption will occur until the maximum adsorption is attained, representing the form of a type IV isotherm.

Subsequent desorption shows the hysteresis due to capillary pore condensation within the mesopores of the catalyst. If one observes the shape of this hysteresis an indication of the uniformity of these pores is provided represented by the width. That way, it could be stated that all catalysts show a high uniformity in pore size. Furthermore, the average pore width is estimated via the BJH method by means of the Kelvin equation showing that for the different catalysts, larger pores are observed for the ones prepared via impregnation (Table 4-1). A possible hypothesis for this observation is that during synthesis of the incorporated catalyst Pd and Zn ions are introduced into the structure next to Al and Mg. The ionic radius of Pd, however, is much higher than Mg and especially than Al (Chapter 2, Table 2-3). As such, introducing the palladium ions will disturb the hydrotalcite structure and limit the formation of the characteristic layers. Subsequent calcination of the material to form the corresponding mixed oxide will then distort the structure but the pore size and surface area is enhanced in only a limited manner. The latter is also shown in Table 4-1.

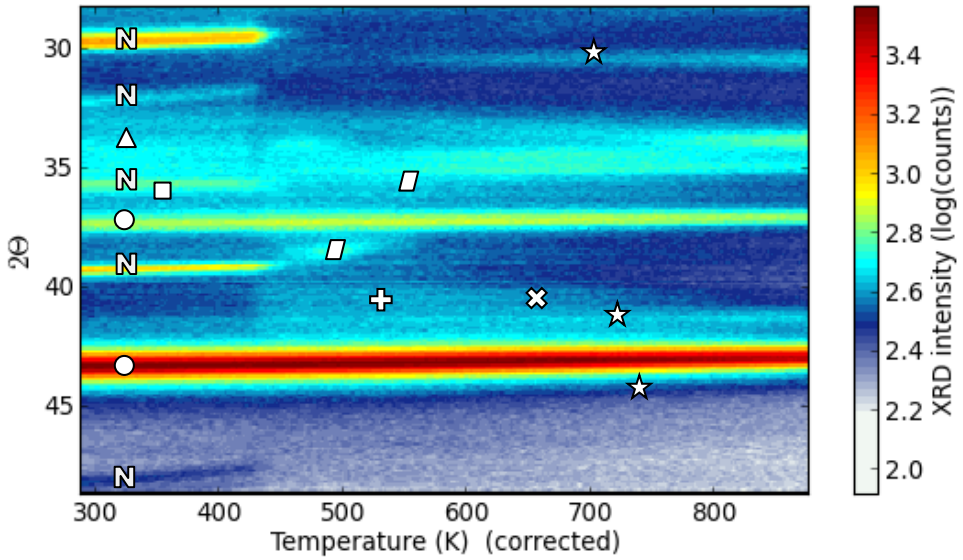

Figure 4-4: TPR-XRD spectrum of Mg(Al)(Pd)(Zn)O_x to PdZn/Mg(Al)(Pd)(Zn)O_x (△: PdO; □ : ZnO; ✚: Pd; ▱ : Zn; ✖: $PdZn_2$; ☆ : PdZn; ○ : MgO; ℕ: $NaNO_3$)

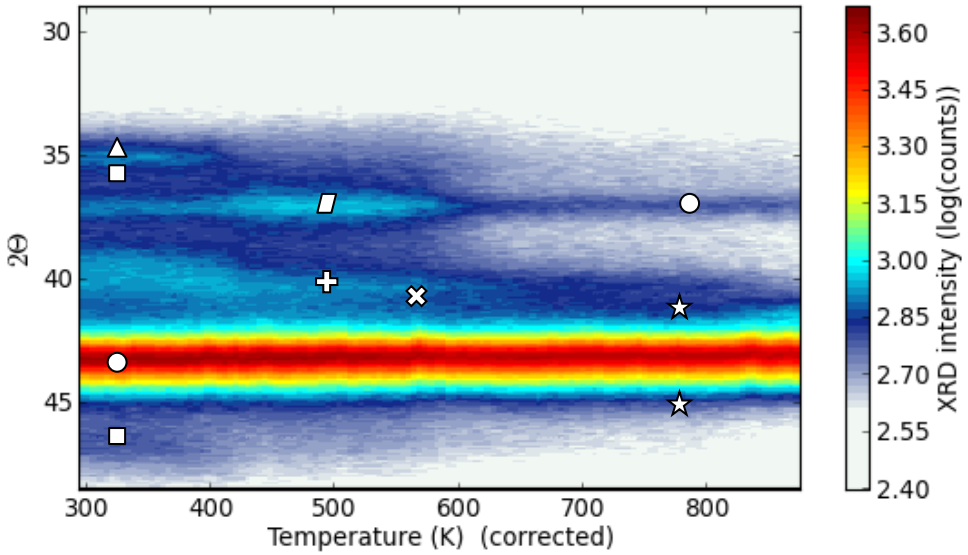

Figure 4-5: TPR-XRD spectrum of PdO,ZnO/Mg(Al)O_x to PdZn/Mg(Al)O_x (△: PdO; □ : ZnO; ✚: Pd; ▱ : Zn; ✖: $PdZn_2$; ☆ : PdZn; ○ : MgO)

For the impregnated catalyst, Pd and Zn ions are introduced on the calcined structure of the mixed oxide of Mg and Al and thus distributed over the surface. The sequencing calcination will then result in PdO and ZnO spread across the surface of the catalyst, limiting the pore size and surface area, though, in a more restricted way than for the incorporated catalyst for which the structure is disturbed.

Subsequent reduction with hydrogen to form the PdZn intermetallic compound will result in diffusion of metallic Pd to the surface. Hence, these PdO particles which disturb the distorted structure of the mixed oxide will be removed from the bulk structure and result in such manner in an increase of the surface area of approximately 120 %. The impregnated catalyst does not show this advantage as the PdO and ZnO particles are already well distributed across the surface during the impregnation. Here, reduction with hydrogen will lead to larger particles, hence lower dispersion and consequently the surface area will reduce as these particles will cover a higher area. As PdO and ZnO were yet well distributed inside the structure of the support for the incorporated catalyst, it could be expected that, here, the formed PdZn particles will be smaller and thus cover a lower surface area as less pores will be blocked or filled.

Reduction with hydrogen has an advantageous effect on the average pore size of the catalysts with especially the incorporated catalyst benefitting from this reduction. The same explanation could be applied as for the surface area since the PdO is no longer disturbing the bulk structure of the catalyst. Furthermore, both Pd and Zn ions are diffusing out of the structure towards the surface to form the intermetallic compound, resulting in free space inside the support structure. A similar reasoning could be applied to the impregnated catalyst. During impregnation, Pd and Zn ions were deposited into the pores of the catalyst, subsequent calcination of this catalyst would then result in the formation of PdO and ZnO inside the pores. After reduction, the Pd and Zn will diffuse out of the catalyst pores and form the PdZn intermetallic compound at the surface. That way, the average pore width would increase.

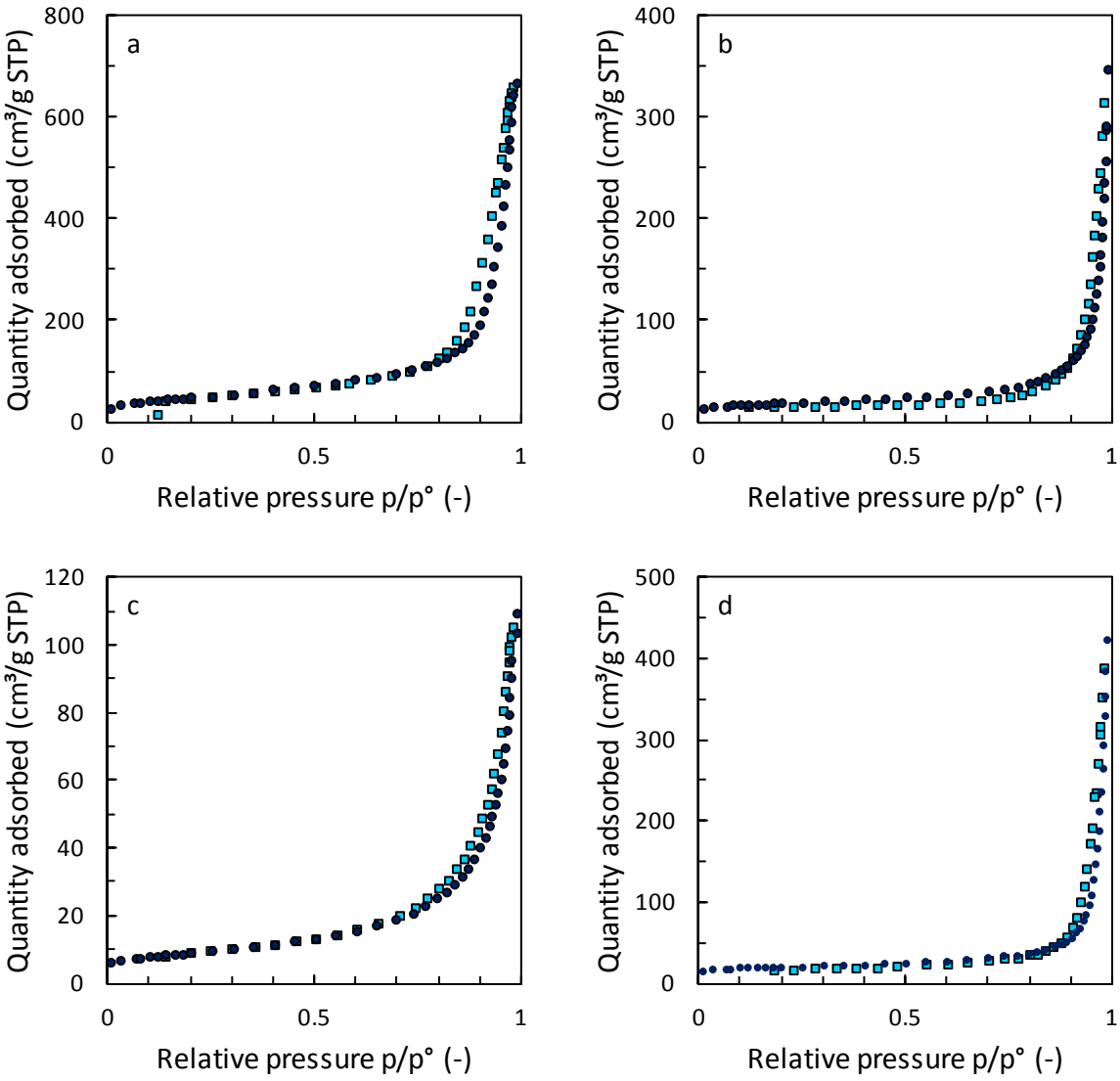

Figure 4-6: Adsorption-desorption (cubes-spheres) isotherms for PdO,ZnO/Mg(Al)O_x (a), PdZn/Mg(Al)O_x (b), Mg(Al)(Pd)(Zn)O_x (c) and PdZn/Mg(Al)(Pd)(Zn)O_x (d)

Table 4-1: Internal and active surface area of the different catalysts

Catalyst	BET surface area ($m^2\ g_{cat}^{-1}$)	BJH average pore width (nm)
Mg(Al)(Pd)(Zn)O_x	28.6 ± 2.1	201.3 ± 5.3
PdZn/Mg(Al)(Pd)(Zn)O_x	62.6 ± 2.4	540.5 ± 4.9
PdO,ZnO/Mg(Al)O_x	158.8 ± 6.6	221.5 ± 4.9
PdZn/Mg(Al)O_x	53.0 ± 9.7	388.7 ± 33.2

3 THE EFFECT OF REDUCTION CYCLES

A crucial step in the synthesis of the PdZn intermetallic compounds is reduction. The procedure that is applied during this step of the synthesis could hereby have a significant effect on the particle diameter distributions and consequently on the reactivity of the catalyst. In order to identify the effect of the reduction method, two different procedures are used:

- Short reduction cycle: red
- Complete reduction cycle: red-ox-red-ox-red

For the conditions at which both methods will take place, the reader is referred to Chapter 3. As the catalyst will possibly require regeneration, these procedures are also applied in between two reaction experiments to re-establish the PdZn compound, though, for the short procedure a preliminary oxidation is applied first.

3.1 PARTICLE SIZE DISTRIBUTION

TEM experiments are performed in order to quantify the amount of PdZn particles and to identify the distribution of their diameter. The corresponding distributions of the incorporated and impregnated catalyst, both for short and complete reduction cycles are illustrated in, respectively, Figure 4-7 and Figure 4-8. For the incorporated catalyst after a short reduction cycle (sample a, Figure 4-7) it is observed that a relatively wide distribution is located around an average particle diameter of 5 nm. Subsequent oxidation will then result in a redistribution of the PdO and ZnO particles over the surface. The reduction that follows this oxidation will consequently start from a more uniform surface. Hence, the PdZn particles formed during reduction with hydrogen will show a more narrow distribution. This is represented by the particle size distribution after a complete reduction cycle in Figure 4-7 (sample b). A small increase in the average particle diameter is observed owing to the redistribution of particles from both smaller and larger sizes. Further multiplying the number of oxidation-reduction cycles will then eventually result in a more uniform diameter, though, will also increase the time of regeneration. As a matter of compromise the number of reduction-oxidation cycles is therefore limited at two, followed by a finishing reduction (indicated as the complete reduction cycle) to restrict the regeneration period.

For the impregnated catalyst two different distributions are observed at diameters of approximately 5.5 and 11 nm (sample a, Figure 4-8). A hypothesis for the less uniform distribution of the particles over the surface of the impregnated catalyst could be found by the manner of addition of Pd and Zn in the structure of the catalyst. Grafting will cause a less ideal distribution of PdO and ZnO particles over the surface, giving hence rise to a wider particle size distribution of PdZn upon reduction with hydrogen. In this wide distribution, the maximum located at higher diameters, could possibly be assigned as the result of particles of PdZn clustering upon the high temperatures of the reduction. The fact that this is not occurring for the incorporated catalyst suggests the higher structural stability that is obtained for the PdZn particles with the support.

Increasing the number of oxidation-reduction cycles will cause a redistribution of the particles and, as such, a smaller distribution of particle diameters will be observed, indicated by sample b in Figure 4-8 with an average diameter of 7 nm and a standard deviation of 2.3 nm. This average particle size, however, remains higher than for the incorporated catalyst which could be assigned to the larger clusters resulting from grafting of the Pd and Zn ions on the surface. Incorporation will indeed result into a better distribution of these ions in the structure, showing beneficial results for the average particle size upon reduction with hydrogen. As the standard deviation of the particle diameter will decrease upon the number of oxidation-reduction cycles, the same reasoning could be applied as for the incorporated catalyst concerning time consumption. This number of cycles will, therefore, be limited to two cycles followed by a finishing reduction as a compromise for regeneration time.

3.2 ACTIVE SURFACE AREA

Based on the particle size distribution, determined via TEM measurements, the dispersion of the PdZn intermetallic compound could be calculated and hence the number of active sites over the catalyst surface is known. The dispersion and number of active sites of the catalyst determined via their particle size distribution (Figure 4-7 and Figure 4-8) are shown in Table 4-2. According to these values, it could be suggested that the short reduction cycle will initially give rise to slightly higher values of dispersion over the catalyst surface. Nonetheless, it is worth considering that the variation on the dispersion is remarkably higher if a short reduction cycle is applied, indicating the higher uniformity of the surface for a complete reduction cycle as was observed in the TEM measurements. It could therefore be argued that a complete reduction cycle would be more appropriate for reaction and regeneration due to the more uniform structure of the catalyst that is derived in this way.

Table 4-2: Number of active sites and dispersion of the catalysts determined via the particle size distribution

Catalyst	Reduction cycle	Number of active sites (g_{cat}^{-1})	Dispersion (-)
PdZn/Mg(Al)O_x	Short	$1.92\ 10^{-5} \pm 8.2\ 10^{-6}$	0.204 ± 0.088
PdZn/Mg(Al)O_x	Complete	$1.63\ 10^{-5} \pm 6.0\ 10^{-6}$	0.174 ± 0.064
PdZn/Mg(Al)(Pd)(Zn)O_x	Short	$2.66\ 10^{-5} \pm 2.03\ 10^{-5}$	0.283 ± 0.216
PdZn/Mg(Al)(Pd)(Zn)O_x	Complete	$2.15\ 10^{-5} \pm 9.4\ 10^{-6}$	0.229 ± 0.099

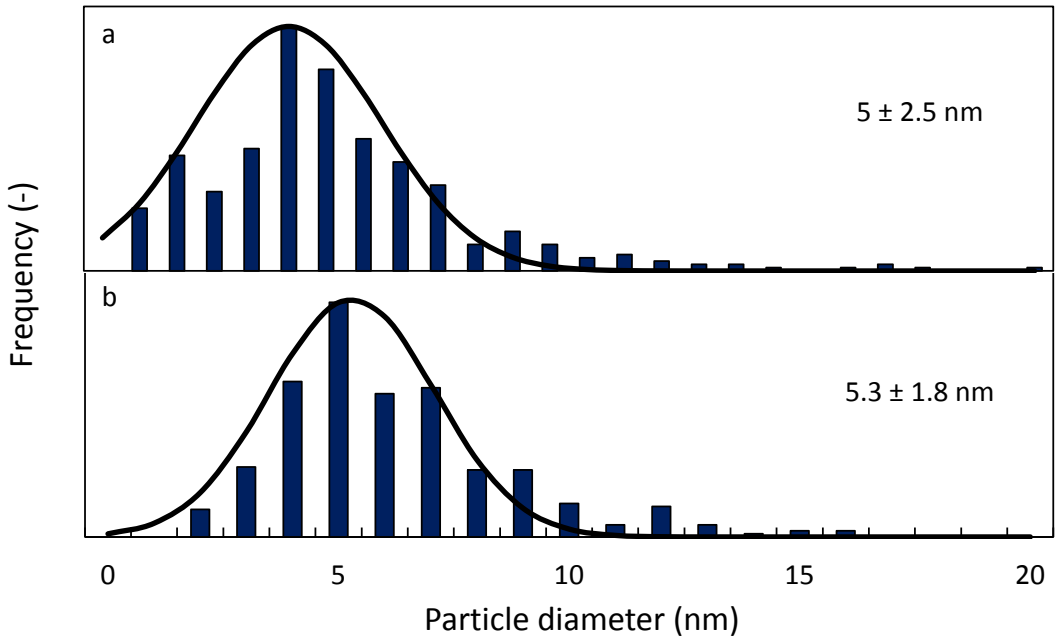

Figure 4-7: Particle diameter distributions of PdZn/Mg(Al)(Pd)(Zn)O_x after a short reduction cycle (a) or a complete reduction cycle (b)

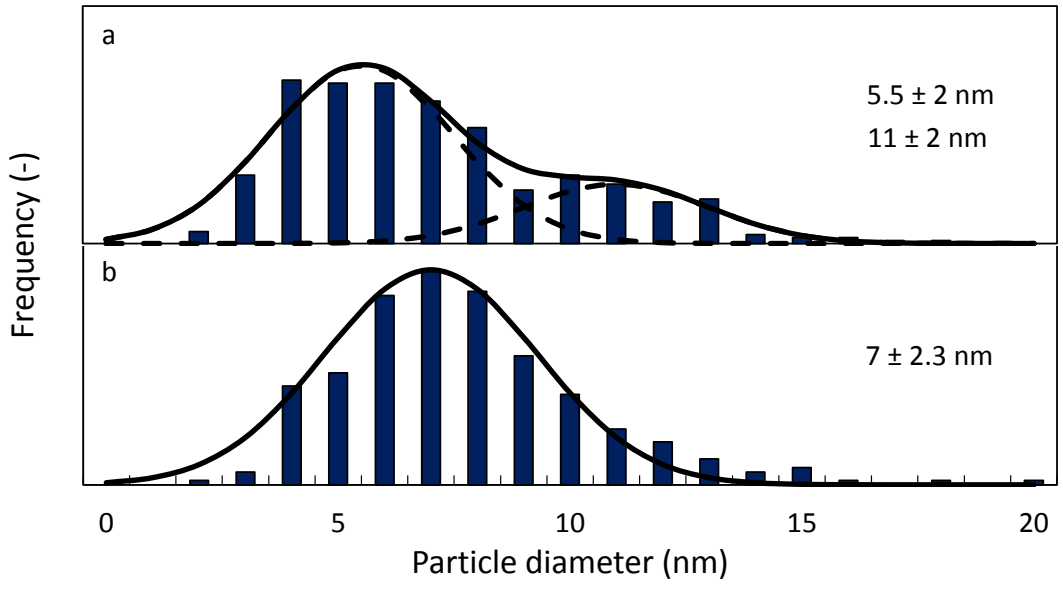

Figure 4-8: Particle diameter distributions of PdZn/Mg(Al)O_x after a short reduction cycle (a) or a complete reduction cycle (b)

4 CONCLUSIONS

Reduction of the PdZn intermetallic compound is successfully performed on the mixed oxide support. It is observed that metallic Zn will diffuse upon reduction with hydrogen into the metallic Pd forming the intermetallic compound. An important role could be assigned to Pd as it will act as a hydrogen carrier in its saturated hydride form. At higher temperatures, a spill-over of hydrogen over the ZnO particles will then ease the reduction to metallic Zn.

The formation of intermediate compounds during diffusion such as Pd_2Zn or $PdZn_2$, given entries in literature, however, remains an unsolved question. Hereby, it could be suggested that the formation of PdZn was easier obtained for the incorporated catalyst. As the Pd and Zn particles introduced on the impregnated catalyst via grafting were less well distributed and hence larger, reduction with hydrogen to form the PdZn intermetallic compound takes place at higher temperature ranges.

Surface area measurements point out the non-ideality of the mixed oxide formation when Pd ions were incorporated into the structure. Reduction with hydrogen, though, leads to diffusion of the ions to the surface and hence an increase in both surface area and pore size width. This effect is not observed for the impregnated catalyst as PdO and ZnO are grafted on the surface. Despite the decreasing surface area of the impregnated catalyst, the pore size width is still increasing as PdO and ZnO will leave the pores and form PdZn at the surface.

Alternating the reduction with oxidation cycles enables a redistribution of the oxides of Pd and Zn over the catalyst surface, hence creating a narrower particle size distribution. Especially in the case of the impregnated catalyst, a beneficial effect is observed as both small and larger clusters are present after only one reduction. As a higher number of cycles will comprise a higher regeneration time, the procedure is a compromise between time and uniformity of the catalyst surface. The number of reduction-oxidation cycles is, therefore, set at two with a finishing reduction step to form the PdZn intermetallic compound.

5 REFERENCES

[1] N. Iwasa, S. Masuda, N. Ogawa, N. Takezawa, Steam Reforming of Methanol over Pd/Zno - Effect of the Formation of Pdzn Alloys Upon the Reaction, Appl Catal a-Gen, 125 (1995) 145-157.
[2] N. Iwasa, T. Mayanagi, N. Ogawa, K. Sakata, N. Takezawa, New catalytic functions of Pd-Zn, Pd-Ga, Pd-In, Pt-Zn, Pt-Ga and Pt-In alloys in the conversions of methanol, Catal Lett, 54 (1998) 119-123.
[3] Y.H. Chin, R. Dagle, J.L. Hu, A.C. Dohnalkova, Y. Wang, Steam reforming of methanol over highly active Pd/ZnO catalyst, Catal Today, 77 (2002) 79-88.
[4] J.L. Davis, M.A. Barteau, Decarbonylation and Decomposition Pathways of Alcohols on Pd(111), Surf Sci, 187 (1987) 387-406.
[5] R. Shekhar, M.A. Barteau, Structure Sensitivity of Alcohol Reactions on (110) and (111) Palladium Surfaces, Catal Lett, 31 (1995) 221-237.
[6] Y.H. Wang, J.C. Zhang, H.Y. Xu, Interaction between Pd and ZnO during reduction of Pd/ZnO catalyst for steam reforming of methanol to hydrogen, Chinese J Catal, 27 (2006) 217-222.
[7] L. Hickey, J.T. Kloprogge, R.L. Frost, The effects of various hydrothermal treatments on magnesium-aluminium hydrotalcites, J Mater Sci, 35 (2000) 4347-4355.
[8] K.W. Jun, W.J. Shen, K.S.R. Rao, K.W. Lee, Residual sodium effect on the catalytic activity of Cu/ZnO/Al2O3 in methanol synthesis from CO2 hydrogenation, Appl Catal a-Gen, 174 (1998) 231-238.
[9] K. Fottinger, J.A. van Bokhoven, M. Nachtegaal, G. Rupprechter, Dynamic Structure of a Working Methanol Steam Reforming Catalyst: In Situ Quick-EXAFS on Pd/ZnO Nanoparticles, J Phys Chem Lett, 2 (2011) 428-433.
[10] A. Ota, E.L. Kunkes, I. Kasatkin, E. Groppo, D. Ferri, B. Poceiro, R.M.N. Yerga, M. Behrens, Comparative study of hydrotalcite-derived supported Pd2Ga and PdZn intermetallic nanoparticles as methanol synthesis and methanol steam reforming catalysts, J Catal, 293 (2012) 27-38.
[11] S. Brunauer, L.S. Deming, W.E. Deming, E. Teller, On a Theory of the van der Waals Adsorption of Gases, Journal of the American Chemical Society, 62 (1940) 1723-1732.

Chapter 5: Intrinsic Kinetics

1 INTRODUCTION

Chemical reactors are known as one of the most important parts within a chemical process and are often referred to as the heart of the chemical operation. A good understanding of the reaction kinetics ensures the construction of a validated kinetic model and is therefore of crucial importance for an accurate and safe reactor design. The study of these chemical kinetics for heterogeneous catalysis is a complex interplay of phenomena occurring both simultaneously and in series. Therefore, the reaction process can be broken down into a number of identifiable steps, all with their own relevant rate equations. Typically one can distinguish between following steps:

1. Mass transfer of reactant(s) (A) from the bulk to the catalyst surface
2. Mass transport of reactant(s) from the surface to the active site
3. Adsorption of reactant(s)
4. Catalytic reaction
5. Desorption of reaction product(s) (B)
6. Mass transport of reaction product(s) from the active site to the surface
7. Mass transfer of reaction product(s) from the surface to the bulk

A representation of previous steps is shown in Figure 5-1. One of the key issues that will arise at this point is the fact that all these phenomena could have a potential effect on the observed reaction rates. When performing the kinetic measurements that will be used for modeling purposes, it is of utmost importance that the true reaction rate is observed, i.e., k_{chem}. Though, mass transfer effects could interfere with the kinetic behavior, resulting in the measurement of an apparent rate coefficient, i.e., k_{app}. Hence to address solely these chemical phenomena within the mechanism, the focus must lie with the adsorption, reaction and desorption of the corresponding reactants and products.

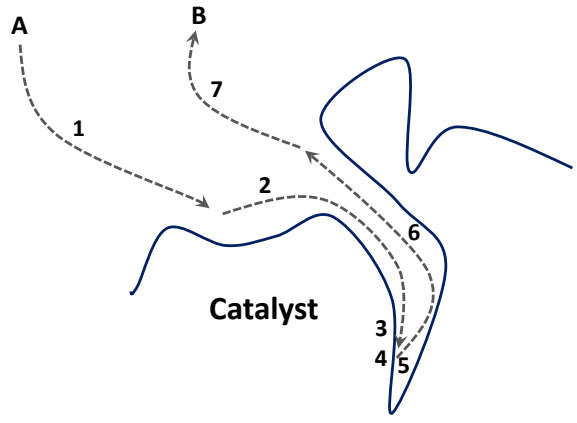

Figure 5-1: Sequence of reaction steps within heterogeneous catalysis

As the rate of these reactions will be depending on the concentration of the reactants and the temperature (via the Arrhenius relation), limitations regarding mass and heat transfer must be avoided as much as possible. To ensure lack of transfer phenomena during the measurement of the kinetics, i.e., the so called intrinsic kinetics regime [1], the reaction conditions shall be validated based on known correlations. The overall criterion will restrict the maximum deviation of the observed rate from the intrinsic reaction rate to 5 % and is shown in equation (5-1). This condition will be applied as guidance throughout this chapter to derive the corresponding criteria.

$$\frac{|R_{w,A}^{obs} - R_{w,A}^{int}|}{R_{w,A}^{int}} < 0.05 \tag{5-1}$$

With $R_{w,A}^{obs}$ Observed specific production rate of A (mol s^{-1} kg_{cat}^{-1})
$R_{w,A}^{int}$ Intrinsic specific production rate of A (mol s^{-1} kg_{cat}^{-1})

2 RESTRICTIONS ON REACTOR SCALE: PLUG FLOW REGIME

The reactor applied in the catalytic testing of reaction rates is a plug flow reactor (PFR, Chapter 3: Procedures). Some disadvantages are, however, encountered with these types of reactors [2]:

- PFR experiments typically yield conversions rather than rates
- Low flow rates can lead to concentration gradients over the stagnant layer surrounding the catalyst pellets
- Isothermicity is difficult to achieve

Due to the former restriction, the production rates need to be determined from the conversion and space time via following condition:

$$\frac{dX_A}{d\frac{W}{F_{A,0}}} = -R_{w,A}^{obs} \tag{5-2}$$

With X_A Conversion of A [-]
W Catalyst weight [kg_{cat}]
$F_{A,0}$ Inlet flow rate [mol s^{-1}]

As this condition is solely valid if one operates in the ideal plug flow regime, it will be required to apply criteria to ensure the absence of axial or radial gradients and complete isothermicity.

2.1 AXIAL DIFFUSION

Diffusion and local flows around catalyst particles and along the wall may cause a disturbing axial dispersion. As the presence of this phenomenon will lead to a lower conversion, a higher reactor length is required to derive the same results. Therefore, the general criterion for the length of the catalyst bed takes into account the increase necessary to achieve the same conversion in comparison to ideal plug flow:

$$\frac{L - L_P}{L} < 0.05 \tag{5-3}$$

With L Length of the reactor [m]
L_p Length of the reactor with ideal plug flow regime [m]

A similar expression can be found for the residence time:

$$\frac{\tau_{0,P}}{\tau_0} < 0.95 \tag{5-4}$$

With τ_0 Residence time of the reactor [s]
$\tau_{0,P}$ Residence time of the reactor with ideal plug flow regime [s]

The concentration of a reactant at the end of the reactor for an irreversible first order reaction with axial diffusion can be written as:

$$C_A = C_{A,0} \exp[-k\tau_0] \exp[\frac{(k\tau_0)^2}{Pe_a}] \tag{5-5}$$

With C_A Concentration of A [mol m^{-3}]
$C_{A,0}$ Inlet concentration of A [mol m^{-3}]
k Rate coefficient of the first order reaction of A [s^{-1}]
Pe_a Péclet number (axial) [-]

For a complete derivation, the author refers to the course of Chemical Reactors: Fundamentals and Applications of Guy B. Marin at Ghent University [3]. This expression will introduce a new dimensionless number, the Péclet number, which is the representation of the time scale of diffusion over the one of convection. The expression and its relation with the axial pellet Péclet number is represented by following equation:

$$Pe_a = \frac{u_s L}{D_{ea}} = \frac{u_s d_p}{D_{ea}} \frac{L}{d_p} = Pe'_a \frac{L}{d_p} \tag{5-6}$$

With u_s Superficial velocity [m s^{-1}]
d_p Pellet diameter [m]
D_{ea} Effective axial diffusion coefficient [m^2 s^{-1}]

Combining expressions (5-4) to (5-6) with the expression for the conversion of a first order irreversible reaction in the ideal plug flow regime, will then give rise to a general criterion for the length of the reactor bed to ensure ideal plug flow behavior:

$$\frac{L}{d_p} > \frac{20}{Pe'_a} \ln[\frac{1}{1 - X_A}] \tag{5-7}$$

Which will be multiplied with the reaction order n in case of higher order reactions. For intermediate conversions, following rule of thumb can be considered:

$$\frac{L}{d_p} > 50 \tag{5-8}$$

2.2 RADIAL DIFFUSION

The difference in density of the packing between the center and near the wall, along with the flat surface of the wall, also may cause deviations from ideal plug flow behavior. This will cause a radial velocity profile as the velocity at the wall will be higher than in the center. As such, the reactants will bypass the packing and affect the conversion. In analogy with axial diffusion, a Péclet number is defined:

$$Pe'_{mr} = \frac{u_s d_p}{D_{er}} \tag{5-9}$$

With D_{er} Effective radial diffusion coefficient [$m^2\ s^{-1}$]

Froment [4] accounted for the wall effects by applying a correction factor to the Péclet number:

$$\frac{Pe'_{mr}}{1 + 19.4\,(\frac{d_p}{d_t})^2} = \frac{u_s d_p}{D_{er}} \tag{5-10}$$

With d_t Tube diameter [m]

For high diameter ratios in the second term of the denominator, the Péclet number will closely resemble the original one as wall effects can be neglected. Following rule of thumb will therefore be applied to account for radial dispersion:

$$\frac{d_t}{d_p} > 10 \tag{5-11}$$

2.3 ISOTHERMAL OPERATION

Next to the absence of axial and radial diffusion, it is required to operate the reactor isothermally as small deviations in temperature can have significant effects on the measured reaction rates. On the reactor scale, one can distinguish between axial and radial temperature gradients. The former gradient offers the advantage that it can be measured along the axial coordinate, which is the case for the experimental reactor (Chapter 3). Furthermore, inert material is added to dilute the catalyst bed in order to decrease the generated heat per unit of volume and also, to increase the conductivity of the bed. Though, it requires some attention that one cannot dilute at random. This is due to the fact that a large amount of dilution will increase the probability that a part of the gas feed will bypass the catalyst as it will be more difficult to achieve a uniform distribution. Berger et al. [5] proposed following criterion for maximum bed dilution:

$$b < \frac{1}{1 + \frac{10\,X_{dil} d_p}{L}} \tag{5-12}$$

With b Volume of inert material as fraction of total volume of solids [$m^3_{inert} m^{-3}_{inert+catalyst}$]

X_{dil} Conversion obtained with the diluted bed [-]

Radial temperature gradients on the other hand, are not measurable and impose therefore additional criteria. Intuitively, it is clear that decreasing the diameter of the reactor tube increases the surface area to volume ratio and the superficial velocity, ameliorating as such the heat transfer. However, as was shown by expression (5-11), this will be in competition with the criteria for ideal plug flow.

Therefore a criterion is proposed, taking into account the resistance against heat transfer at the wall to account for possible wall effects. If this is combined with the general criterion illustrated by expression (5-1), following restriction is derived:

$$\frac{|\Delta_r H| r_w^{obs} \rho_p (1-\varepsilon_B)(1-b) d_t^2}{\lambda_{er} T_{wi}} < \frac{1.6 \frac{R T_{wi}}{E_a}}{1 + 8 \frac{\lambda_{er}}{\alpha_w d_t}} \tag{5-13}$$

With $\Delta_r H$ Reaction enthalpy [J mol^{-1}]
ρ_p Density of the catalyst pellet [kg_{cat} m_p^{-3}]
$1-\varepsilon_B$ Fraction of reaction volume, occupied by catalyst bed [m_B^3 m_r^{-3}]
$1-b$ Fraction of catalyst bed, occupied by catalyst pellet [m_p^3 m_B^{-3}]
T_{wi} Internal wall temperature [K]
λ_{er} Effective radial heat conductivity [W m_r^{-1} K^{-1}]
E_a Activation energy [J mol^{-1}]
α_w Heat transfer coefficient between bed and reactor wall [W m_r^{-2} K^{-1}]
R Gas constant [8.314 J mol^{-1} K^{-1}]

For a more detailed elaboration, the reader is referred to Mears [6].

2.4 ISOBARIC OPERATION

Besides isothermal operation and the absence of radial and axial gradients, a pressure drop over the reactor need to be avoided as much as possible in order to maintain ideal plug flow. The pressure drop, mainly caused by friction, can be represented over the axial coordinate via a momentum balance. For an empty tube, following balance can be considered [3]:

$$\frac{dp}{dz} = -2 f \frac{\rho_f u_s^2}{d_t} \tag{5-14}$$

With f Friction factor [-]
ρ_f Density of the fluid [kg m_f^{-3}]

Since a packed bed reactor is considered, some modifications are required taking into account the porosity and tortuosity of the catalyst bed. This transforms equation (5-14) into:

$$\frac{dp}{dz} = -3 f_B \tau_B^{1/2} \frac{1-\varepsilon_B}{\varepsilon_B^3} \frac{\rho_f u_s^2}{d_p} \tag{5-15}$$

With f_B Friction factor for a packed bed [-]
τ_B Tortuosity of the bed [m^2 m^{-2}]

ε_B Porosity of the bed [m_f^3 m_r^{-3}]

According to Blake-Kozeny, a relationship can be defined between the friction factor and the Reynolds number in the laminar regime. In the turbulent regime, the friction factor is considered to be independent of the Reynolds number, resulting in contributions for both regimes:

$$f_B = \frac{16}{Re_{p,B}} + a \tag{5-16}$$

With $Re_{p,B}$ Reynolds number around catalyst pe llet in a packed bed [-]
a Constant for the contribution in the turbulent regime [-]

Elimination of f_B, along with introducing empirical values for the tortuosity of the catalyst bed will then give rise to the Ergun equation:

$$\frac{dp}{dz} = -150\,\frac{(1-\varepsilon_B)^2}{\varepsilon_B^3}\frac{\mu\, u_s}{d_p^2} - 1.75\,\frac{(1-\varepsilon_B)}{\varepsilon_B^3}\frac{\rho\, u_s^2}{d_p} \tag{5-17}$$

A general rule of thumb to apply towards the maximum pressure drop in the reactor is the allowance of maximally 20 % of the total reactor pressure, bearing in mind the reaction order [2]:

$$\Delta P < \frac{0.2\, P_{tot}}{n} \tag{5-18}$$

With n Reaction order [-]
P_{tot} Reactor pressure [Pa]

3 RESTRICTIONS ON PELLET SCALE: TRANSPORT LIMITATIONS

On the pellet scale, one can distinguish between internal and external transport limitations, occurring respectively simultaneously or in series with reaction. A representation of these gradients is shown in Figure 5-2. For both mass and heat transport, limitations will occur, indicating that the bulk temperature and concentration are not an accurate representation of the actual values inside the catalyst pellet in case of strong limitations. For this reason, criteria are introduced to evaluate if these effects are present. For the criteria it is assumed that solely one limitation is occurring at once.

3.1 EXTERNAL TRANSPORT LIMITATIONS

3.1.1 MASS TRANSPORT

The general criterion, represented by equation (5-1), will be used as starting point for the derivation of the criteria. The intrinsic rate can hereby be considered as the production rate at bulk conditions. Deviations from these conditions are then taken into account by applying a Taylor expansion, neglecting higher order terms:

$$R_{w,A} = R_{w,A}^b + \frac{dR_{w,A}}{dC_A}|_{C_{A,b}}(C_A - C_{A,b}) \tag{5-19}$$

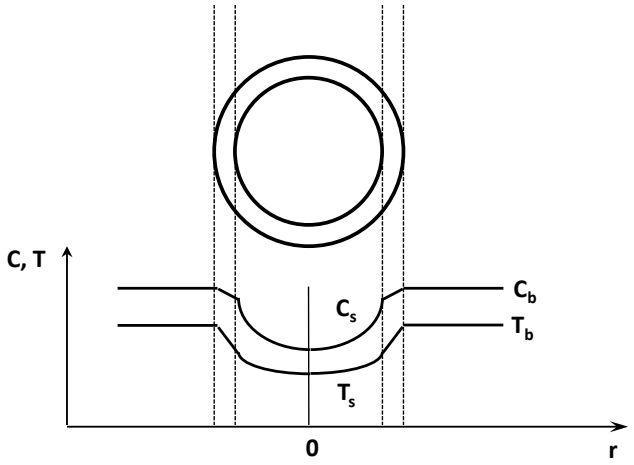

Figure 5-2: Concentration and temperature gradients in and around the catalyst pellet

With $R_{w,A}{}^{b}$ Specific production rate of A at bulk conditions [mol s^{-1} kg_{cat}^{-1}]
$C_{A,b}$ Concentration of A at bulk conditions [mol m^{-3}]

After introduction of equation (5-1) this will give:

$$\frac{|C_{A,b} - C_{A,s}|}{C_{A,b}} < \frac{0.05}{n} \tag{5-20}$$

With $C_{A,s}$ Concentration of A at surface conditions [mol m^{-3}]

As reaction and transport are occurring in series, a mass balance can be applied over a conceptual film around the catalyst pellet in steady state:

$$R_{w,A}^{obs} = k_{f,A} a_s (C_{A,b} - C_{A,s}) \tag{5-21}$$

With $k_{f,A}$ Mass transfer coefficient [m_f^3 m_i^{-2} s^{-1}]
a_s Specific external surface area [m_i^2 kg_{cat}^{-1}]

A combination of (5-20) and (5-21) results subsequently in the criterion for external mass transport limitations:

$$\frac{|R_{w,A}^{obs}|}{k_{f,A} a_s C_{A,b}} < \frac{0.05}{n} \tag{5-22}$$

The mass transfer coefficient is determined via the Sherwood number which is calculated according to the J_D analogy of Chilton-Colburn:

$$k_{f,A} = \frac{k_{f,A}{}^{\circ}}{y_{f,A}} = \frac{1}{y_{f,A}} \frac{D_A Sh}{d_p} = \frac{1}{y_{f,A}} \frac{D_A}{d_p} j_D Re_p Sc^{\frac{1}{3}} \tag{5-23}$$

In which

$$Re_p = \frac{\rho\, u_s d_p}{\mu} \quad and \quad Sc = \frac{\mu}{\rho\, D_A} \tag{5-24}$$

With D_A Molecular diffusion coefficient [m_f^2 s^{-1}]

μ Dynamic viscosity [kg m_f^{-1} s^{-1}]

$y_{f,A}$ Film factor [-]

The film factor will imply a correction for non-equimolar counter diffusion via the conceptual film. For a stoichiometric single reaction it holds [3]:

$$y_{f,A} = \frac{(1 + y_{A,b}\sum_j \frac{\upsilon_j}{\nu_A}) - (1 + y_{A,s}\sum_j \frac{\upsilon_j}{\nu_A})}{\ln[\frac{1 + y_{A,b}\sum_j \frac{\upsilon_j}{\nu_A}}{1 + y_{A,s}\sum_j \frac{\upsilon_j}{\nu_A}}]} \tag{5-25}$$

For which it holds that

$$\sum_j \nu_j A_j = 0 \tag{5-26}$$

Many correlations exist to calculate the J_D factor for gas phase reactions in packed beds. Sen Gupta and Thodos [7] proposed following relation:

$$j_D = 0.01 + \frac{0.863}{Re_p^{0.58} - 0.483} \; for \; Re_p > 1 \tag{5-27}$$

3.1.2 HEAT TRANSPORT

An analogous approach can be applied towards deviations from the bulk temperature. The Arrhenius relation will hereby be introduced, neglecting the temperature dependence of the pre-exponential factor:

$$R_{w,A} = R_{w,A}^b + \frac{dR_{w,A}}{dT}|_{T_b}(T - T_b) \tag{5-28}$$

In which

$$R_{w,A} = A \exp[-\frac{E_a}{RT}] f(C_A) \tag{5-29}$$

With T_b Temperature at the bulk [K]

A Pre-exponential factor [mol s^{-1} m^{-3} (mol s^{-1} m^{-3})$^{-n}$]

Combined with (5-1), this will then result in:

$$\frac{E_a|T_s - T_b|}{RT_b{}^2} < 0.05 \tag{5-30}$$

The heat balance over the conceptual film in steady state is represented by equation (5-31):

$$\rho_p r_{w,A}^{obs} |\Delta_r H| \frac{\pi}{6} d_p^3 = \alpha \, |T_s - T_b| \, \pi \, d_p^2 \tag{5-31}$$

With α Heat transfer coefficient over the film [W m_i^{-2} K^{-1}]

$r_{w,A}{}^{obs}$ Observed specific reaction rate [mol s^{-1} kg_{cat}^{-1}]

As such, the criterion for external heat transfer limitations can be derived:

$$\frac{\rho_p r_{w,A}^{obs} |\Delta_r H| \, d_p}{\alpha T_b} < 0.3 \frac{R T_b}{E_a} \tag{5-32}$$

The heat transfer coefficient α is determined via the Nusselt number. This dimensionless number is calculated analogously to mass transfer via a j_H factor proposed by Chilton-Colburn:

$$\alpha = \frac{\lambda}{d_p} Nu_p = \frac{\lambda}{d_p} j_H Re_p Pr^{\frac{1}{3}} \tag{5-33}$$

In which

$$Pr = \frac{\mu \, c_p}{\lambda} \tag{5-34}$$

With c_p Specific heat capacity [J kg^{-1} K^{-1}]
λ Heat conduction coefficient [W m^{-1} K^{-1}]

Several correlations exist for the determination of j_H. By Acetis and Thodos [8] following correlation was proposed:

$$j_H = \frac{1.10}{Re_p^{0.41} - 0.15} \; for \; 13 < Re_p < 2136 \tag{5-35}$$

3.2 INTERNAL TRANSPORT LIMITATIONS

3.2.1 MASS TRANSPORT

In heterogeneous catalysis, the Thiele modulus and in extension the effectiveness factor can be defined to represent the effect of internal mass transport limitations on the chemical reaction:

$$\phi = \frac{1}{a_v} \sqrt{\frac{k_v}{D_{A,e}}} \tag{5-36}$$

and

$$\eta = \frac{a_v N_A|_{r'=1}}{R_v(C_{A,b})} = \frac{R_{w,A}^{obs}}{R_{w,A}^{int}} \tag{5-37}$$

With k_v Volumetric rate coefficient [s^{-1}]
$D_{A,e}$ Effective diffusion coefficient [m_f^3 m_p^{-1} s^{-1}]
a_v Volumetric surface area at which reaction occurs [m_i^2 m^{-3}]
$N_A|_{r'=1}$ Flux through the external surface of the catalyst pellet [mol m_i^{-2} s^{-1}]

For a complete derivation, the reader is referred to the course of Chemical Reactors: Fundamentals and Applications of Guy B. Marin at Ghent University [3]. It is necessary to bear in mind that previous

equations hold for first order irreversible reactions. If it is assumed that the catalyst particle is spherically shaped, following expression is valid for the effectiveness factor:

$$\eta = \frac{1}{\phi}\left(\frac{1}{\tanh(3\phi)} - \frac{1}{3\phi}\right) \tag{5-38}$$

For higher order reactions, a more generalized Thiele modulus can be introduced in case of strong diffusion limitations [3]:

$$\phi = \frac{R_w(C_{A,b})}{a_v(2\int_{C_A|_e}^{C_{A,b}} D_{A,e} R_w dC)^{\frac{1}{2}}} \tag{5-39}$$

Since calculations cannot be performed with previous equations as knowledge about intrinsic kinetics is restricted, the Weisz modulus is introduced:

$$\Phi = \eta\,\phi^2 \tag{5-40}$$

For n^{th} order kinetics, following relationship can then be derived [3]:

$$\Phi = \frac{(n+1)\,\rho_p R_{w,A}^{obs}}{2\,a_v^2\,D_{A,e}\,C_{A,b}} \tag{5-41}$$

This contains only observable parameters. Taking into account that in order to assure the absence of diffusion limitations, the Thiele modulus should be as small as possible and the effectiveness factor should be close to unity. Therefore, following condition is applied to the Weisz modulus:

$$\Phi \ll 1 \tag{5-42}$$

The effective diffusion coefficient used in the calculations is determined taking into account the porosity and tortuosity of the catalyst pellet:

$$D_{A,e} = \frac{\varepsilon_p D_A}{\tau_p} \tag{5-43}$$

With ε_p Porosity of the catalyst pellet [$m_f^3\ m_p^{-3}$]
τ_p Tortuosity of the catalyst pellet [$m^2\ m^{-2}$]

3.2.2 HEAT TRANSPORT

The temperature profile in the catalyst pellet will be estimated via a parabolic expression such that for the center of the catalyst pellet both a maximum and a gradient of zero, for symmetry reasons, is achieved. This parabolic expression can be represented by following equation:

$$T - T_s = \gamma\left(1 - \left[\frac{2r}{d_p}\right]^2\right) \tag{5-44}$$

With r Pellet radius [m]

The constant γ will represent the steepness of the temperature gradient in the pellet and will be negative in the case of an endothermic reaction. The observed specific production rate in the catalyst

pellet needs to be calculated over the entire pellet. The deviation in temperature for the specific production rate is again estimated via a first order Taylor expansion (equation (5-28)):

$$R_{w,A}^{obs} = \frac{\rho_p \int_0^{V_p} R_{w,A} dV}{\rho_p \frac{\pi d_p^3}{6}} = \frac{6}{\pi d_p^3} \int_0^{\frac{d_p}{2}} \left(1 + \frac{E_a \gamma}{R\, T_s^2} \left(1 - \left(\frac{2r}{d_p}\right)^2\right)\right) 4\pi r^2\, dr \tag{5-45}$$

With T_s Temperature at pellet surface [K]

Taking into account the general condition represented by equation (5-1), the condition for internal temperature gradients becomes:

$$\left|\frac{2}{5}\frac{\gamma E_a}{R T_s^2}\right| < 0.05 \tag{5-46}$$

γ is subsequently determined via the heat balance over the catalyst surface at steady state:

$$(-\Delta_r H) R_{w,A}^{obs} \rho_p V_p = -\lambda_p S_p \frac{dT}{dr}\Big|_{r=\frac{d_p}{2}} \tag{5-47}$$

With V_p Volume of catalyst pellet [m_p^3]
S_p Surface of catalyst pellet [m_p^2]
λ_p Heat conduction coefficient of catalyst pellet [W m_p^{-1} K^{-1}]

This results in the final condition for internal temperature gradients:

$$\frac{d_p^2 R_{w,A}^{obs} \rho_p |\Delta_r H|}{\lambda_p T_s} < 3.0 \frac{R T_s}{E_a} \tag{5-48}$$

4 REMARKS FOR CATALYTIC REACTION TESTS

Bearing in mind previous conditions concerning ideal plug flow regime and transport limitations, some critical parameters can be defined by applying a sensitivity analysis:

- Pellet diameter (d_p)
- Molar inlet flow rate (F_0)
- Temperature (T)
- Pressure (P_{tot})
- Catalyst mass (W)

The former two parameters are essential in defining the intrinsic kinetic regime. Increasing the pellet diameter would eventually result in limitations in plug flow behavior due to the increased significance of wall effects. Furthermore, the pellet diameter is also an important parameter in the conditions for internal transport limitations (equations (5-41) and (5-48)). For these reasons, pellets will be synthesized in the range of 250 to 500 µm. The second critical parameter is the molar inlet flow rate as higher flow rates will increase heat and transfer and, as such, reduce temperature and (external) concentration gradients. They will, however, lead to higher pressure drops. According to a sensitivity analysis, reactor inlet flow rates could therefore be varied between 0.15 and 15 mmol/s.

Restrictions on temperature and pressure are rather due to limitations of the set-up or the reaction than due to non-ideal plug flow or transport phenomena. For this reason, these parameters are handled in a more narrow range than intrinsic kinetics will allow. It should be taken into account that the HTK-MI set-up is not able to operate at pressures below atmosphere while too high pressures will most probably result in an increased selectivity to ethyl acetate [9]. Also temperature could result in increases of selectivity to side reactions leading to conditions far from ideal for ethanol dehydrogenation to acetaldehyde. Hence, it goes without saying that a more narrow operating range should be opted. A last factor to be considered is the catalyst mass as this will directly affect the amount of dilution in the catalyst bed. This last parameter will be kept constant during processing as the space time will be varied via the inlet flow rates of ethanol.

In the following chapter, a range of operating conditions is therefore selected to ensure the criteria of the intrinsic kinetics regime. That way, a straightforward analysis of the reaction kinetics is possible for an ideal plug flow reactor in the absence of mass and heat transfer limitations. A presentation of these reaction conditions is listed in Table 5-1.

Table 5-1: Possible operating regime applied in Chapter 6

Operating conditions	
Temperature (K)	533-573
Pressure (MPa)	0.5
Space time (kg_{cat} s mol^{-1})	35-100

5 REFERENCES

[1] R.J. Berger, E.H. Stitt, G.B. Marin, F. Kapteijn, J.A. Moulijn, Eurokin - Chemical reaction kinetics in practice, Cattech, 5 (2001) 30-60.
[2] J. Perez-Ramirez, R.J. Berger, G. Mul, F. Kapteijn, J.A. Moulijn, The six-flow reactor technology - A review on fast catalyst screening and kinetic studies, Catal Today, 60 (2000) 93-109.
[3] G.B. Marin, Chemical Reactors: Fundamentals and Applications, Ghent University, 2015.
[4] G.F. Froment, Fixed Bed Catalytic Reactors - Current Design Status, Ind Eng Chem, 59 (1967) 18-&.
[5] R.J. Berger, J. Perez-Ramirez, F. Kapteijn, J.A. Moulijn, Catalyst performance testing: bed dilution revisited, Chem Eng Sci, 57 (2002) 4921-4932.
[6] D.E. Mears, Diagnostic Criteria for Heat Transport Limitations in Fixed Bed Reactors, J Catal, 20 (1971) 127-&.
[7] A. Sengupta, G. Thodos, Mass and Heat Transfer in the Flow of Fluids through Fixed and Fluidized Beds of Spherical Particles, Aiche J, 8 (1962) 608-610.
[8] J. Deacetis, G. Thodos, Mass and Heat Transfer In ... Flow of Gases through Spherical Packings, Ind Eng Chem, 52 (1960) 1003-1006.
[9] G. Carotenuto, R. Tesser, M. Di Serio, E. Santacesaria, Kinetic study of ethanol dehydrogenation to ethyl acetate promoted by a copper/copper-chromite based catalyst, Catal Today, 203 (2013) 202-210.

Chapter 6: Catalytic Reaction Experiments

1 INTRODUCTION

With the characterization techniques discussed in Chapter 4, insight is obtained in the catalyst properties. Nonetheless, it will require catalytic reaction experiments to fully understand and comprise the performance of the catalysts in the dehydrogenation of bio-ethanol. For this reason, the catalysts synthesized according to the different procedures explained in Chapter 3 are tested on a High Throughput Kinetics Mechanistic Investigation set-up. It was checked via the procedures of Chapter 5 that all experimental results were measured in the intrinsic regime, i.e., absence of heat or mass transfer limitations or complex flow patterns. In a first instance, a comparison will be performed based on the different methods of synthesis and the effect of the regeneration procedure for the formation of the active sites. Consequently attention is paid to the deactivation of the catalysts and their regenerability which allows for the measurement of a kinetic dataset. This can serve as a basis for the regression to a kinetic model. To finalize, the effect of water on the behavior of the catalyst will be examined as the presence of water is unavoidable in the production of bio-ethanol via fermentation and would be energy and time intensive to remove.

2 THERMODYNAMIC EQUILIBRIUM

Before looking at the performance of the catalyst, it is important to stress that a complete conversion of ethanol towards acetaldehyde is thermodynamically unfeasible. Therefore, the thermodynamic equilibrium, corresponding with the dehydrogenation of ethanol to acetaldehyde in the gas phase, is further investigated. The conversion that is reached for this equilibrium will then resemble the maximal conversion that could be achieved.

For an extensive discussion about the method of determination of the chemical equilibrium, the reader is referred to Appendix A. An overview of the equilibrium coefficients along with the conversions at equilibrium for a considered temperature interval of 533 to 573 K is shown in Table 6-1.

Table 6-1: Equilibrium coefficients and conversions at equilibrium for different temperatures

Temperature (K)	K_{eq} (-)	X_{eq} (-)
533	0.460	0.913
553	0.905	0.952
573	1.700	0.973

3 INCORPORATION VS. IMPREGNATION

Characterization of the synthesized catalysts already indicated that the catalyst prepared via coprecipitation has more interesting properties such as a smaller particle size distribution which consequently led to a higher dispersion of the catalyst. The larger clusters of particles formed at the surface of the impregnated catalyst also indicated a limitation in the formation of the PdZn intermetallic compound. Remnants of metallic palladium could as such remain at the surface and affect the selectivity of the reactions in a negative way.

When looking at the deactivation curves of the incorporated and impregnated catalyst, as shown in Figure 6-1, a higher activity after 24 hours of 27.6 % is achieved for the incorporated sample compared to 5.4 % for the impregnated sample. In these deactivation curves, two different rates of deactivation could be observed. At earlier time on streams (TOS), a faster rate is observed while after a certain period of time, deactivation shows a more restricted decreasing behavior. A hypothesis for the first drop in activity could be the deposition of coking on the surface of the catalyst. In order to assign which components could result in the formation of the cokes, a closer look is taken at the selectivity of the catalyst and possible reactions occurring at the surface. Figure 6-2 and Figure 6-3 represent the dependency of the selectivity of the incorporated and impregnated catalyst on the time on stream, distinguishing a region with fast deactivation and lower selectivity to acetaldehyde and a region of slow deactivation with a higher selectivity to acetaldehyde. The latter is further indicated as the stable region.

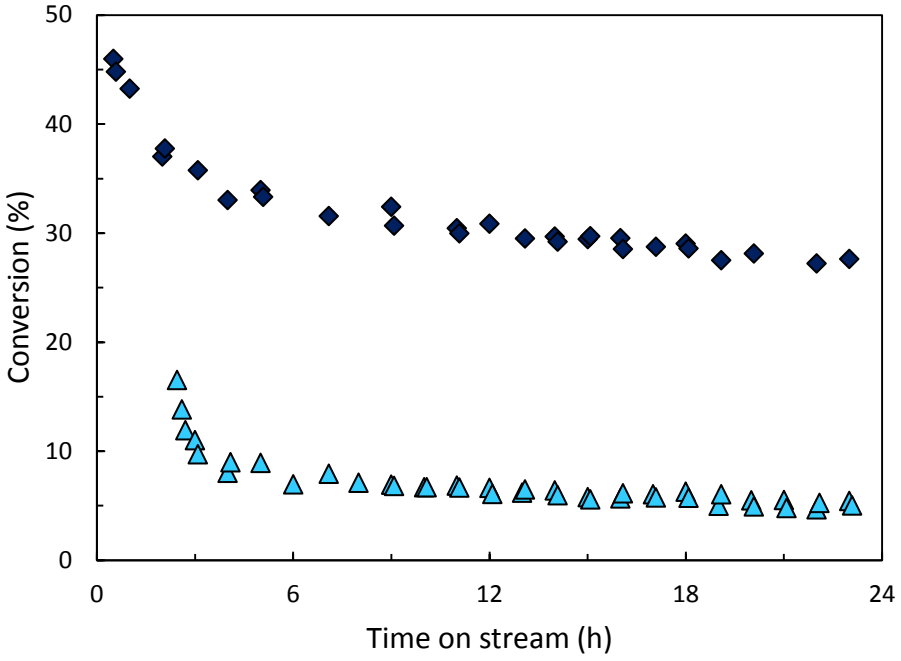

Figure 6-1: Deactivation curves for fresh PdZn/Mg(Al)(Pd)(Zn)O_x (diamonds, dark blue) and PdZn/Mg(Al)O_x (triangles, cyan) with a complete reduction cycle (T = 533 K; p_{EtOH} = 25 kPa, space time = 36 kg_{cat} s mol^{-1})

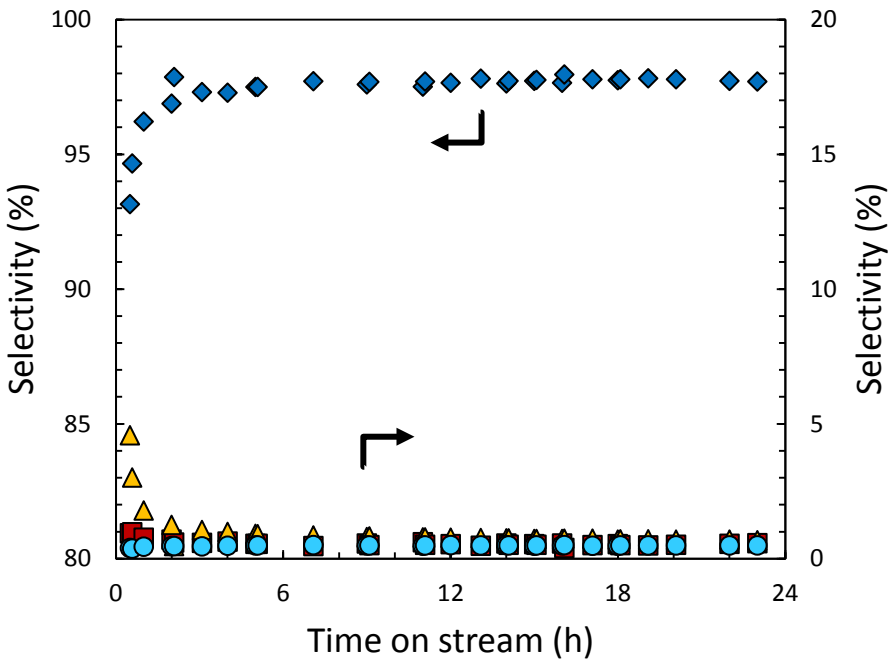

Figure 6-2: Dependency of the selectivity for acetaldehyde (diamonds, blue), methane (squares, red), ethyl acetate (triangles, yellow) and diethyl ether (circles, cyan) on the time on stream for PdZn/Mg(Al)(Pd)(Zn)O_x (T = 533 K; p_{EtOH} = 25 kPa, space time = 36 kg_{cat} s mol^{-1})

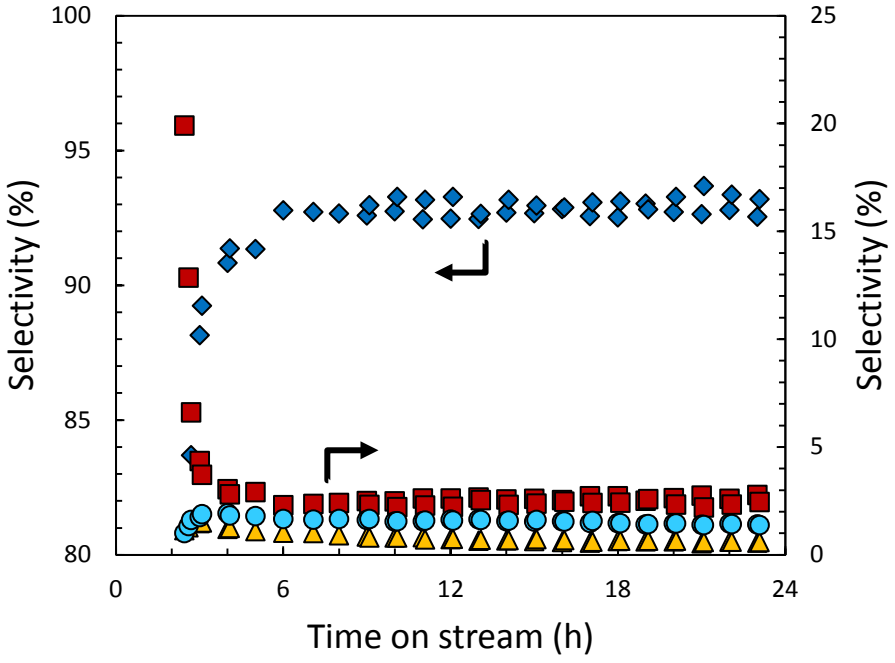

Figure 6-3: Dependency of the selectivity for acetaldehyde (diamonds, blue), methane (squares, red), ethyl acetate (triangles, yellow) and diethyl ether (circles, cyan) on the time on stream for PdZn/Mg(Al)O_x (T = 533 K; p_{EtOH} = 25 kPa, space time = 36 kg_{cat} s mol^{-1})

3.1 COKES FORMATION ON THE CATALYST SURFACE

A true validation of the deposition of cokes at the catalyst surface will require characterization techniques such as XRD and TPO to verify if these compounds are present at the surface. This will be performed in Chapter 7. At first, though, possible reactions that could lead to the formation of cokes are identified. An overview of possible reactions happening at the catalyst surface is represented in Figure 6-4. In a first consideration, reactions that hereby would lead to coke formation are the Boudouard reaction and the decomposition of methane resulting in the formation of carbon graphite [1]:

$$2\,CO \rightleftarrows C + CO_2$$

$$CH_4 \rightleftarrows C + 2\,H_2$$

Though, it could be argued that decomposition of other reaction products also results in coke formation [2]:

$$CH_3CH_2OH \rightarrow cokes$$

$$CH_3CHO \rightarrow cokes$$

$$CH_3COOCH_2CH_3 \rightarrow cokes$$

$$CH_3CH_2OCH_2CH_3 \rightarrow cokes$$

It is much likely that the first two reactions will affect the selectivity towards methane and carbon monoxide. Nonetheless, this effect is considered to be negligible as one could argue that a small formation of cokes already shows considerable decreases in activity of the catalyst.

Overviewing the initial selectivity of both catalysts, it is observed that the impregnated catalyst will show a strong tendency to ethanol decomposition, indicating the remaining presence of metallic palladium sites at the surface. The high formation of methane and carbon monoxide could subsequently favor the formation of cokes. As these will deposit on the active sites of palladium a decrease in methane selectivity is consequently observed, favoring the formation of acetaldehyde with a selectivity of 92.8 %.

Despite the fact that a high selectivity towards methane was observed for the impregnated catalyst, this was not the case for the incorporated one indicating a lower fraction of metallic Pd sites at the surface of the catalyst. However, the initial decrease in activity is still observed, suggesting that only a small fraction of metallic Pd, not observable via XRD, already could result in the formation of cokes resulting in the initial deactivation. As these metallic Pd sites are possibly located between the PdZn sites, e.g., as a lattice defect, it is more likely that coke will deposit on the PdZn active sites resulting in a less dense coverage. That way, the selectivity to ethyl acetate will weakly decrease, favoring the formation of acetaldehyde. The finally obtained selectivity will then reach values of 97.6 %, confirming the higher catalytic performance of the incorporated catalyst.

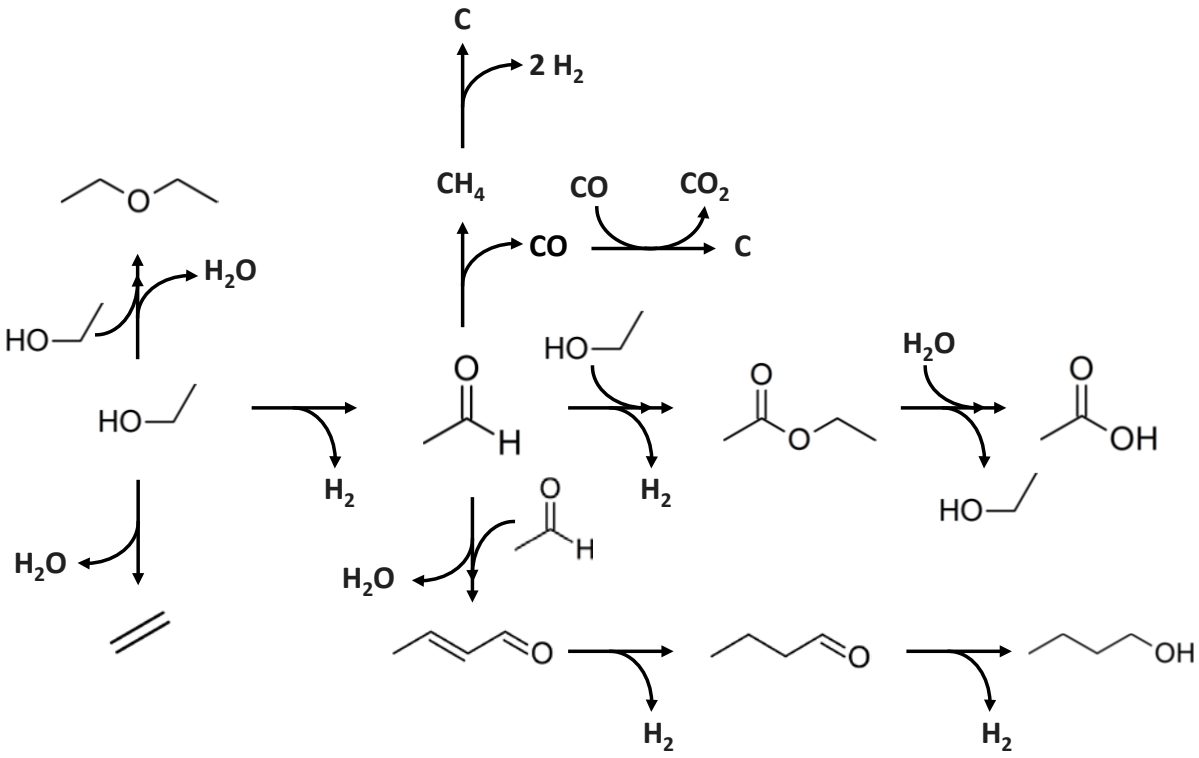

Figure 6-4: Possible reactions occurring at the catalyst surface [3]

3.2 Contribution of the Mixed Oxide Support

The formation of diethyl ether during the experiments cannot be assigned to the reactions catalyzed by the active sites of neither PdZn nor Pd. As this formation will require acid sites it is more likely that the reaction occurs at the carrier of the metal sites than on the metal sites themselves. The alumina sites of the hydrotalcite precursor are strong Lewis acids giving rise to acid sites on the support and thus catalysis to diethyl ether. Nonetheless, hydrotalcite-based mixed oxides are generally known as basic supports, containing only a small fraction of acid sites. Due to the excess of ZnO used in the synthesis of the catalysts, it is possible that some remnants of the ZnO are present in the bulk of the support that was too stable to be reduced. As ZnO is often used in the synthesis of methanol to decrease the selectivity towards dimethyl ether, it decreases the acidity of the alumina sites. It is hence likely that it will also suppress the formation of diethyl ether [4, 5]. The impregnated catalyst will not contain ZnO in its support structure but less distributed on its surface, indicating the reason for the higher selectivity to diethyl ether. It, however, requires consideration that also other phenomena could play a role such as a higher surface area and thus availability of the support.

3.3 The Stable Region

The second region that could be distinguished besides the fast deactivation region starts for both catalysts between approximately 5 and 10 hours of time on stream. This deactivation, which has a more linearly developing behavior, could be assigned to sintering of the intermetallic particles. As

this sintering is a very slow process, deactivation rates are also of a few orders of magnitude lower than the deactivation in the first region. Confirmation on this sintering, though, needs to be provided by characterization, performed in Chapter 7.

4 EFFECT OF THE REDUCTION PROCEDURE

In Chapter 4 on characterization of the different catalysts, it was yet reported that the reduction procedure can have a significant effect on the catalyst structure. The number of reduction cycles points out to be largely affecting the uniformity of the PdZn sites at the catalyst surface and hence the particle size distribution. As the average particle size but also its variance are preferably as small as possible for a high dispersion and uniformity of the surface, one is therefore inclined to opt for a complete reduction procedure. Validation by means of reaction experiments, though, is appropriate.

4.1 ON THE INCORPORATED CATALYST

Figure 6-5 shows the deactivation curves of fresh incorporated catalysts, either activated via a complete or a short reduction procedure. According to these curves, it could be observed that the conversion after 24 hours obtained for the catalyst prepared via a complete reduction procedure is remarkably higher, i.e., 27.6 % versus 5.6 %, than for the one with the shorter cycle. Partially, this could be explained by the smaller average particle sizes of the PdZn particles on the catalyst surface. Nonetheless, values of dispersion, calculated from this particle size showed the highest average values for the catalyst prepared via a short reduction cycle. It, however, requires consideration that the variation on this dispersion was quite high in comparison to the other one.

Based on these results of conversion, there is no doubt that based on fresh catalysts the complete reduction cycle is the superior regeneration procedure of the two. If one looks at the selectivity, represented by Figure 6-2 and Figure 6-6, this superiority is confirmed. The selectivity of the catalyst regenerated via the short cycle will have a selectivity of 96.7 % while complete reduction cycles as regeneration are able to reach a selectivity of 97.6 %. This is assigned to the higher uniformity of the catalyst surface that is possible to be obtained (Figure 4-7, Chapter 4). Upon increasing the number of oxidation-reduction cycles, a more stable intermetallic compound will be formed, thus causing a lower fraction of metallic Pd sites at the surface.

This is represented by the effect on the deactivation curves of cokes deposition on the surface of the catalysts. Figure 6-6 showed an initially higher selectivity towards methane for the catalyst prepared via a short reduction cycle, indicating a remaining presence of metallic palladium on the catalyst surface. Subsequent coking would cover these sites which will then result in an increased selectivity to acetaldehyde.

The selectivity to ethyl acetate is rather low and could be assigned to the lower yield of acetaldehyde in comparison to the catalyst regenerated with a complete reduction cycle as acetaldehyde is required to remain on the surface or re-adsorb to convert to ethyl acetate. The higher selectivity towards diethyl ether is a result of more acidic sites available for reaction.

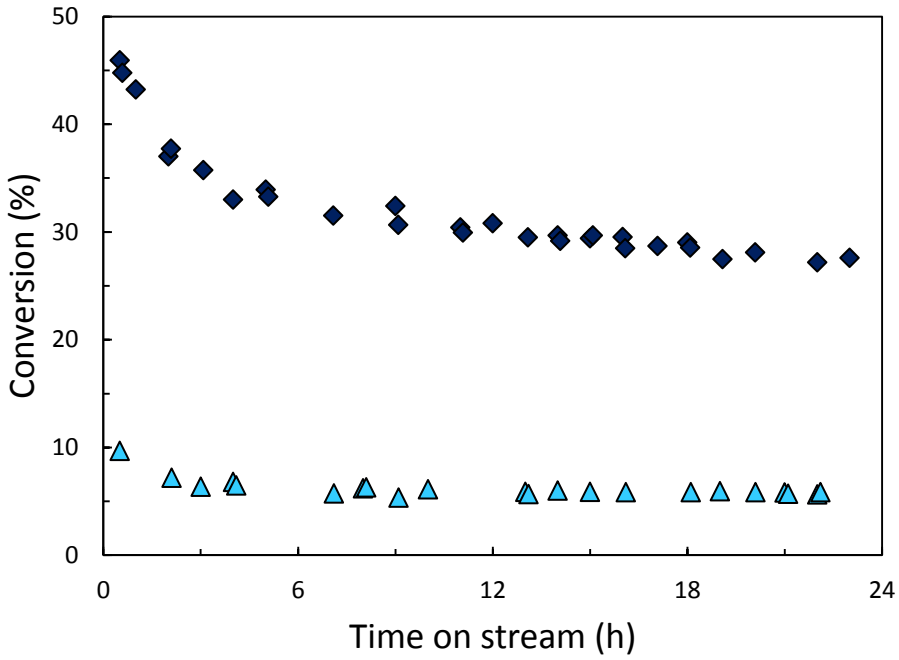

Figure 6-5: Deactivation curves for fresh PdZn/Mg(Al)(Pd)(Zn)O_x for a complete (diamonds, dark blue) and short (triangles, cyan) reduction cycle (T = 533 K; p_{EtOH} = 25 kPa, space time = 36 kg_{cat} s mol^{-1})

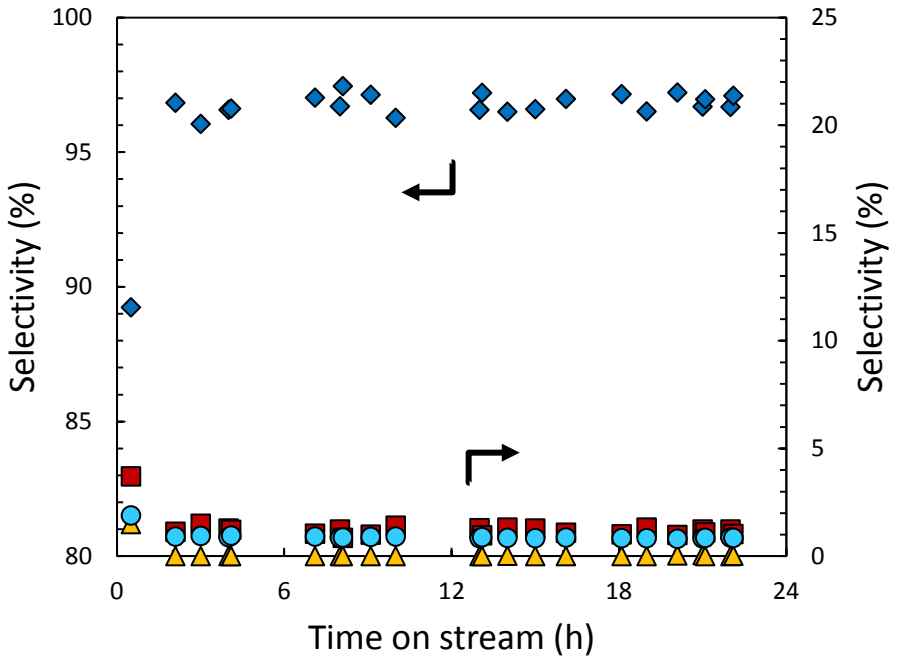

Figure 6-6: Dependency of the selectivity for acetaldehyde (diamonds, blue), methane (squares, red), ethyl acetate (triangles, yellow) and diethyl ether (circles, cyan) on the time on stream for PdZn/Mg(Al)(Pd)(Zn)O_x with a short reduction cycle (T = 533 K; p_{EtOH} = 25 kPa, space time = 36 kg_{cat} s mol^{-1})

4.2 ON THE IMPREGNATED CATALYST

The deactivation curves of the impregnated catalysts, regenerated by both a short as a complete procedure are illustrated in Figure 6-7. That way, it could be observed that for both procedures approximately the same conversions are reached after a certain period of time, i.e., 6 hours. The amount of deactivation in the first hours, though, is much higher for the catalyst regenerated via a complete reduction cycle. Looking at the selectivity as a function of the time on stream for both catalysts, shown in Figure 6-3 and Figure 6-8, also illustrates the low initial selectivity to acetaldehyde for both catalysts. Though, while the catalyst regenerated via a complete reduction cycle shows only a high initial selectivity to methane, i.e., 19.9 %, the catalyst regenerated via a short reduction cycle shows a high initial selectivity for both methane and ethyl acetate, i.e., 3.7 and 3.0 %, respectively. The lower selectivity towards methane can also be derived from the lower activity decrease, assigned to coking, observed in the deactivation curves, i.e., 2.7 % and 0.7 % per hour for a complete and short cycle, respectively.

The alteration between oxidation and reduction cycles thus has no beneficial effect for the impregnated catalyst. In order to find an explanation for these results, it is worth considering the particle size distributions of the PdZn particles in Chapter 4, represented by Figure 4-8. In these distributions, one can clearly distinguish 2 separate distributions at 5.5 and 11 nm for the catalyst after a short reduction cycle while the one with the complete cycle shows only one maximum at 7 nm. The difference between both procedures will lie in the redistribution of the PdO and ZnO over the catalyst surface in between the reduction cycles. This will result in a more uniform diameter as is shown by the distributions. A possible hypothesis, though, is that when the reduction again takes place, less Zn is facilitated to reduce, creating a larger, though in comparison to PdZn small, fraction of metallic Pd. This will consequently result in a higher selectivity towards methane. The reason why this is not occurring for the incorporated catalyst could be assigned to the higher compatibility with the oxide support as PdO and ZnO were coming from the structure, making their redistribution across the surface easier.

After the region in which cokes deposition is a prominent factor, the selectivity of acetaldehyde will move towards a stable value of 95.7 % for the catalyst with the short reduction cycle which is considerably higher than the one with a complete cycle which only reaches values up to 92.8 %. Bearing in mind the remaining selectivity towards methane, i.e., 2.5%, a larger fraction of uncovered metallic Pd could be considered for this catalyst, even after cokes deposition. Nevertheless, also the selectivity for diethyl ether will be higher for the catalyst with a complete reduction cycle, indicating a higher availability of acid sites on the support available for reaction.

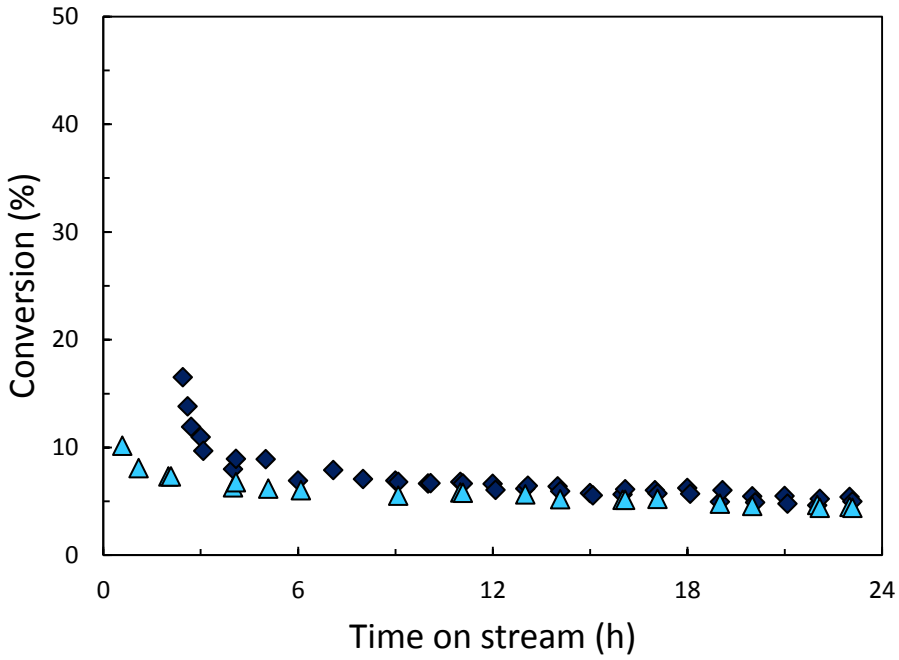

Figure 6-7: Deactivation curves for fresh PdZn/Mg(Al)Ox for a complete (diamonds, dark blue) and short (triangles, cyan) reduction cycle (T = 533 K; p_{EtOH} = 25 kPa, space time = 36 kg_{cat} s mol^{-1})

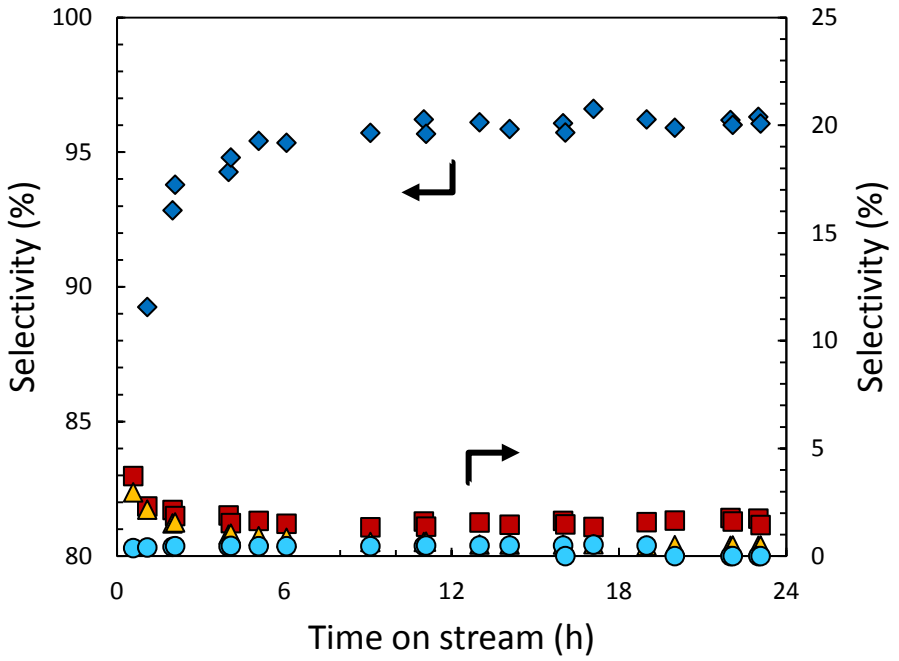

Figure 6-8: Dependency of the selectivity for acetaldehyde (diamonds, blue), methane (squares, red), ethyl acetate (triangles, yellow) and diethyl ether (circles, cyan) on the time on stream for PdZn/Mg(Al)O_x with a short reduction cycle (T = 533 K; p_{EtOH} = 25 kPa, space time = 36 kg_{cat} s mol^{-1})

5 REPRODUCIBILITY OF CATALYSIS

After introduction of the different catalysts used in this study, a more in-depth analysis will be performed based on the reproducibility of these catalysts. As the final goal is to obtain a model-derived catalyst design through adequate experimental observation, it is necessary to consider the reproducibility. If a catalyst does not show this ability, it will not be possible to regenerate the same catalyst for further observation. Every individual data point hence will require the loading of a new catalyst in the reactor. For this reason, deactivation curves of different regenerations will be measured of all overviewed catalysts, in order to give an indication on their reproducibility.

5.1 ON THE INCORPORATED CATALYST

Figure 6-7 already indicated the superiority of the catalyst regenerated via a complete reduction cycle due to the higher conversion and selectivity to acetaldehyde that was obtained. However, if this catalyst showed to be inadequately reproducible, its value for experimental measurements or industrial operation would drop due to the excessive amount of time that would be required for unloading and loading of new catalyst. Therefore, it is worth considering the catalysts prepared via both procedures.

The deactivation curves for a fresh catalyst and two regenerations with a short cycle are represented by Figure 6-9. According to these curves, the lack of reproducibility of the catalysts is immediately clear as the conversion in the stable region will increase per regeneration, i.e., from 5.6 % to 14.3 % until 22.1 %. If one, hereby, looks at the dependency of the selectivity to acetaldehyde and side products, it can be observed that the selectivity to acetaldehyde and ethyl acetate will increase while the ones to methane and diethyl ether will drop. A more clear understanding of these observations could be obtained by redirecting again to the deactivation curve of the incorporated catalyst with a complete reduction cycle, shown in Figure 6-5. That way, it could be observed that both conversion and the selectivity to the different products are evolving towards similar orders of magnitude as for the complete reduction cycle. As such, this creates the suggestion that a similar mechanism will occur as one performs a complete reduction cycle, though, reaction will happen in between the cycles. So, every new regeneration a narrower particle size distribution and thus more uniform surface area is obtained which will benefit the activity and selectivity of the catalysts. The reason why the catalyst is not at the same level after 2 regenerations as the one with a complete reduction cycle could possibly be assigned to sintering that is happening during reaction, causing a shift to higher particle sizes and hence lower dispersions. This, however, requires confirmation by TEM measurements and will be performed in Chapter 7.

Looking at the deactivation curves for an incorporated catalyst with a complete reduction cycle for a number of regenerations, reproducibility is achieved, as is illustrated in Figure 6-11. This will also confirm the hypothesis defined for a short reduction cycle as here it is observed that a further improvement on the activity of the catalyst by increasing the number of reduction cycles is very small. The regeneration cycle could therefore be considered sufficient to counter possible coking and sintering that is occurring on the catalyst surface but will not further improve the particle size

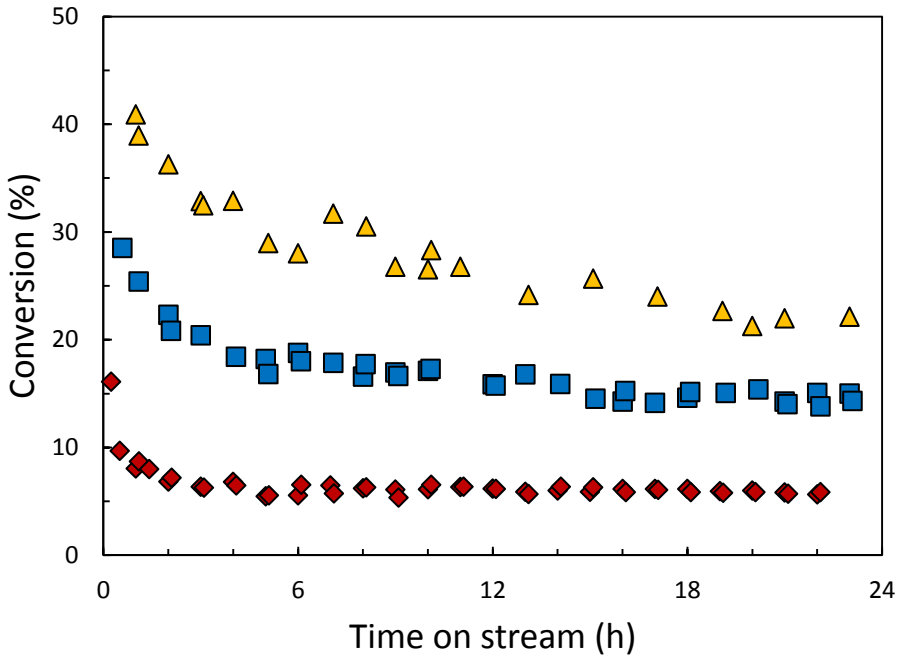

Figure 6-9: Deactivation curve for PdZn/Mg(Al)(Pd)(Zn)O_x with a short reduction cycle, fresh (diamonds, red), 1st regeneration (squares, blue) and 2nd regeneration (triangles, yellow) (T = 533 K; p_{EtOH} = 25 kPa, space time = 36 kg_{cat} s mol^{-1})

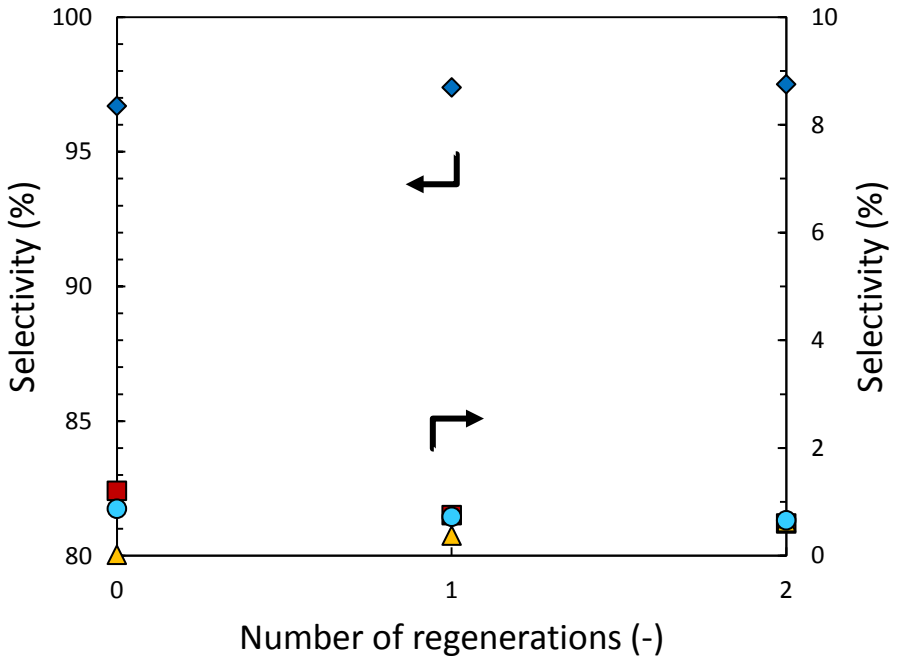

Figure 6-10: Dependency of the selectivity to acetaldehyde (diamonds, blue), methane (squares, red), ethyl acetate (triangles, yellow) and diethyl ether (circles, cyan) on the number of regenerations for PdZn/Mg(Al)(Pd)(Zn)O_x with a short reduction cycle (T = 533 K; p_{EtOH} = 25 kPa, space time = 36 kg_{cat} s mol^{-1})

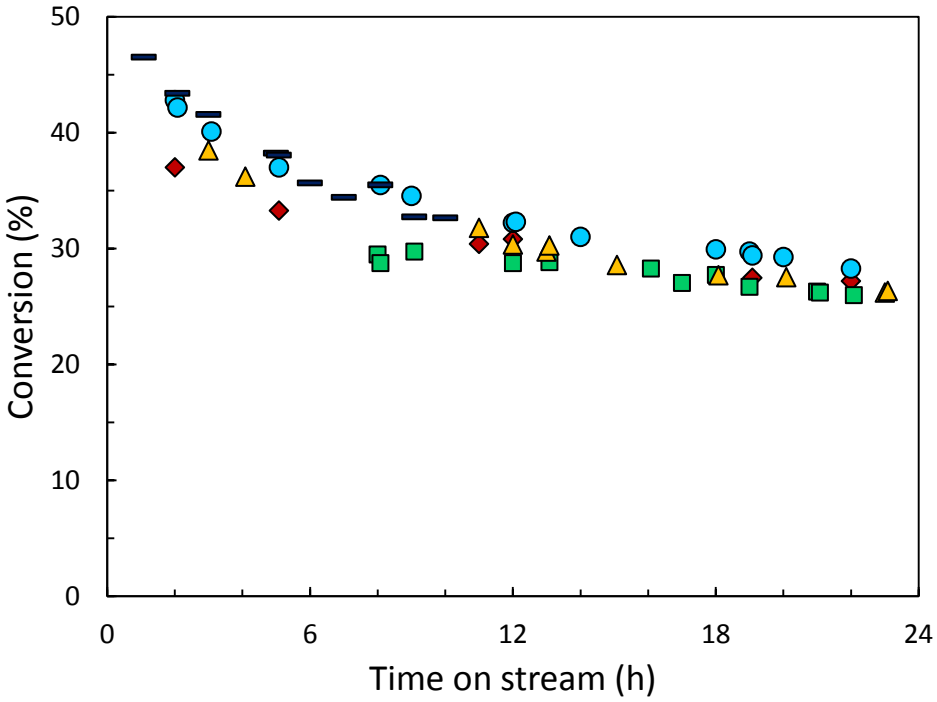

Figure 6-11: Deactivation curve for PdZn/Mg(Al)(Pd)(Zn)O_x with a complete reduction cycle, fresh (diamonds, red), 1st regeneration (squares, green), 2nd regeneration (triangles, yellow), 3rd regeneration (circles, cyan) and 4th regeneration (stripes, dark blue) (T = 533 K; p_{EtOH} = 25 kPa, space time = 36 kg_{cat} s mol^{-1})

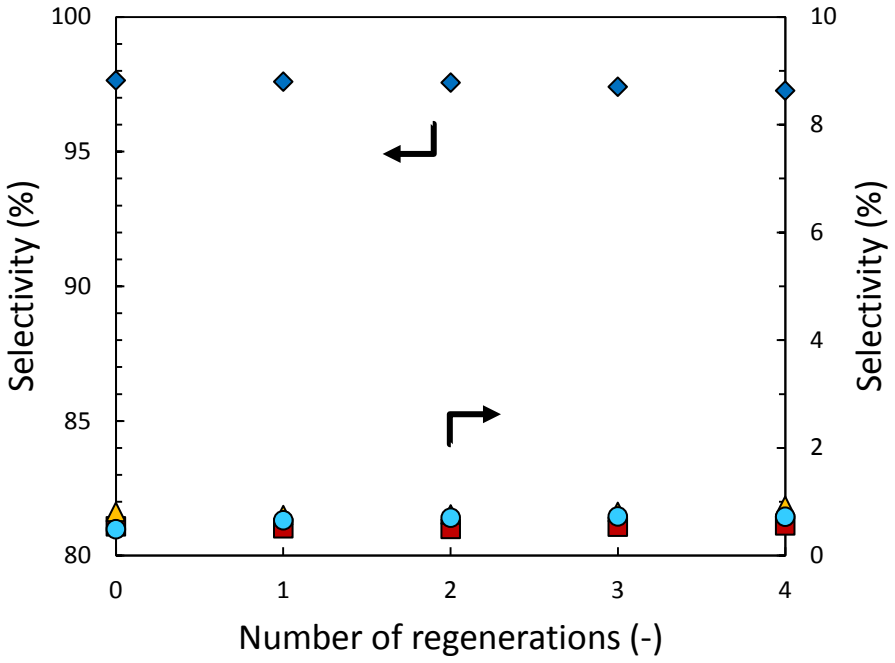

Figure 6-12: Dependency of the selectivity to acetaldehyde (diamonds, blue), methane (squares, red), ethyl acetate (triangles, yellow) and diethyl ether (circles, cyan) on the number of regenerations for PdZn/Mg(Al)(Pd)(Zn)O_x with a complete reduction cycle (T = 533 K; p_{EtOH} = 25 kPa, space time = 36 kg_{cat} s mol^{-1})

distribution as was the case for a short reduction cycle. The eventual effect of reaction and regeneration on the surface area, though, needs to be confirmed by characterization (Chapter 7).

The dependency of the selectivity on the number of regenerations for the catalyst with a complete reduction cycle is shown in Figure 6-12. As such, it could be illustrated that the selectivity to acetaldehyde is barely changing upon regeneration with a small drop of 0.3 % after 4 regenerations. The highest increase in selectivity to side products could hereby be measured for diethyl ether, i.e., 0.5 % to 0.7 %, which could possibly be assigned to a change in the mixed oxide support upon multiple regenerations, leading to a higher availability of acid sites.

According to previous measurements, the superiority of the incorporated catalyst with a complete reduction cycle could be confirmed as it maintains its activity and selectivity after several regenerations. The reduction procedure, though, did not show better results for the impregnated catalysts, indicating the necessity of a more thorough investigation on the deactivation for several regenerations.

5.2 ON THE IMPREGNATED CATALYST

Figure 6-13 illustrates the deactivation curve for the impregnated catalyst regenerated via short reduction cycles for a number of regenerations. A similar effect as for the incorporated catalyst with short reduction cycles could be initially observed as the activity will increase after a first regeneration. Though, for the second regeneration a lower activity will be measured. As the impregnated catalyst with a complete reduction cycle only shows limited activity, the possibility that the one with the short cycle will approach this behavior is rather unlikely. Other phenomena occurring on the surface will thus be responsible for these observations.

It was recently brought to attention that the catalyst with the short reduction cycle showed two different maxima in its PdZn particle size distribution in contrast to the one maximum with a complete reduction cycle. A possible hypothesis could be that during reaction, sintering would result in a distribution around one maximum. Subsequent oxidation and reduction would than narrow this distribution, leading to a higher activity of the catalyst. As the activity is higher than for the impregnated catalyst, the average particle size is probably lower. This could also prove the previously mentioned assumption that redistribution is less ideal for the impregnated catalyst, leading to higher particle sizes for the number of regenerations. The reason that the activity after the second regeneration is then again lower could be assigned to the fact that for the impregnated catalyst, the optimal number of regeneration cycles is already reached. Another possibility would be sintering that is occurring during reaction, shifting the particle sizes to higher values. This cannot be countered by a narrower particle size distribution as was the case for the incorporated catalyst as the ability of redistribution is lower for the impregnated catalyst. When observing the selectivity to acetaldehyde, shown in Figure 6-14, a similar trend as for the conversion is observed as the selectivity will increase with conversion. With values around 96 % they remain below the ones of the incorporated catalyst.

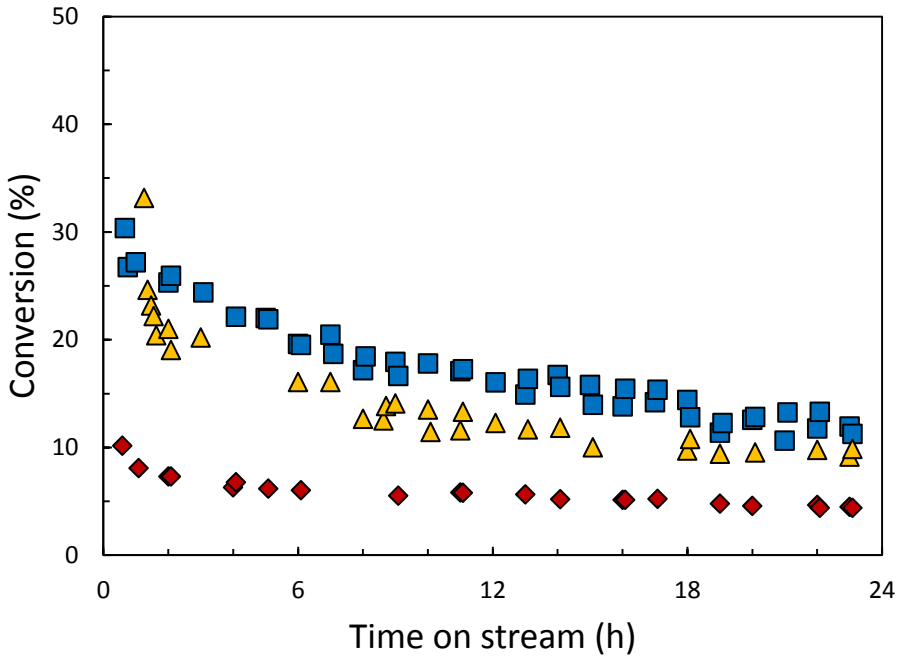

Figure 6-13: Deactivation curve for PdZn/Mg(Al)O_x with a short reduction cycle, fresh (diamonds, red), 1st regeneration (squares, blue) and 2nd regeneration (triangles, yellow) (T = 533 K; p_{EtOH} = 25 kPa, space time = 36 kg_{cat} s mol^{-1})

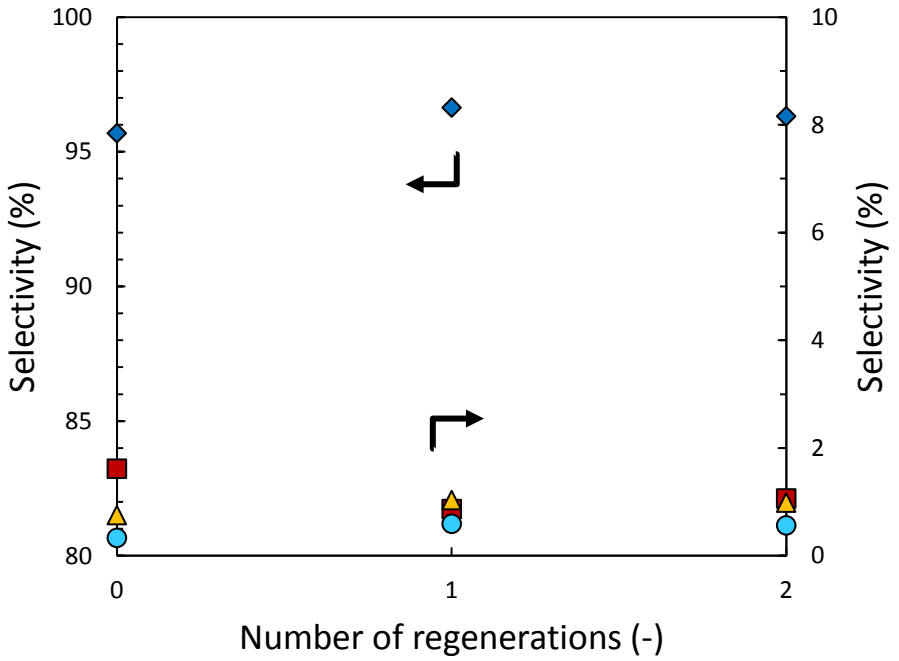

Figure 6-14: Dependency of the selectivity to acetaldehyde (diamonds, blue), methane (squares, red), ethyl acetate (triangles, yellow) and diethyl ether (circles, cyan) on the number of regenerations for PdZn/Mg(Al)O_x with a short reduction cycle (T = 533 K; p_{EtOH} = 25 kPa, space time = 36 kg_{cat} s mol^{-1})

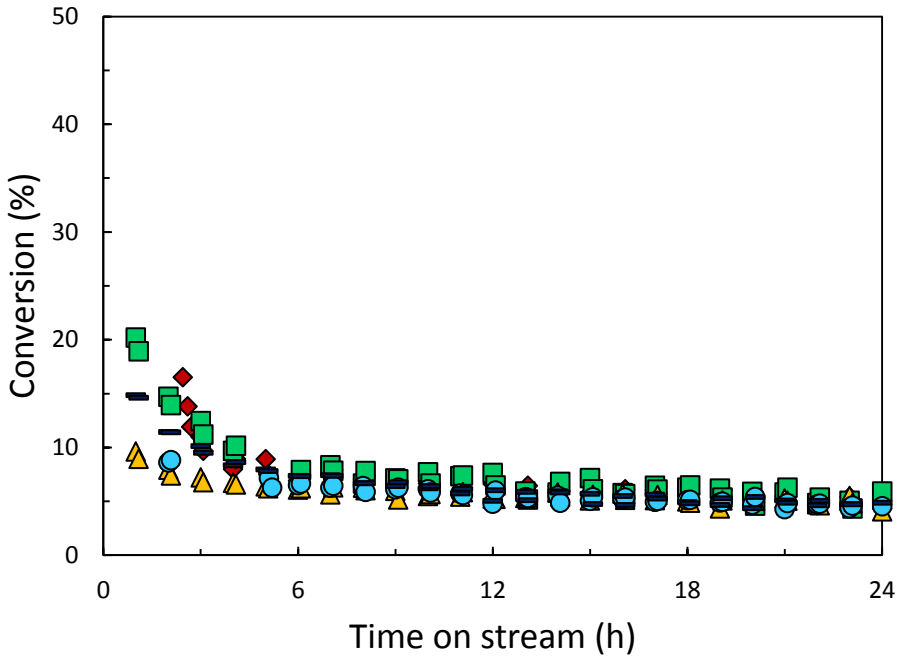

Figure 6-15: Deactivation curve for PdZn/Mg(Al)O_x with a complete reduction cycle, fresh (diamonds, red), 1st regeneration (squares, green), 2nd regeneration (triangles, yellow), 3rd regeneration (circles, cyan) and 4th regeneration (stripes, dark blue) (T = 533 K; p_{EtOH} = 25 kPa, space time = 36 kg_{cat} s mol^{-1})

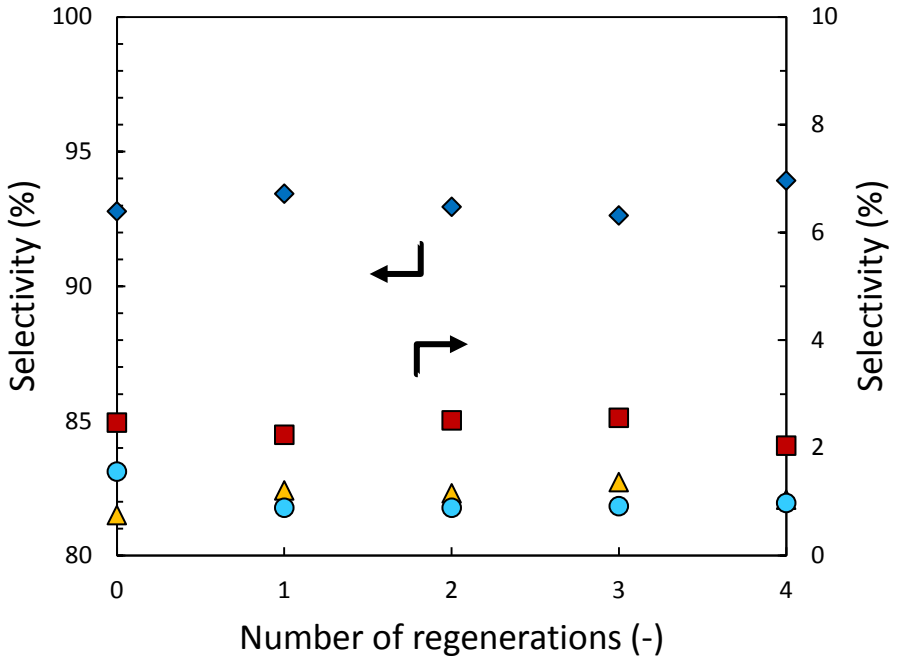

Figure 6-16: Dependency of the selectivity to acetaldehyde (diamonds, blue), methane (squares, red), ethyl acetate (triangles, yellow) and diethyl ether (circles, cyan) on the number of regenerations for PdZn/Mg(Al)O_x with a complete reduction cycle (T = 533 K; p_{EtOH} = 25 kPa, space time = 36 kg_{cat} s mol^{-1})

A complete reduction cycle does show the ability of reproduction upon regeneration as could be observed in Figure 6-15. The regeneration procedure, overviewing both the impregnated and incorporated catalyst, therefore could be considered as sufficient to regenerate the catalyst adequately. Nonetheless, only limited activity is measured for the impregnated catalyst as the procedure will most probably be able to compensate for surface effects such as coking or sintering but will not further narrow the particle size distributions. The reason why the activity is lower than for the incorporated catalyst is hence a result of the lower compatibility with the surface limiting the minimum particle size at higher values. This will also affect the reduction whereby a higher fraction of metallic Pd will be formed, indicated by higher values of methane selectivity, e.g., 2.0 % after the forth regeneration. The dependency of the selectivity on the number of regenerations is shown in Figure 6-16.

Previous observations would therefore suggest applying a complete reduction cycle in order to ensure the reproducibility of the catalyst. As the conversion and selectivity remain at approximately the same values, the incorporated catalyst still shows superior performance over the impregnated one, showing its suitability for further investigation.

6 THE PRESENCE OF WATER DURING ETHANOL PROCESSING

6.1 TRANSITION TO WATER CONTAINING FEEDSTOCK

The incorporated catalyst regenerated via a complete reduction cycle is subsequently selected as the catalyst of choice for further experimental observation. Previous experiments all applied a 100 % ethanol feedstock during reaction, though, in industrial operation, bio-ethanol will always contain a certain percentage of water. Therefore, the effect of water will be investigated in this section. A catalyst situated in its stable region is, after a run time of 24 hours on pure ethanol as feedstock, subjected to a mixture of ethanol/water with a weight ratio of 96/4 at a constant space time and partial pressure of ethanol. The weight ratio will correspond to the azeotropic composition of the ethanol-water mixture.

The dependency of the selectivity on the transition to an ethanol/water feedstock is shown in Figure 6-17. That way, it could be observed that after the change in feedstock, a significant drop, i.e., 97.8 % to 68.8 % in selectivity towards acetaldehyde is measured in favor of the formation of methane, i.e., 0.5 % to 15.3 % increase in selectivity. Initially, also a small increase is observed towards ethyl acetate and diethyl ether, though, this is rather assigned to measurement errors due to the drop in selectivity to acetaldehyde. Observations on the change of conversion with the time on stream indicated no effect of a change of feedstock, thus suggesting that the presence of water will not result in an additional formation of methane but rather in a shift of the dehydrogenation of ethanol to other reactions such as decomposition.

Due to the presence of water, one would expect that reactions corresponding to the steam reforming of ethanol would take place:

$$CH_3CH_2OH + 3\,H_2O \rightleftarrows 2\,CO_2 + 6\,H_2$$

This reaction contains the water gas shift, resulting in a higher formation of hydrogen. It, however, has to be considered that the steam reforming of ethanol generally is performed at temperatures of 623 to 1073 K and water/ethanol ratios of 3:1 or more [6]. As these conditions are far from the ones applied in this work, it is hard to assume that the reaction above will take place. Several reactions pathways were proposed for the ethanol steam reforming, for which one will proceed via the decomposition of ethanol and a consequent water gas shift [7]:

$$CH_3CH_2OH + H_2O \rightleftarrows CH_4 + CO + H_2 + H_2O \rightleftarrows CH_4 + CO_2 + 2H_2$$

The water gas shift will, that way, result in the removal of carbon monoxide which could enhance the formation of methane as observed in Figure 6-17. This, however, remains a hypothesis as a confirmation cannot be obtained with current analysis equipment. Another possibility that could be occurring at the surface is the reaction of cokes with the steam [8]:

$$C + H_2O \rightleftarrows CO + H_2$$

$$2C + 2\,H_2O \rightleftarrows CO_2 + CH_4$$

Hereby, methane will not only be a product of reaction of cokes with steam but the removal of cokes will also result in uncovering the metallic Pd sites which will, that way, result in a higher selectivity to ethanol decomposition. As these reactions are highly exothermic, the creation of hot spots on the catalyst surface could further enhance the decomposition of ethanol.

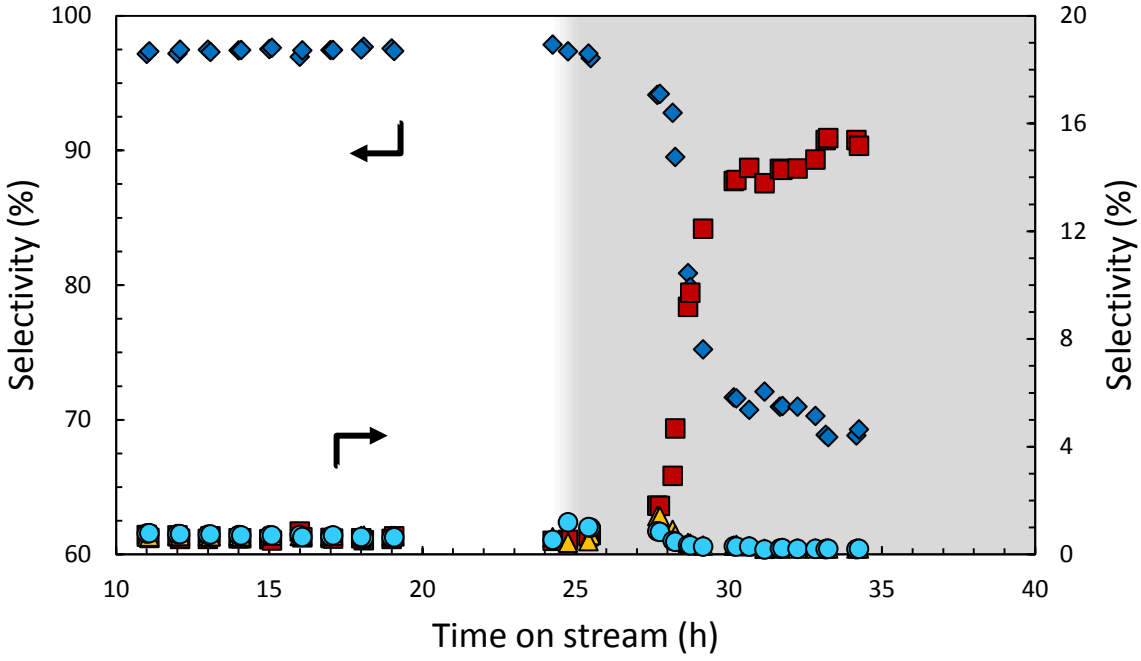

Figure 6-17: Dependency of the selectivity for acetaldehyde (diamonds, blue), methane (squares, red), ethyl acetate (triangles, yellow) and diethyl ether (circles, cyan) during the transition of ethanol feedstock (white area) to an ethanol/water feedstock (grey area) (ethanol/water: 90/10, temperature: 533 K, pressure: 5 barg, space time: 36.1 kg_{cat} s mol^{-1})

6.2 REGENERATION OF THE CATALYST

After reaction with an ethanol/water mixture as feedstock, the catalyst is subjected to a regeneration cycle and subsequently to a reaction cycle with pure ethanol. The initial activity which is in normal operation observed, though, is not reached as conversion starts at a value of 14.5 % with the selectivity to acetaldehyde of 47.2 %. The selectivity to methane, on the contrary, reaches values up to 26.4 %. As the feedstock applied is pure ethanol, it could therefore be considered that a higher fraction of metallic Pd will be present on the catalyst after reaction of water and regeneration. A possible argument for this phenomenon could be that water will affect the mixed oxide support by means of the memory effect. During recreation of the mixed oxide structure upon regeneration, a lower compatibility will be present for PdO and ZnO with the support, impeding the redistribution and thus the formation of the PdZn intermetallic compound. Nonetheless, further characterization will be required on the used catalyst in order to validate the hypothesis and to understand the phenomena occurring at the surface.

7 CONCLUSIONS

The catalytic reaction experiments were carried out on a High Throughput Kinetics Mechanistic Investigation set-up. Two different types of synthesis, i.e., incorporation and impregnation, were evaluated, along with two ways of regeneration, i.e., a short and complete cycle. The incorporated catalyst, regenerated via a complete reduction cycle, points out to have the superior properties, outperforming the other catalysts both in conversion as in selectivity. After 24 hours of operation, ethanol conversion still reaches 27.6 % with a selectivity of 97.6 % to acetaldehyde.

Deactivation curves show that a complete reduction cycle is required to obtain a catalyst that is reproducible and hence more suitable for kinetic experiments. Due to its higher activity, the incorporated catalyst is therefore considered the catalyst of choice. Deactivation, though, is measured for all catalyst and could be contributed to different phenomena such as cokes deposition or possible sintering of the PdZn particles. Further characterization is therefore appropriate and this will be performed in Chapter 7.

The effect of water is evaluated at the azeotropic composition of the ethanol/water mixture and points out a significant increase in selectivity towards methane, rising from approx. 0.5 % to 15.3 %. Possible hypotheses for the increased formation of methane in the presence of water could be assigned to an increase of decomposition of ethanol due to the water gas shift or due to the removal of cokes deposition on the surface. Furthermore, it is observed that water will affect the regenerability of the catalyst, which possibly could be assigned to an impeded formation of PdZn upon regeneration. A more in-depth analysis with different contents of water is, however, required along with a better analysis of the reaction products. In order to evaluate the effect of water on the support, also additional characterization will be necessary.

8 REFERENCES

[1] P.D. Vaidya, A.E. Rodrigues, Insight into steam reforming of ethanol to produce hydrogen for fuel cells, Chem Eng J, 117 (2006) 39-49.
[2] H. Wang, Y. Liu, L. Wang, Y.N. Qin, Study on the carbon deposition in steam reforming of ethanol over Co/CeO(2) catalyst, Chem Eng J, 145 (2008) 25-31.
[3] G. Carotenuto, R. Tesser, M. Di Serio, E. Santacesaria, Kinetic study of ethanol dehydrogenation to ethyl acetate promoted by a copper/copper-chromite based catalyst, Catal Today, 203 (2013) 202-210.
[4] M.S. Spencer, The role of zinc oxide in Cu ZnO catalysts for methanol synthesis and the water-gas shift reaction, Top Catal, 8 (1999) 259-266.
[5] M. Saito, T. Fujitani, M. Takeuchi, T. Watanabe, Development of copper/zinc oxide-based multicomponent catalysts for methanol synthesis from carbon dioxide and hydrogen, Appl Catal a-Gen, 138 (1996) 311-318.
[6] A. Haryanto, S. Fernando, N. Murali, S. Adhikari, Current status of hydrogen production techniques by steam reforming of ethanol: A review, Energ Fuel, 19 (2005) 2098-2106.
[7] A.N. Fatsikostas, X.E. Verykios, Reaction network of steam reforming of ethanol over Ni-based catalysts, J Catal, 225 (2004) 439-452.
[8] J.G. Xu, G.F. Froment, Methane Steam Reforming, Methanation and Water-Gas Shift .1. Intrinsic Kinetics, Aiche J, 35 (1989) 88-96.

Chapter 7: Characterization after Reaction

1 INTRODUCTION

In Chapter 4, first insights are provided into the catalytic properties such as the structure and composition. Catalytic reaction experiments in Chapter 6 aided this analysis by linking this with properties such as activity and selectivity, though, different phenomena were observed affecting these catalytic properties. In order to derive a fundamental understanding on the phenomena during reaction, further characterization is required on the used catalysts. As such, information could be obtained on possible links between the synthesis and preparation of the catalyst on the one side and deactivation of the catalyst on the other side. That way, these results could contribute to strategies applied in future catalyst design. The catalysts, examined in this section, underwent different regeneration-reaction cycles and correspond with the used catalysts of the deactivation curves from Section 5 in Chapter 6:

- PdZn/Mg(Al)(Pd)(Zn)O_x (short): underwent 3 cycles
- PdZn/Mg(Al)(Pd)(Zn)O_x (complete): underwent 5 cycles
- PdZn/Mg(Al)O_x (short): underwent 3 cycles
- PdZn/Mg(Al)O_x (complete): underwent 5 cycles

In a first instance, possible deactivation phenomena are discussed such as cokes formation or sintering of the PdZn particles. Furthermore, the change of the support will be evaluated and possible consequences for reaction. At last, the different crystallographic phases on the used catalysts are examined along with their stability upon oxidation with TPO-XRD as characterization technique.

2 COKES FORMATION ON THE SURFACE

During unloading and loading of the catalyst in the reactor in between two experiments, cokes formation was visually observed on the catalyst surface and the reactor wall. The coke deposition on the surface of the catalyst could, as such, result in a deactivation due to coverage of the active sites. The possible sources of cokes were discussed in Chapter 6, the confirmation of their formation, though, will be shown below. Therefore, the catalysts after reaction are subjected to a temperature programmed oxidation with a constant temperature ramp of 5 K per minute. The effluent is consequently sent to a mass spectrometer that measures the gases formed during oxidation. Following reactions are expected to occur:

$$C + \frac{1}{2}\, O_2 \;\longrightarrow CO$$

$$CO + \frac{1}{2} O_2 \longrightarrow\; CO_2$$

In general, carbon dioxide is formed to the largest extent but also carbon monoxide is measured as a result of insufficient combustion of the cokes. Based on the intensity of the signals of these gases, an indication of the amount of cokes formation on the catalyst surface could be provided. An overview of the observed gas formation for the different catalysts applied in reaction is shown in Figure 7-1. Besides the signals of CO and CO_2, also H_2O signals are detected. As the hydrotalcite based support

will react with water, the structure is continuously changing as according to the memory effect [1]. This water fraction could be resulting from reaction, although, this is only formed in marginal amounts due to formation of diethyl ether. What is more likely to occur is the reaction with water present in the atmosphere to which the used catalyst is exposed. When water is present in the feedstock, more reaction of the support is expected to occur. The used catalysts of the experiments with water are, however, not examined during this work. Subsequent heating, which is now performed via the temperature programmed oxidation will eventually result in desorption of this water via dehydroxylation (Chapter 2, 5.2).

As can be seen in Figure 7-1, the same shapes of CO and CO_2 signals are measured at temperatures between 550 and 650 K for all types of catalysts, suggesting a similar type of cokes formed during reaction. The intensity of the signals for the different catalysts is shown in Table 7-1. That way, it can be indicated that, apart from the incorporated catalyst with a short reduction cycle, all catalysts give rise to similar intensities of cokes formation. Hereby, the lowest intensity is measured for the incorporated catalyst with a complete reduction cycle. The same catalyst but with a short reduction cycle, on the contrary, will give rise to signals of an order of magnitude higher. This was yet observed in Figure 6-9 of Chapter 6, showing the high deactivation rate, i.e., 3.5 % per hour, in the first six hours in comparison to approximately 2.5 % for the one with the complete reduction cycle, illustrated in Figure 6-11.

The impregnated catalyst with a short reduction cycle shows similar deactivation rates, though the selectivity to methane formation is higher, giving rise to slightly higher intensities. According to the observed selectivity towards methane, one would expect that the impregnated catalyst with a complete reduction cycle would give rise to high intensities of cokes formation. It, however, requires consideration that the activity of the catalyst is rather low. Bearing in mind the amount of ethanol converted, the intensity of cokes formation of the catalyst would be in the same order of magnitude as the incorporated catalyst with a short reduction cycle.

Table 7-1: Intensity of CO and CO_2 signals during temperature programmed reduction of different catalysts

Catalyst	**Reduction cycle**	**CO intensity (a.u.)**	**CO_2 intensity (a.u.)**
PdZn/Mg(Al)O_x	Short	$2.75\ 10^{-8} \pm 8.35\ 10^{-9}$	$1.64\ 10^{-7} \pm 5.67\ 10^{-8}$
PdZn/Mg(Al)O_x	Complete	$1.51\ 10^{-5}$	$1.19\ 10^{-7}$
PdZn/Mg(Al)(Pd)(Zn)O_x	Short	$3.59\ 10^{-5} \pm 3.98\ 10^{-6}$	$2.47\ 10^{-6} \pm 1.74\ 10^{-6}$
PdZn/Mg(Al)(Pd)(Zn)O_x	Complete	$2.55\ 10^{-8} \pm 1.03\ 10^{-9}$	$1.55\ 10^{-7} \pm 9.54\ 10^{-9}$

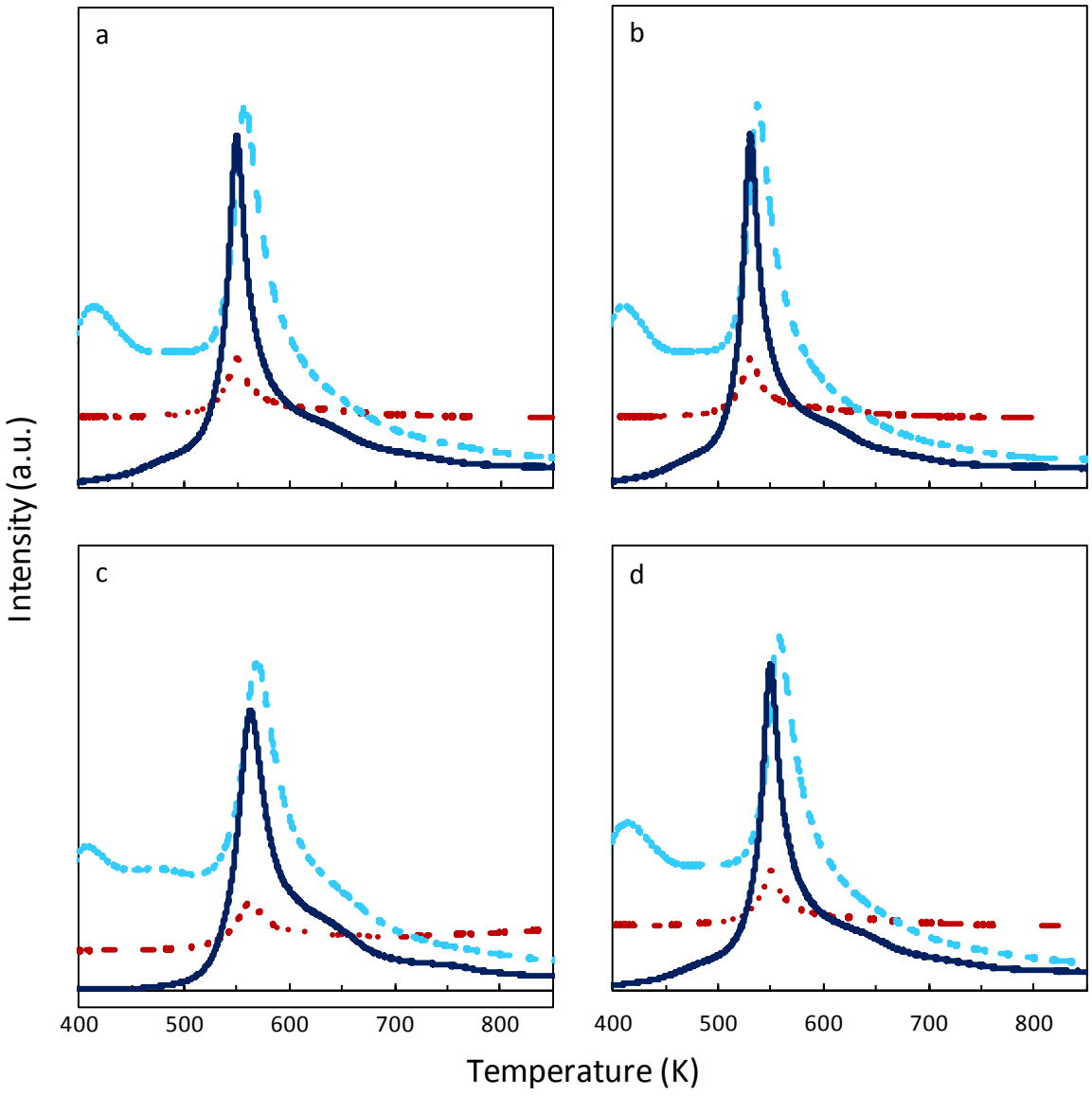

Figure 7-1: Observed gas formation during TPO of used PdZn/Mg(Al)O_x for a short (a) and complete (b) reduction cycle and of used PdZn/Mg(Al)(Pd)(Zn)O_x for a short (c) and complete (d) reduction cycle (full, dark blue: CO_2; dashed, red: CO; dotted, cyan: H_2O)

3 SINTERING DURING REACTION

One of the most important reasons for replacing the conventional copper catalysts by PdZn active sites was the sintering that occurred, resulting in a fast deactivation of the catalyst [2]. Palladium catalysts also show this disadvantage, though, the presence of Zn in the intermetallic compound should minimize this as much as possible [3].

The particle diameter distributions of the used catalysts are represented in Figure 7-2. According to these distributions, it could be argued that the average particle sizes are shifted towards higher values for the catalyst regenerated via a short reduction cycle, though, not for the ones regenerated via a complete reduction cycle. Changes will, here, remain within the confidence interval. This suggests that a complete reduction procedure will increase the stability of the formed PdZn intermetallic compound and hence counter possible sintering.

For the incorporated catalyst, regeneration via a short reduction procedure will show a maximum shifted more to higher particle sizes, i.e., 5 nm to 7.6 nm, along with a much higher variance in comparison to a complete reduction cycle, i.e., 2.2 nm to 1.5 nm. Before reaction, these cycles gave rise to similar particle sizes, though, a much wider variation was observed for the one with a short reduction cycle. After the reaction-regeneration cycles, this variance is decreased indicating the advantage of redistribution of the PdZn particles that is obtained for more sequencing oxidation and reduction steps. However, reaction is happening in between the regenerations. As this will result in sintering, not the same small particle sizes are able to be reached as with a complete reduction cycle for which no sintering is occurring.

The effect of sintering will affect the dispersion of the catalyst and consequently the number of active sites on the surface. An overview of the active surface area and the dispersion of the different catalysts determined via the particle size distribution is shown in Table 7-2. That way, it could be illustrated that for a catalyst with a complete reduction cycle, the regeneration procedure in between two reactions will further narrow the particle size distribution and enhance, in this manner, the dispersion of the catalyst. For the catalyst regenerated via short reduction cycles, the regeneration will not stabilize the PdZn sites sufficiently for possible sintering that is systematically shifting the particle size to higher values. This will result in a decrease in active PdZn sites at the surface of the catalysts, i.e., 0.016 versus 0.027 mmol g_{cat}^{-1} for a fresh catalyst (Table 4-2).

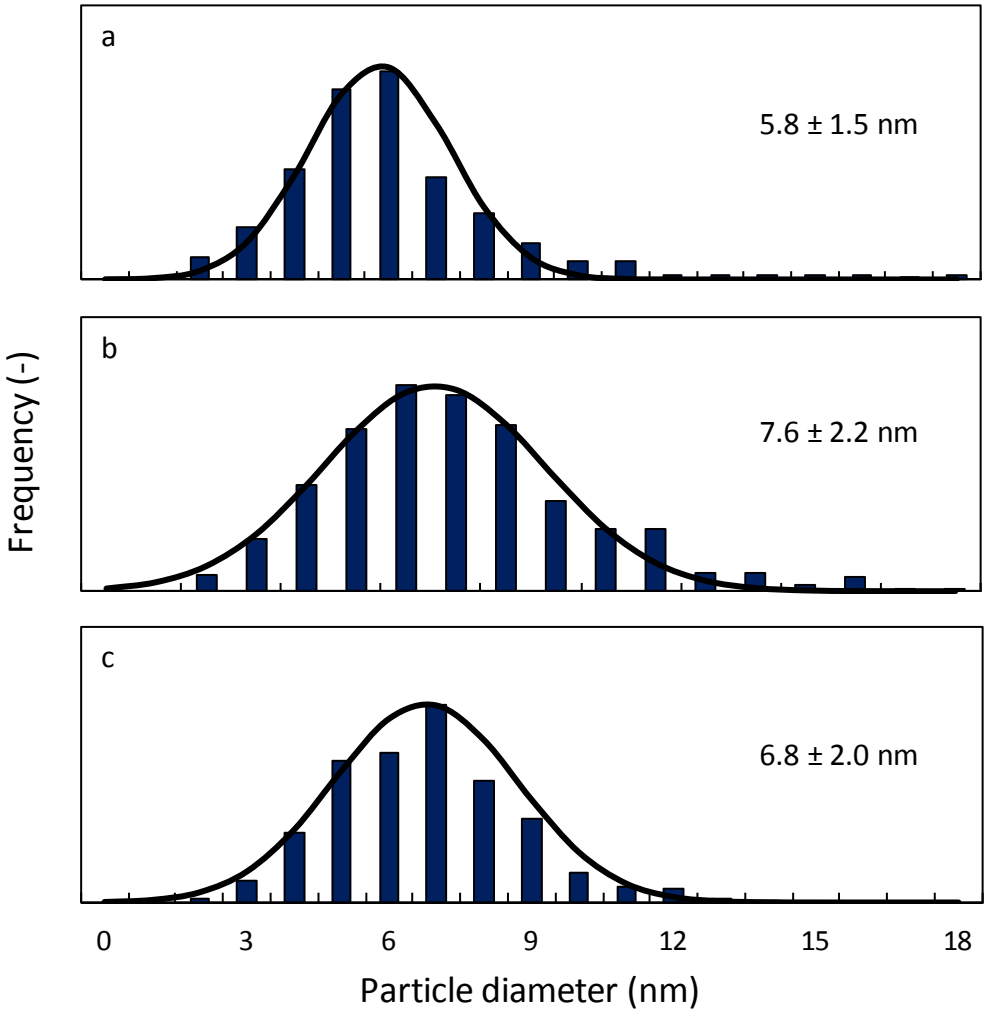

Figure 7-2: Particle size distributions for used PdZn/Mg(Al)(Pd)(Zn)O_x with a complete (a) and short (b) reduction cycle and used PdZn/Mg(Al)O_x with a complete reduction cycle (c)

Table 7-2: Active surface area and dispersion of the used catalysts determined via the particle size distribution

Catalyst	Reduction cycle	Number of active sites (mol g_{cat}^{-1})	Dispersion (-)
PdZn/Mg(Al)O_x	Complete	$1.84\ 10^{-5} \pm 6.1\ 10^{-6}$	0.196 ± 0.065
PdZn/Mg(Al)(Pd)(Zn)O_x	Short	$1.56\ 10^{-5} \pm 5.6\ 10^{-6}$	0.166 ± 0.060
PdZn/Mg(Al)(Pd)(Zn)O_x	Complete	$2.14\ 10^{-5} \pm 8.6\ 10^{-6}$	0.228 ± 0.091

4 EVOLUTION OF THE SUPPORT DURING REACTION

4.1 ON THE SURFACE OF THE SUPPORT

As was yet observed in the TPO experiments, the support of the intermetallic compound is continuously changing during reaction. In literature, it is reported that the mixed oxide will return to its original hydrotalcite based state in contact with water due to the memory effect. Initial reaction experiments, though, were performed with pure ethanol as feedstock, limiting the amount of water to the quantity formed during reaction, possibly via the formation of diethyl ether. Nonetheless, the greatest contributor of the water fraction inside the catalyst is the contact time with air between the reaction experiment and the BET analysis. The amount of water that is adsorbed, as such, could diffuse into the structure and trigger the transformation to the hydrotalcite disfavoring the surface area of the catalyst.

The surface area and average pore width of the catalysts applied for reaction are listed in Table 7-3. As such, it could be illustrated that indeed reaction will have a negative effect on the surface area of the catalyst. However, this decrease cannot solely be assigned to the effect of water as the regeneration procedure will again remove the incorporated water due to temperatures up to 823 K. Cokes deposition could be considered a second phenomenon that is occurring and will decrease the measured surface area of the catalyst. Furthermore, sintering could also show minor effects on these observations. The cause of this decrease is a complex interplay between different phenomena and no clear confirmation could be provided based on current characterization results. Also the observation that lower surface areas are measured for the catalysts that went through a complete reduction cycle, remains an unanswered question.

Table 7-3: Surface area and average pore width of the used catalysts

Catalyst	Reduction cycle	BET Surface area ($m^2\ g_{cat}^{-1}$)	BJH average pore width (nm)
PdZn/Mg(Al)O_x	Short	46.7 ± 1.2	146.9 ± 34.2
PdZn/Mg(Al)O_x	Complete	34.4 ± 5.0	257.0 ± 14.3
PdZn/Mg(Al)(Pd)(Zn)O_x	Short	23.3 ± 3.7	342.9 ± 28.0
PdZn/Mg(Al)(Pd)(Zn)O_x	Complete	17.0 ± 1.4	445.8 ± 20.1

4.2 EFFECT OF REACTION ON THE CRYSTALLOGRAPHIC PHASES

Figure 7-3 represents the XRD spectra of the used incorporated catalysts for both reduction cycles before and after oxidation. Again, the three characteristic peaks of the MgO periclase are observed while no signals were corresponding to the original layered structure of the hydrotalcite component. This suggests that the amount of water absorbed from the air during the time gap between reaction and characterization is of minor importance on the actual structure of the catalyst. If one compares both the catalysts regenerated via a short reduction cycle (samples a and b, Figure 7-3) with the ones via a complete reduction cycle (samples c and d, Figure 7-3), one observes the higher sharpness of the peaks for the latter. Hence, the size of the crystallographic planes of the support will be larger.

This trend, though, is not observed for the impregnated catalysts, shown in Figure 7-4, indicating that something else than the reduction period is responsible for this higher crystallinity.

A clear difference with the XRD spectra of the fresh catalysts, represented by Figure 4-2 in Chapter 4, is the occurrence of different signals corresponding to ZnO measured in Figure 7-4, i.e. at 32°, 34°, 36°, 47°, 56° and 62°. These peaks will be clearer after oxidation as a result of the transformation of Zn to ZnO. The longer the reduction-oxidation treatment at higher temperatures, the more it is expected that ZnO will diffuse to the surface and give rise to more intense signals on the spectra. As due to this diffusion, space inside the structure will become available, additional growth of the crystalline planes of the MgO periclase could be occurring, offering an explanation for the higher intensity of the signals of samples c and d of Figure 7-3. For the impregnated catalyst, no bulk ZnO will be present and hence this phenomenon will not be occurring. The longer time at higher temperatures will for these samples thus result in a lower crystallinity (samples c and d of Figure 7-4).

The PdZn intermetallic compound will give rise to intense signals located at diffraction angles of 42° and 44° and a weaker signal at 31°. As one compares the signals of both catalysts after reaction (samples a and c, Figure 7-3), it can be observed clearly that the intermetallic compound shows a sharper signal if a complete reduction cycle is applied. It is yet brought to attention in the distribution of the PdZn particle sizes (Figure 7-2) that a short reduction cycle will not give rise to a good dispersion of the particles despite the low intensity that is measured for the corresponding PdZn signals. A possible argument could be that due to the large variance of the distribution of the PdZn particles sizes, the corresponding X-rays will destructively interfere with each other, resulting in a lower intensity.

No signals corresponding to metallic Zn or Pd were measured at the catalyst surface. This suggests that these are either not present after reaction or finely dispersed on the surface. The latter could be expected as more likely as in Chapter 6, a small selectivity to the decomposition of ethanol, occurring at metallic Pd sites, was measured. It is expected that subsequent treatment of the catalysts via temperature programmed oxidation will result in a disappearance of the signals of PdZn. This gives rise to signals corresponding to the oxides of both Pd and Zn. The latter were yet observed to be increasing in intensity and also the former shows a corresponding signal located at 33°, measured in sample a and c of Figure 7-3.

The formation of cokes on the surface of the catalyst, which was yet confirmed by TPO, should result in the corresponding peaks at 42°. Nonetheless, PdZn intermetallic compounds will show signals in a similar range or it could be possible that the coke deposition is finely dispersed. After oxidation, both signals will have disappeared, indicating that XRD alone cannot give a decisive answer.

The XRD spectra of the impregnated catalysts are shown in Figure 7-3 for both a complete and a short reduction cycle. As was mentioned previously, the contrary is observed in the intensity of the signals of MgO in comparison to the incorporated catalyst. Here, used catalysts with a short reduction cycle show the highest crystallinity. This effect was yet assigned to the diffusing ZnO from the structure to the surface in the incorporated catalyst. As the impregnated catalyst will not have this bulk ZnO present, it will only sense the negative effect of a longer treatment on higher temperatures, i.e., a decrease in crystallinity.

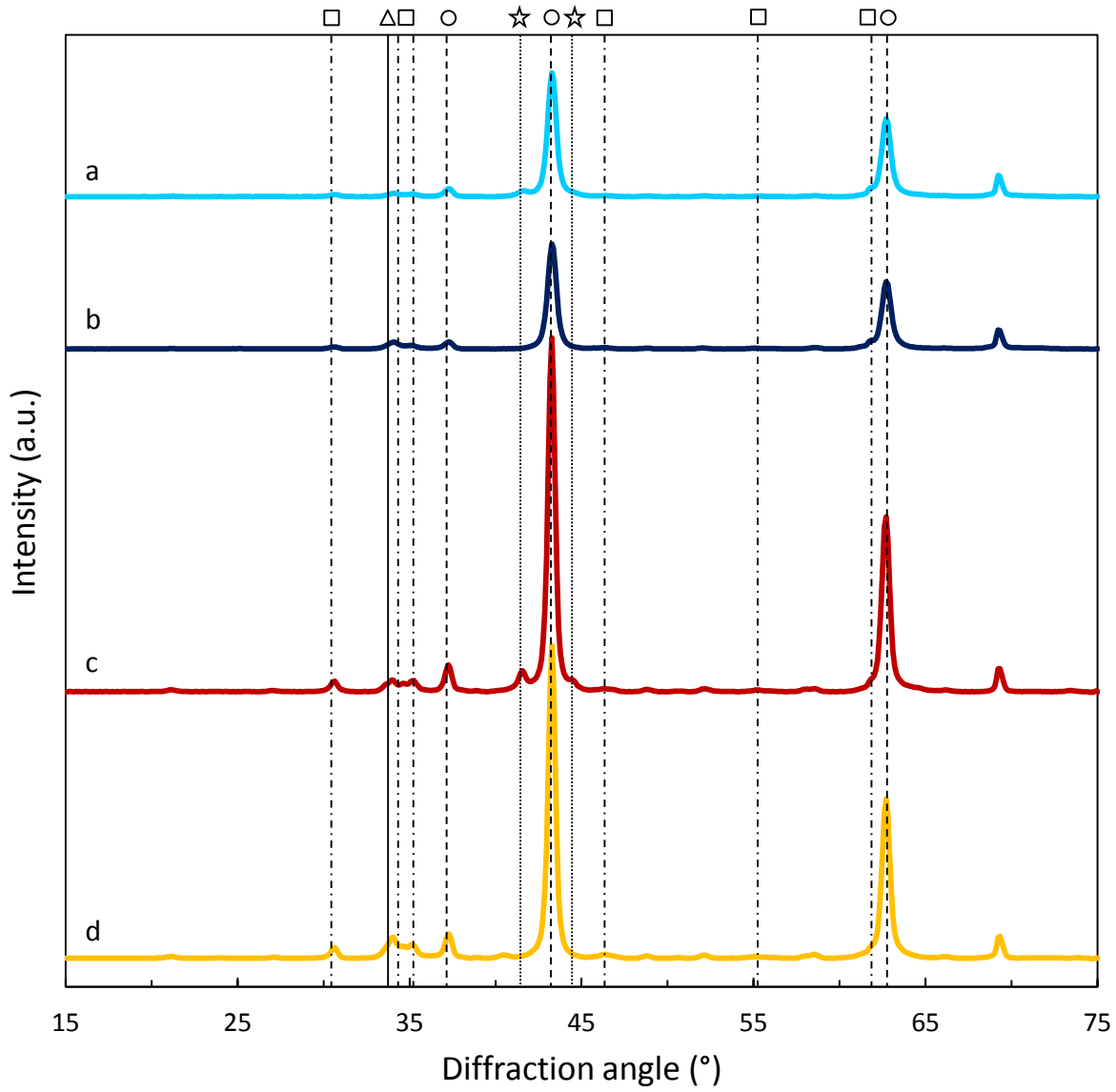

Figure 7-3: XRD spectra of PdZn/Mg(Al)(Pd)(Zn)O_x with a short reduction cycle: used (a, cyan) and after oxidation (b, dark blue) and PdZn/Mg(Al)(Pd)(Zn)O_x with a complete reduction cycle: used (c, red) and after oxidation (d, yellow) (○: MgO; □: ZnO; △: PdO; ☆: PdZn)

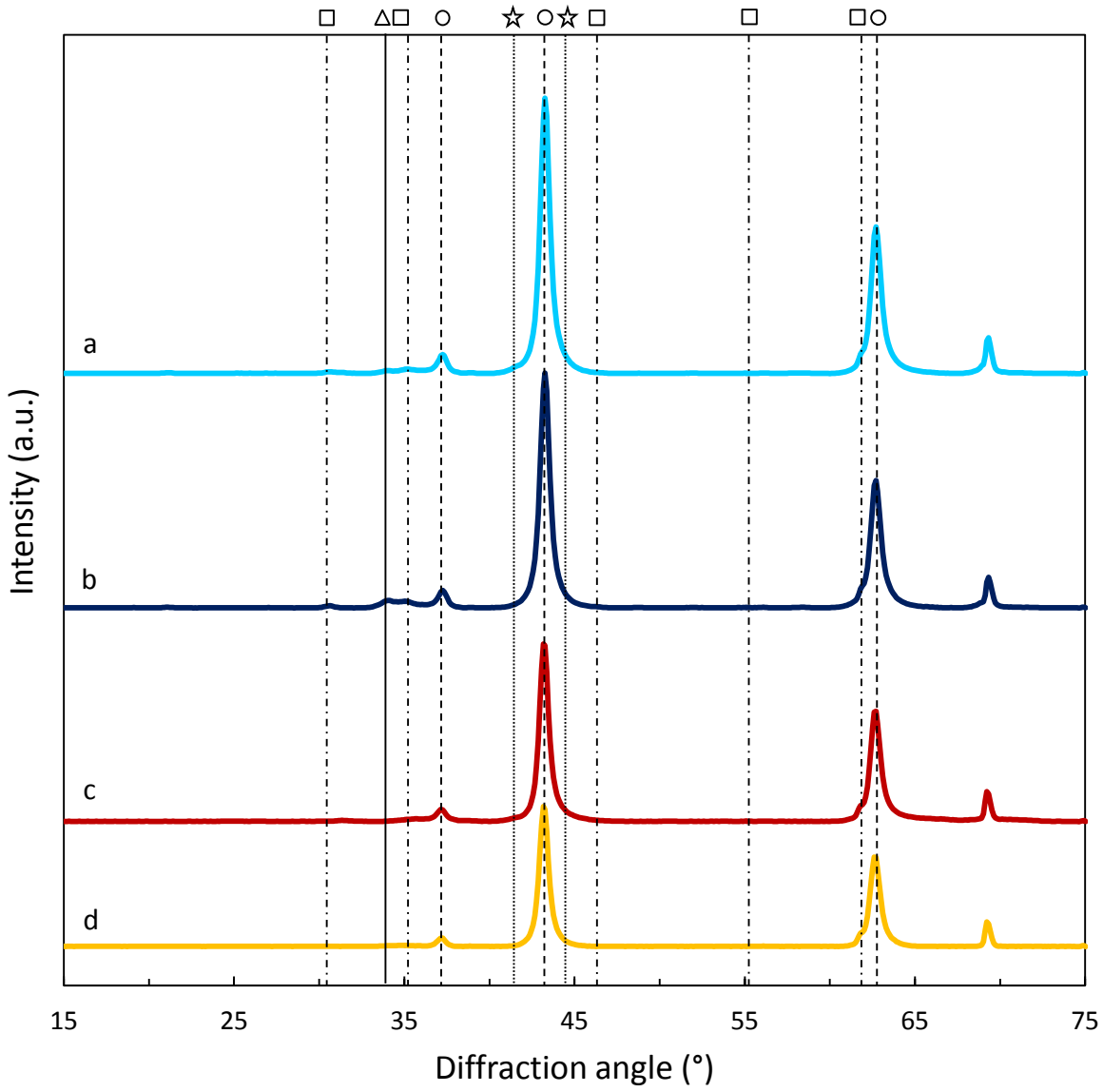

Figure 7-4: XRD spectra of PdZn/Mg(Al)O_x with a short reduction cycle: used (a, cyan) and after oxidation (b, dark blue) and PdZn/Mg(Al)O_x with a complete reduction cycle: used (c, red) and after oxidation (d, yellow) (○: MgO; □: ZnO; △: PdO; ☆: PdZn)

Due to the less uniform distribution of ZnO on the surface, in comparison to the incorporated catalyst, a lower intensity of the signals corresponding to ZnO will be observed as a result of destructive interference of the XRD signals. The same reasoning could be found for the signals corresponding to PdZn as these were also very broad and almost non-observable (samples b and d, Figure 7-3) at 42° and 44°. Nonetheless, a complete reduction cycle will still give rise to a more uniform distribution than the one regenerated via the short reduction cycle, hence giving rise to the largest intensity of signals corresponding to PdZn and ZnO among the impregnated catalysts.

4.3 COMBINING XRD WITH OXIDATION

The spectra lack in signals corresponding to possible coke deposition due to the overlap with PdZn signals or due to fine dispersion on the surface. Therefore, a more in-depth analysis is applied towards the variation of the XRD spectra upon oxidation. This will be performed by means of a combined TPO-XRD technique which measures the XRD spectra under a constant oxygen flow and a temperature ramp of 10 K per minute.

The TPO-XRD spectra of used PdZn/Mg(Al)(Pd)(Zn)O_x for both a short and complete reduction cycle are shown in Figure 7-5 and Figure 7-6, respectively. Next to the corresponding signals of MgO, located at 37° and 43°, the most intense peaks observed, especially for the one at a complete reduction cycle, are the ones of the PdZn intermetallic compound. These are located at 31°, 42° and 44°. These peaks will disappear when the temperature is further increased above 700 K. During this oxidation, no signals corresponding to Pd and Zn are measured, indicating that the PdZn intermetallic compound is directly reduced to ZnO and PdO. The latter is shown by the occurrence of the peak at 34° at around 650 K. The peaks corresponding to ZnO, in previous XRD spectra yet identified as being present at 31°, 34°, 36°, etc. are already present in the reduced state, hence showing less alteration upon oxidation. The loss of intensity of the peak at 31°, though, could be assigned to the oxidation of PdZn which has a weak signal at similar diffraction angles.

The PdZn intermetallic compound will thus directly be oxidized into its oxides of Pd and Zn. This could be assigned to the fact that the combination of the metallic Pd and Zn species will stabilize the intermetallic compound as these species separately are reducing at much lower temperatures. This can be observed by the signals of metallic Pd, i.e., at 47° and metallic Zn, i.e., at 37° and 39° which will lose intensity between 300 and 500 K. The Zn signal, though, shows a special behavior as initially a decrease in intensity is observed while a small peak will remain until higher temperatures. A possible reasoning could lie in a fast oxidation to ZnO that will cover the remaining Zn and hence protect it against oxidation. When the temperature is further increased, the ZnO will eventually redistribute across the surface, leading to the oxidation of the rest of the Zn.

Signals of coke deposition were thus not observed due to the overlap with the signals of the PdZn intermetallic compound. Though, if one looks closely, small signals of carbon can be observed at around 41° which will disappear in the range of 500 to 700 K as was observed in the temperature programmed oxidation measurements shown in Figure 7-1. As was mentioned previously, the PdZn compound will be completely oxidized when the temperature exceeds 700 K, hence the first losses in intensity of the signal could be assigned to oxidation of the cokes.

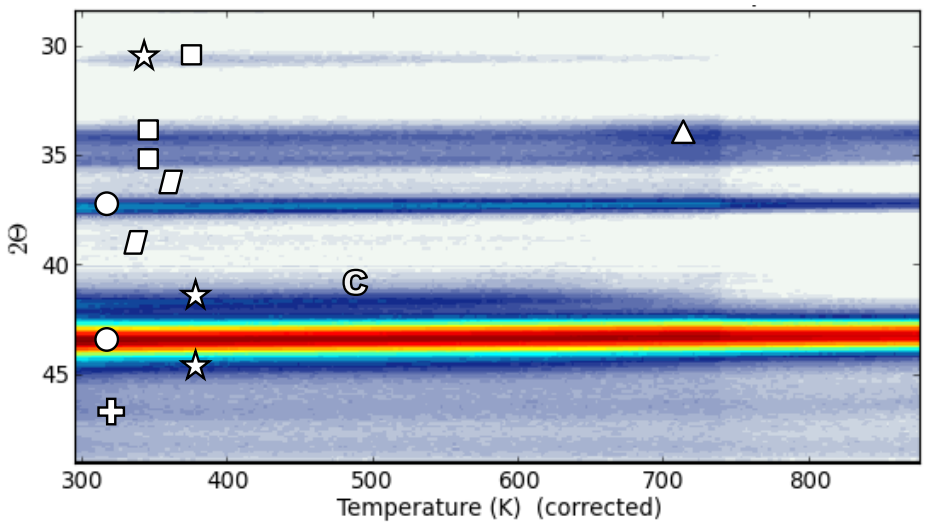

Figure 7-5: TPO-XRD spectrum of used PdZn/Mg(Al)(Pd)(Zn)Ox for a short reduction cycle
(△: PdO; □ : ZnO; ✚ : Pd; ▱ : Zn; ☆ : PdZn; ○ : MgO; ℂ : Cokes)

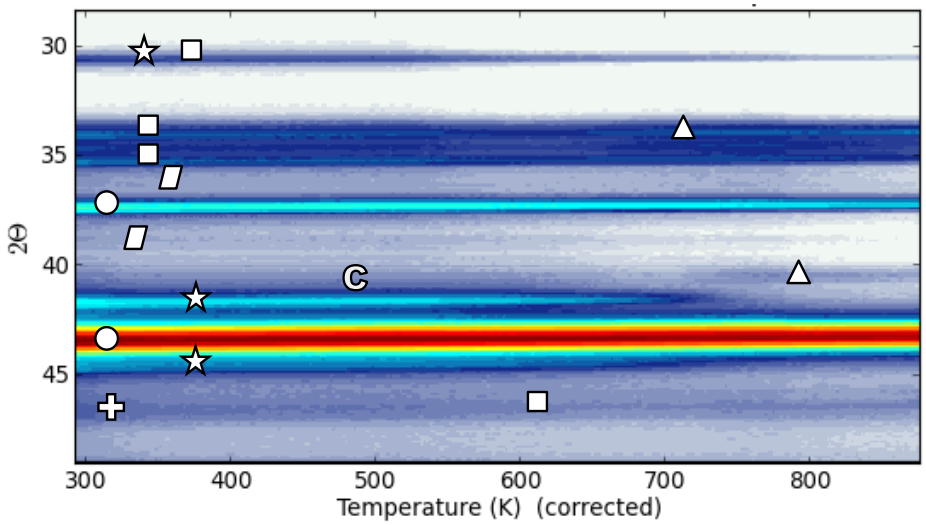

Figure 7-6: TPO-XRD spectrum of used PdZn/Mg(Al)(Pd)(Zn)Ox for a complete reduction cycle
(△: PdO; □ : ZnO; ✚ : Pd; ▱ : Zn; ☆ : PdZn; ○ : MgO; ℂ : Cokes)

A representation of the TPO-XRD spectra of the used impregnated catalysts, both with a short or complete reduction cycle, are shown in, respectively, Figure 7-7 and Figure 7-8. Similar observations can be made when looking at the PdZn signals, though lower intensities are observed compared to the incorporated catalyst with a complete reduction cycle. Again, the uniformity of the surface could be a reasonable explanation for this observation. A faster disappearance of the corresponding signal at 42° and 44° could also show the better stability of the PdZn intermetallic compound on the incorporated catalyst.

Comparing both impregnated catalysts with each other, a higher intensity in signals is observed for both the oxides of Pd and Zn, indicating a higher uniformity on the surface upon oxidation for the catalyst with a short reduction cycle. Further, signals for metallic Zn, i.e., at 37° and 39°, and Pd, i.e., at 47°, are observed. The intensity of these signals in comparison to the signal of PdZn, suggests a higher fraction of metallic Pd present in both the impregnated catalysts relative to the incorporated ones. This results in a lower selectivity to acetaldehyde and, as such, a confirmation of the observations in Chapter 6. Especially the one with a complete reduction cycle shows these higher intensity differences. Furthermore, a better distribution of the oxides in the one with the short reduction cycle could also suggest a better distribution of the PdZn intermetallic compound before oxidation. In such a way, this could explain the higher activity and selectivity that was observed for the impregnated catalyst regenerated after a short reduction cycle in comparison to the one with a complete reduction cycle. Hereby, the higher intensity of signals corresponding to metallic Pd and Zn contributes to the hypothesis of a more difficult formation of PdZn as redistribution over the surface is less facilitated for the impregnated catalyst.

5 CONCLUSIONS

One of the general conclusions in Chapter 6 on reaction experiments is the superiority of the incorporated catalyst prepared via a complete reduction cycle as this catalyst is not solely the most active and selective one, but is also able to be regenerated adequately. An evaluation on the structural properties by means of characterization only confirms these results as coke deposition points out to be the lowest at this catalyst. Furthermore, complete reduction cycle are able to stabilize the PdZn intermetallic compound in order to counter possible sintering that could occur during reaction of the catalyst. That way, the particle size distribution could be maintained resulting in the highest values of dispersion obtained for the catalysts with a complete reduction cycle.

XRD spectra point out the presence of ZnO next to the expected signals of PdZn and MgO, confirming the difficulty of reduction to metallic Zn. In the case of the incorporated catalyst, ZnO would eventually diffuse from the bulk to the surface, ameliorating that way the crystallinity of the mixed oxide support. Further combination of XRD with TPO reveals more information about the oxidation mechanism of the catalyst. As such, the spectra show the direct transformation of the PdZn intermetallic compound into its oxides of Pd and Zn. Subsequently, these species would redistribute on the surface of the mixed oxide, indicating, in this manner, the effectivity of a higher number of sequencing oxidation-reduction cycles.

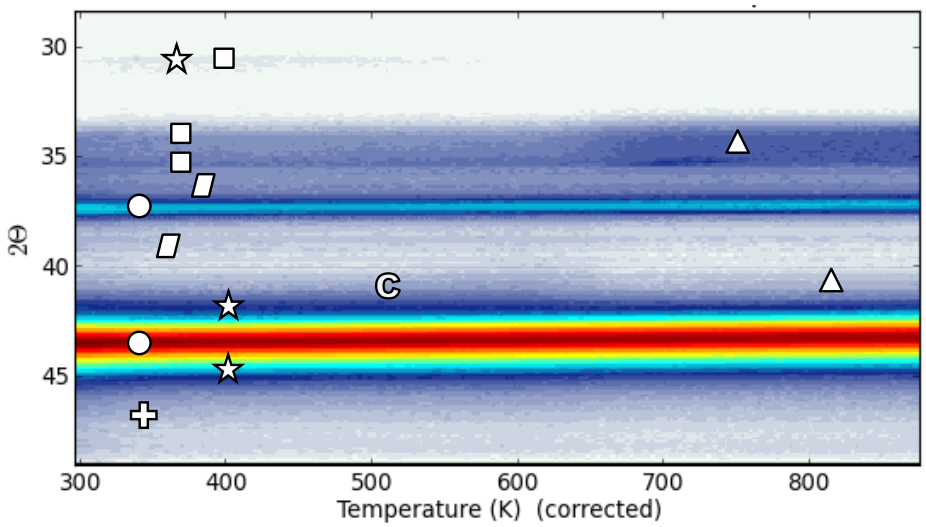

Figure 7-7: XRD-TPO spectrum of used PdZn/Mg(Al)O_x for a short reduction cycle
(△: PdO; □ : ZnO; ☆ : PdZn; ○ : MgO; ℂ : Cokes)

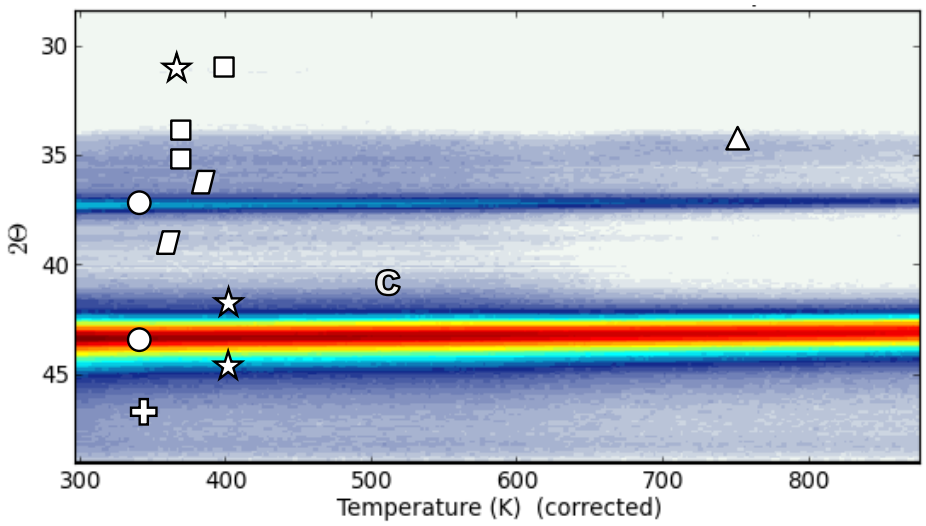

Figure 7-8: XRD-TPO spectrum of used PdZn/Mg(Al)O_x for a complete reduction cycle
(△: PdO; □ : ZnO; ✚ : Pd; ▱ : Zn; ☆ : PdZn; ○ : MgO; ℂ : Cokes)

6 REFERENCES

[1] V. Rives, Surface Texture and Electron Microscopy Studies of Layered Double Hydroxides, Layered Double Hydroxides: Present and Future, Nova Science Publishers, Inc. 2006.
[2] Y.J. Tu, Y.W. Chen, Effects of alkali metal oxide additives on Cu/SiO2 catalyst in the dehydrogenation of ethanol, Ind Eng Chem Res, 40 (2001) 5889-5893.
[3] S.C. Shekar, J.K. Murthy, P.K. Rao, K.S.R. Rao, E. Kemnitz, Selective hydrogenolysis of dichlorodifluoromethane(CCl2F2) over CCA supported palladium bimetallic catalysts, Appl Catal a-Gen, 244 (2003) 39-48.

Chapter 8: Towards a Kinetic Model for Ethanol Dehydrogenation

1 INTRODUCTION

An important pillar within the application of model based catalyst design is the construction of a kinetic model, taking into account the different reactions occurring at the catalyst surface. After validation of this model with experimental data, it could provide the link of the reaction's kinetics with the performance of the catalyst. This is performed by defining the catalyst descriptors within the kinetic model which will affect the activity and selectivity of the catalyst and are depending on the properties of the catalyst. That way, adjusting these properties will result in an optimization of the design. As an extensive modeling approach does not belong to the scope of this work, only a short introduction to the construction of a kinetic model for ethanol dehydrogenation is provided, taking into account a limited amount of reactions and species.

2 CONSIDERATIONS ABOUT THE REACTION MECHANISM

Due to the growing production of bio-ethanol, studies on ethanol conversion reactions such as dehydrogenation have grown tremendously in the past decade. Though, in most of these studies, the catalytic conversion was not solely restricted to acetaldehyde but continued towards ethyl acetate. First thoughts on the reaction mechanism were yet delivered in Chapter 2 with a mechanism proposed by Sato et al. [1], represented in Figure 8-1. Ethanol will hereby be dehydrogenated at the surface and either desorb or react with an adsorbed ethanol molecule. According to Santacesaria et al. [2] a main factor of influence is the partial pressure of ethanol as this will indicate the density of adsorbed ethanol molecules on the surface. A high selectivity to acetaldehyde would therefore require operating pressures near atmospheric pressure.

The adsorption of hydrogen at the surface can occur by an associative and/or a dissociative mechanism. Little research is applied in this area towards PdZn intermetallic compounds, although, they offer the same electronic composition as copper indicating that a similar mechanism will occur. According to Kuang et al. [3] the associative mechanism is favored in which the adsorption of molecular hydrogen will result in a weaker hydrogen-hydrogen bond and consequently a more reactive molecule. It should, however, be stressed that also the dissociative mechanism could occur, involving two active sites [4]. As it is expected that hydrogen will only chemisorb on metallic Pd, which provides two active sites, while Zn is assumed to provide none, an equivalent number of 1 per active site of PdZn is proposed.

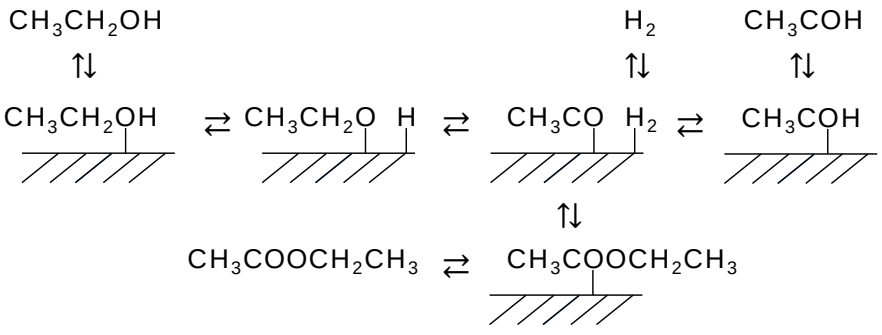

Figure 8-1: Reaction mechanism on the dehydrogenation of ethanol according to Sato et al. [1]

In Chapter 6, also the presence of side products such as methane, carbon monoxide and diethyl ether are observed. Though, these will not be considered in the preliminary kinetic model yet as these reactions will take place at other active sites. The decomposition of acetaldehyde towards methane and carbon monoxide is generally due to the presence of metallic Pd sites. As it is a key assumption in Langmuir-Hinshelwood kinetics that all adsorption sites are identical, introducing Pd sites would increase the number of parameters due to the presence of two different active sites. The dehydration of ethanol to diethyl ether could be assigned to acid sites present on the mixed oxide support. Due to the low selectivity to diethyl ether, this reaction will also be neglected.

3 CONSTRUCTION OF A KINETIC MODEL

3.1 REACTION RATE EQUATIONS

A kinetic model will be constructed based on the Langmuir-Hinshelwood-Hougen-Watson (LHHW) mechanism. In Langmuir-Hinshelwood kinetics it is assumed that all species are adsorbed and accommodated (in quasi-equilibrium) with the surface before they take part in any reactions. Hence species react in the chemisorbed state on the surface. For simplicity, the decomposition and dehydration reaction of ethanol are neglected and it will be assumed that hydrogen does not dissociate upon adsorption. Following adsorption and desorption steps will then occur in the mechanism:

$$EtOH + {}^{*} \rightleftarrows EtOH^{*} \tag{7-1}$$

$$H_2{}^{*} \rightleftarrows H_2 + {}^{*} \tag{7-2}$$

$$AcH^{*} \rightleftarrows AcH + {}^{*} \tag{7-3}$$

$$EtOAc^{*} \rightleftarrows EtOAc + {}^{*} \tag{7-4}$$

As these reactions are assumed to be in quasi-equilibrium, they are characterized by an equilibrium coefficient:

$$K_{EtOH} = \frac{\theta_{EtOH}}{p_{EtOH}\theta_{*}} \tag{7-5}$$

$$K_{H_2} = \frac{\theta_{H_2}}{p_{H_2}\theta_{*}} \tag{7-6}$$

$$K_{AcH} = \frac{\theta_{AcH}}{p_{AcH}\theta_{*}} \tag{7-7}$$

$$K_{EtOAc} = \frac{\theta_{EtOAc}}{p_{EtAc}\theta_{*}} \tag{7-8}$$

With θ_i Fraction of sites occupied by component i [-]

p_i Partial pressure of component i [Pa]

Note that in contrast to the reaction scheme represented in Figure 8-1, further simplification is applied to both dehydrogenation reactions, going respectively to acetaldehyde and ethyl acetate:

$$EtOH^* + {}^* \rightleftarrows AcH^* + {H_2}^* \tag{7-9}$$

$$AcH^* + EtOH^* \rightleftarrows EtOAc^* + {H_2}^* \tag{7-10}$$

By making use of these simplified reactions the number of parameters of the kinetic model can be significantly reduced compared to a full microkinetic model. The rate of the first dehydrogenation reaction (equation (7-9)) can then be written as:

$$r_{dhg,1} = r_{dhg,1+} - r_{dhg,1-} \tag{7-11}$$

These reaction rates are defined as according to the mean-field approximation, taking into account a probability factor that indicates the probability that both sites are neighbors:

$$r_{dhg,1+} = k_{dhg,1+}\theta_{EtOH}\theta_* C_t^2 \frac{z}{C_t} \tag{7-12}$$

With C_t Number of active sites at the surface [mol kg_{cat}^{-1}]

In which z represents the number of adjacent sites to an adsorbed ethanol molecule. As PdZn intermetallic compounds represent a CuAu-*L* 1_0 tetragonal structure [5], the value of z is 4. The rate of the first dehydrogenation reaction is then written as follows:

$$r_{dhg,1} = (k_{dhg,1+}\theta_{EtOH}\theta_* - k_{dhg,1-}\theta_{H_2}\theta_{AcH})zC_t \tag{7-13}$$

As the number of active sites remains constant during operation, following equation will hold:

$$\theta_* + \theta_{EtOH} + \theta_{H_2} + \theta_{AcH} + \theta_{EtOAc} = 1 \tag{7-14}$$

Thus one can rewrite the rate of the first dehydrogenation as:

$$r_{dhg,1} = \frac{zk_{dhg,1+}K_{EtOH}p_{EtOH}\left(1 - \frac{p_{H_2}p_{AcH}}{p_{EtOH}K_1}\right)C_t}{(1 + K_{EtOH}p_{EtOH} + K_{H_2}p_{H_2} + K_{AcH}p_{AcH} + K_{EtOAc}p_{EtOAc})^2} \tag{7-15}$$

with

$$K_1 = \frac{K_{dhg,1}K_{EtOH}}{K_{AcH}K_{H_2}} \tag{7-16}$$

and

$$K_{dhg,1} = \frac{k_{dhg,1+}}{k_{dhg,1-}} \tag{7-17}$$

Analogously the rate of the second dehydrogenation reaction can be constructed:

$$r_{dhg,2} = \frac{zk_{dhg,2+}K_{EtOH}K_{AcH}p_{EtOH}p_{AcH}\left(1 - \frac{p_{H_2}p_{EtOAc}}{p_{EtOH}p_{AcH}K_2}\right)C_t}{(1 + K_{EtOH}p_{EtOH} + K_{H_2}p_{H_2} + K_{AcH}p_{AcH} + K_{EtOAc}p_{EtOAc})^2} \tag{7-18}$$

with

$$K_2 = \frac{K_{dhg,2}K_{EtOH}K_{AcH}}{K_{EtOAc}K_{H_2}} \tag{7-19}$$

and

$$K_{dhg,2} = \frac{k_{dhg,2+}}{k_{dhg,2-}} \tag{7-20}$$

3.2 REACTOR MODEL

Previously constructed rate equations for the first and second dehydrogenation reaction are subsequently combined to generate a link with the conversion and selectivity obtained via experiments. When taking into account the mass balance over the reactor, a relation between the flow rates and the production rate is found, as represented by equation (5-2):

$$\frac{dF_i}{dW} = R_{w,i} \tag{7-21}$$

It should be stressed that this equation is only valid in case of the ideal plug flow assumption which was validated in Chapter 5. Since there are two linear independent reaction equations present, an equal number of so called key components can be assigned. The term key component, as it is defined in Chemical Reactors: Fundamentals and Applications of Guy B. Marin at Ghent University [6], is indicated as a component for which it is at least required to derive a mass balance. Ethanol and acetaldehyde will be assigned as key components during operation. The corresponding mass balance of ethanol and acetaldehyde are represented by following expressions:

$$\frac{dF_{EtOH}}{dW} = R_{w,EtOH} = -r_{dhg,1} - r_{dhg,2} \tag{7-22}$$

$$\frac{dF_{AcH}}{dW} = R_{w,AcH} = r_{dhg,1} - r_{dhg,2} \tag{7-23}$$

The flow rates of ethanol and acetaldehyde are linked with the conversion and selectivity via following expressions:

$$F_{EtOH} = F_{EtOH,0}(1 - X_{EtOH}) \tag{7-24}$$

$$F_{AcH} = F_{EtOH,0} X_{EtOH} S_{AcH} \tag{7-25}$$

The flow rates of, respectively, hydrogen and ethyl acetate can be determined from the elemental balances:

$$F_{H_2} = F_{EtOH,0} - F_{EtOH} \tag{7-26}$$

$$F_{EtOAc} = \frac{1}{2}(F_{EtOH,0} - F_{EtOH} - F_{AcH}) \tag{7-27}$$

According to the law of Dalton, the partial pressures of the respective components can be generated from the molar flow rates.

3.3 REGRESSION OF KINETIC PARAMETERS

If one overviews both reaction rate equations, expressions (7-15) and (7-18), a distinction can be made between 8 different kinetic parameters (k_{A-B} and K_{C-H}):

$$r_{dhg,1} = \frac{k_A p_{EtOH}\left(1 - \frac{p_{H_2} p_{AcH}}{p_{EtOH} K_C}\right)}{\left(1 + K_D p_{EtOH} + K_E p_{H_2} + K_F p_{AcH} + K_G p_{EtOAc}\right)^2} \tag{7-28}$$

$$r_{dhg,2} = \frac{k_B p_{EtOH} p_{AcH}\left(1 - \frac{p_{H_2} p_{EtOAc}}{p_{EtOH} p_{AcH} K_H}\right)}{\left(1 + K_D p_{EtOH} + K_E p_{H_2} + K_F p_{AcH} + K_G p_{EtOAc}\right)^2} \tag{7-29}$$

However, a correct analysis of the kinetic parameters will consist of simultaneously fitting all data to the model. Therefore, the temperature dependence of the parameters should be incorporated in the model explicitly. For the rate coefficients this can be represented by the Arrhenius relation. As the adsorption is in quasi-equilibrium, the temperature dependence of the adsorption coefficients is characterized by the adsorption enthalpy and entropy:

$$k = A \exp\left[-\frac{E_a}{RT}\right] \tag{7-30}$$

$$K_X = \exp\left[\frac{\Delta S_X}{R}\right] \exp\left[-\frac{\Delta H_X}{RT}\right] \tag{7-31}$$

With ΔH_X Adsorption enthalpy of component X [J mol^{-1}]
ΔS_X Adsorption entropy of component X [J mol^{-1} K^{-1}]

Though, one has to note that the newly introduced parameters have a high probability of correlation due to the limited temperature range over which a chemical reaction can be varied. In order to counter these correlations, a reparametrization is applied [7]. Convergence difficulties are as such reduced to a minimum:

$$k = k_{T_{avg}} \exp\left[-\frac{E_a}{R}\left(\frac{1}{T} - \frac{1}{T_{avg}}\right)\right] \tag{7-32}$$

$$K_X = K_{X,T_{avg}} \exp\left[-\frac{\Delta H_X}{R}\left(\frac{1}{T} - \frac{1}{T_{avg}}\right)\right] \tag{7-33}$$

In order to reduce the number of parameters the temperature dependence of the equilibrium coefficients of the gas phase reactions, i.e., K_B and K_H, are determined via thermodynamic data obtained from literature. For a more detailed elaboration, the reader is referred to Appendix A. Following temperature dependence will be incorporated in the kinetic model:

$$\ln[K_C] = \frac{3758.4}{T} - 1.2986 \tag{7-34}$$

$$\ln[K_H] = \frac{-9981.6}{T} + 17.95 \tag{7-35}$$

4 REFERENCES

[1] A.G. Sato, D.P. Volanti, I.C. de Freitas, E. Longo, J.M.C. Bueno, Site-selective ethanol conversion over supported copper catalysts, Catal Commun, 26 (2012) 122-126.
[2] E. Santacesaria, G. Carotenuto, R. Tesser, M. Di Serio, Ethanol dehydrogenation to ethyl acetate by using copper and copper chromite catalysts, Chem Eng J, 179 (2012) 209-220.
[3] X.J. Kuang, X.Q. Wang, G.B. Liu, A density functional study on the adsorption of hydrogen molecule onto small copper clusters, J Chem Sci, 123 (2011) 743-754.
[4] G. Carotenuto, R. Tesser, M. Di Serio, E. Santacesaria, Kinetic study of ethanol dehydrogenation to ethyl acetate promoted by a copper/copper-chromite based catalyst, Catal Today, 203 (2013) 202-210.
[5] Z.X. Chen, K.M. Neyman, A.B. Gordienko, N. Rosch, Surface structure and stability of PdZn and PtZn alloys: Density-functional slab model studies, Phys Rev B, 68 (2003).
[6] G.B. Marin, Chemical Reactors: Fundamentals and Applications, Ghent University, 2015.
[7] J.W. Thybaut, Kinetic Modeling and Simulation, Ghent University, 2014.

Chapter 9: General Conclusions and Future Work

1 CONCLUSIONS

During this work, PdZn intermetallic compounds supported on a mixed oxide basis are introduced in the dehydrogenation of bio-ethanol as a substitute for conventional copper catalysis. The goal of this work is to optimize the synthesis and reduction method applied to create the catalyst in terms of catalytic properties, such as conversion and selectivity to acetaldehyde.

The catalysts used in this work are synthesized in two ways: incorporation through coprecipitation and grafting through impregnation. During reduction to the PdZn intermetallic compound, it is observed that metallic Zn will diffuse into the metallic Pd upon reduction with hydrogen. Based on TPR experiments, it could hereby be concluded that Pd will act as a hydrogen carrier in its saturated hydride form. At the high temperatures at which reduction takes place, i.e., 823 K, a spill-over of hydrogen to ZnO will then eventually occur, easing the reduction to metallic Zn. Between both synthesis methods, TPR-XRD spectra illustrated a difference in the formation of PdZn which showed to be obtained at milder conditions for the incorporated catalyst. On the impregnated catalyst, reduction with hydrogen to form the intermetallic compound takes place at higher temperature ranges and this could be assigned to the fact that the Pd and Zn particles, introduced on the catalyst via grafting, are larger. Furthermore, measurements of the specific surface area point out a non-ideal formation of the mixed oxide when Pd ions were incorporated in the structure, owing to their larger ionic radii. Reduction with hydrogen, though, leads to diffusion of these ions to the surface and hence an increase in both surface area and pore size width. This effect is not observed for the impregnated catalysts as PdO and ZnO are grafted on the surface and are not present in the bulk.

The reduction method could be further improved by alternating the reduction with oxidation cycles, enabling that way, a redistribution of the oxides of Pd and Zn over the surface and causing hence a narrower particle size distribution. Especially in the case of the impregnated catalyst, a beneficial effect is observed as TEM shows a dual distribution with both small, i.e., 5.5 nm, and larger clusters, i.e., 11 nm, present after only one reduction. TEM results after increasing the number of oxidation-reduction cycles, on the contrary, will show one distribution located around 7.0 nm. For the incorporated catalyst with a complete reduction cycle, even better results are obtained with an average particle size of 5.3 nm, owing to a better redistribution of the oxides over the surface. As a higher number of cycles will comprise a higher regeneration time, the procedure is a trade-off between time and uniformity of the catalyst surface. The number of reduction-oxidation cycles is, therefore, set at two with a finishing reduction step to form the PdZn intermetallic compound.

Catalytic reaction experiments in a packed bed reactor point out the differences between the synthesis methods and the benefit of an increase in reduction-oxidation cycles. Considering all tested catalysts, the incorporated catalyst reduced via a complete reduction cycle shows to have superior catalytic properties reaching a conversion of 27.6 % with a selectivity to acetaldehyde of 97.6 %. The impregnated catalyst on the contrary, reduced via the same method, shows considerably lower properties, i.e., 5.4 % conversion of ethanol and 92.8 % selectivity to acetaldehyde. Nonetheless, both catalysts have the benefit over the ones prepared via a short reduction cycle as regeneration points out to be not reproducible for the latter ones. This confirms the increased

stability of the PdZn intermetallic compound prepared via sequencing reduction-oxidation cycles and hence the necessity for further kinetic investigation.

Based on the deactivation curves, two different regions could be distinguished. TPO experiments show the deposition of cokes on the surface during reaction, responsible for a fast initial deactivation of the catalyst. This phenomenon could possibly be assigned to the Boudouard reaction and methane decomposition occurring at the Pd sites on the catalyst. As cokes subsequently would deposit on these same sites, the effect of deactivation is only shown in the initial hours on stream. A higher number of sequencing reduction-oxidation cycles is hereby beneficial in the reduction of cokes formation due to the improved stabilization of PdZn. The incorporated catalyst is then again the superior one. The second deactivation period shows a more restricted linearly decreasing trend and is assigned to sintering occurring during reaction. Due to the increased stabilization of the PdZn compound in a complete reduction cycle, this effect is not observed for the corresponding catalysts. Combined TPO and XRD confirms this advantage of sequencing oxidation-reduction cycles as the oxides of Pd and Zn are redistributed across the surface upon oxidation. Subsequent reduction is hence improved as the oxides do not have to diffuse from the bulk structure of the mixed oxide.

Processing a feedstock at the azeotropic composition of an ethanol/water mixture shows to increase the selectivity towards ethanol decomposition, i.e., 0.5 % to 15.3 %. Possible hypotheses for this increased formation could be assigned to an increased decomposition of ethanol combined with a water gas shift or due to removal of cokes deposited on the surface. Furthermore, it is observed that water will affect the regenerability of the catalyst. This is possibly assigned to an impeded formation of PdZn upon regeneration, though a more in-depth analysis would be appropriate.

2 FUTURE WORK

Previous conclusions point out the superiority of the incorporated catalyst with a complete reduction cycle. Further investigation on the catalyst's performance, though, is required by means of generation of a kinetic dataset. Evaluation of the results obtained at different temperatures, pressures and space times could subsequently be applied in the parameter estimation of a kinetic model as constructed in Chapter 8. Nonetheless, extensions of the model are required with regard to the formation of methane and carbon monoxide at the surface of the catalyst, owing to the presence of metallic Pd. This needs to be included under the pretext of a different active site, as here, Zn is not present to alter the selectivity.

This decomposition of ethanol becomes more pronounced during processing of ethanol/water feedstock as is shown in Chapter 6. Only limited testing is yet available and further investigation of the effects of higher amounts of water on the conversion and selectivity of the catalysts is therefore required. Additional improvement of the analysis method could hereby clarify the actual reactions occurring at the surface of the catalyst. Afterwards, a more detailed kinetic investigation in the presence of water will lie within the possibilities. At first, though, an in-depth analysis by means of characterization, such as TEM, TPO-XRD, etc., is appropriate to study the effect of water processing on the structure of the catalyst. Redox cycles after reaction seem to have only a limited effect on the full regeneration of the catalyst. This effect needs to be evaluated at different water contents as one would expect this to be more pronounced at higher percentages. As such, a clear understanding of the phenomena occurring at the surface and in the bulk of the catalyst could offer solutions to counter these constraints.

Appendix A: Calculation of Thermodynamic Equilibrium

1 THERMODYNAMIC DATA

For a complete method of calculation, the reader is referred to the course of Chemical Reactors: Fundamentals and Applications of Guy B. Marin at Ghent University [1]. The values for the corresponding enthalpies of formation, standard molar entropies and specific heat capacities to calculate the standard Gibbs energy of reaction, and hence the equilibrium coefficient, are provided in literature by Paraskevas et al. [2] for ethanol, acetaldehyde and ethyl acetate. These are listed in Table A-1.

Table A-1: Standard enthalpies of formation, standard molar entropies and specific heat capacities of reactants and products as according to Paraskevas et al. [2]

Component	$\Delta_f H°$	$S°$	c_p (J mol^{-1} K^{-1})			
	(kJ mol^{-1})	(J mol^{-1} K^{-1})	300 K	400 K	500 K	600 K
Ethanol	-236.2	289.6	66.4	81.1	95	107
Acetaldehyde	-164.9	271.5	53.9	64.5	74.9	84.2
Ethyl Acetate	-445.4	380.0	106.7	133.4	158.1	179.7

The corresponding values for hydrogen are determined via the NIST library [3], which states following correlations between temperature and the enthalpy of formation and the standard molar entropy of hydrogen:

$$\Delta_f H° = A\,t + B\frac{t^2}{2} + C\frac{t^3}{3} + D\frac{t^4}{4} - \frac{E}{t} + F \tag{A-1}$$

$$S° = A\ln(t) + Bt + C\frac{t^2}{2} + D\frac{t^3}{3} - \frac{E}{2\,t^2} + G \tag{A-2}$$

with

$$t = \frac{T}{1000} \tag{A-3}$$

The values corresponding with the constants shown in expressions (A-1) and (A-2) are listed in Table A-2.

Table A-2: Parameters for the calculation of the standard enthalpy of formation and standard molar entropy of hydrogen

Parameter	
A	33.066
B	-11.363
C	11.433
D	-2.7729
E	-0.15856
F	-9.9808
G	172.71

2 CONVERSION AT EQUILIBRIUM

In order to express the equilibrium coefficient as a function of conversion, the assumption of an ideal gas mixture is introduced. That way, the equilibrium coefficient could be written in terms of partial pressures of reactants and products:

$$K_r = \prod_i \left(\frac{p_i}{p_t}\right)^{v_i} = \frac{p_{AcH} p_{H_2}}{p_{EtOH} p_t} \tag{A-4}$$

The partial pressures are consequently defined as a function of the conversion of ethanol. Hereby, it is necessary to account for the dilution of nitrogen which comprises 95 % of the inlet flow of the reactor:

$$p_{EtOH} = \frac{1 - X_{EtOH}}{20 + X_{EtOH}}\, p_t \qquad p_{AcH} = p_{H_2} = \frac{X_{EtOH}}{20 + X_{EtOH}} p_t \tag{A-5}$$

As such, an expression for the equilibrium coefficient is obtained, solely depending on the conversion of ethanol:

$$K_r = \frac{X_{EtOH}^2}{(1 - X_{EtOH})(20 + X_{EtOH})} \tag{A-6}$$

Taking into account the values for the equilibrium coefficient that were determined in previous section, the corresponding equilibrium conversions are obtained. These are listed, along with the equilibrium coefficients, in Table A-3 for a considered temperature range of 533 to 573 K.

Table A-3: Equilibrium coefficients and conversions at equilibrium for different temperatures

Temperature (K)	K_{eq}	X_{eq}
533	0.460	0.913
553	0.905	0.952
573	1.700	0.973

3 TEMPERATURE DEPENDENCE OF THE EQUILIBRIUM COEFFICIENTS

Expression (A-2) already indicated that the equilibrium coefficient will depend on temperature, both due to the term in the exponent as due to the temperature dependence of the Gibbs free reaction energy. Since the coefficients of both dehydrogenation reactions are present in the kinetic model, introduced in Chapter 8, this temperature dependence must be included. For this reason the equilibrium coefficient was calculated at different temperatures and represented in Figure A-1.

If one assumes that the standard reaction enthalpy and entropy are approximately constant over a considered temperature interval of 533 to 573 K, a regression could be performed on the data points as according to the Van 't Hoff relation. The temperature variation of the equilibrium coefficient for the first and second dehydrogenation reaction, respectively, is than shown in expression (A-7) and (A-8).

$$\ln[K_{dhg,1}] = \frac{3758.4}{T} - 1.2986 \quad \text{(A-7)}$$

$$\ln[K_{dhg,2}] = \frac{-9981.6}{T} + 17.95 \quad \text{(A-8)}$$

These exponential dependencies on temperature are subsequently implemented in the kinetic model.

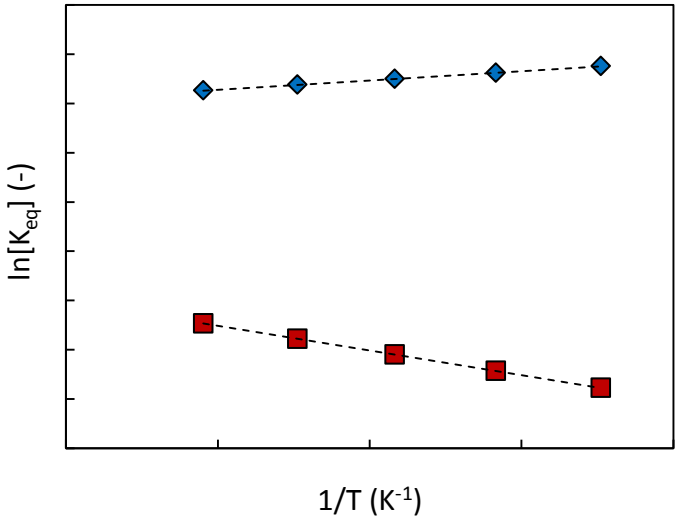

Figure A-1: Temperature dependence of Gibbs free reaction energy for both the first (diamonds, blue) and second (cubes, red) dehydrogenation reaction, the dotted lines represent the regression performed as according to the Van 't Hoff relation

4 REFERENCES

[1] G.B. Marin, Chemical Reactors: Fundamentals and Applications, Ghent University, 2015.
[2] P.D. Paraskevas, M.K. Sabbe, M.F. Reyniers, N. Papayannakos, G.B. Marin, Group Additive Values for the Gas-Phase Standard Enthalpy of Formation, Entropy and Heat Capacity of Oxygenates, Chem-Eur J, 19 (2013) 16431-16452.
[3] Chase, Hydrogen: Gas Phase Thermochemistry Data, NIST Webbook, 1998.

Appendix B: Lab Journal